Magnetic Ion Doping and Secondary Phase Assisted Enhancement in Thermoelectric Properties of Chalcopyrite Type Compounds for Energy Applications

Fahim Ahmed

February 2019

Magnetic Ion Doping and Secondary Phase Assisted Enhancement in Thermoelectric Properties of Chalcopyrite Type Compounds for Energy Applications

Fahim Ahmed

Doctoral Program in Materials Science and Engineering

Submitted to the Graduate School of

Pure and Applied Sciences

in Partial Fulfillment of the Requirements

for the Degree of Doctor of Philosophy in

Engineering

at the

University of Tsukuba

Dedicated to my beloved Parents.

Table of Contents

Outline of Thesis **13**
Chapter 1: **14**
Thermoelectric Phenomenon and Brief Background **14**
1.1 Thermoelectricity 14
1.2 Seebeck Effect 14
1.3 Efficiency and Figure of Merit (ZT) 15
1.4 Peltier Effect 16
1.5 Coefficient of performance (COP). 17
1.6 Thomson Effect 18
2. Challenges in Thermoelectricity / TE Paradoxes 18
2.1. Seebeck coefficient and Electrical conductivity. ($S \sim \sigma$) 18
2.2. Electronic thermal conductivity and electrical conductivity ($k_e \sim \sigma$) 19
3. Approaches to tackle challenges 20
3.1 Nano structuring 20
3.2 Phonon thermal Transport Engineering 21
3.3 Band Structure Engineering (BSE) 21
4. Promising thermoelectric materials. 22
4.1 Bismuth Telluride Bi_2Te_3 22
4.2 Lead Telluride PbTe 23
4.3 SiGe Alloys 24
4.4 SnSe 24
4.5 Other High Performance TE Materials 25
Chapter 2: **27**
Characterization Techniques and Synthesis Process **27**
1. Synthesis Process. 27
2. Laser Flash Analysis (LFA) 29
3. Seebeck Coefficient and Electrical resistivity Measurement 30
4. Electron Probe Micro Analyzer (EPMA) 31
5. Magnetic Property Measurement System (MPMS) 32
6. Physical Property Measurement System (PPMS) 33
Chapter 3: **34**
Mn Incorporated $CuGaTe_2$: Power Factor Enhancement **34**
1. Background 34

2. Literature Review 34
3. Abstract 35
4. Experiments 36
5. Structural Analysis 36
6. Thermoelectric Properties 39
6.1 Electrical conductivity, Seebeck and Power factor. 39
6.2 Seebeck vs ln σ Plot 42
7. Magnetic Properties 44
7.1 Magnetic Susceptibility 44
7.2 Magneto-transport properties 46
8. Thermal Conductivity and Figure of merit. 49
9. Summary 51
Chapter 4: 52
Thermoelectric and Magnetic Properties of Mn Doped $CuInTe_2$ 52
1. Introduction 52
2. Experimental Section 53
3. Results 53
3.1 Structural Analysis 53
4. Magnetic Properties 54
5. Thermoelectric properties 56
6. Summary 62
Chapter 5: Secondary Phase Assisted Enhancement in TE Properties of Fe doped $CuGaTe_2$ 63
1. Introduction 63
2. Method and Materials 64
3. Structural Analysis 64
4. Microstructure and compositional analysis 65
5. Thermoelectric Properties 71
6. Thermal Transport Properties 72
7. Summary points 74
Conclusions and Outlook 75
Appendix A 76
References 77
Achievements 90
***Acknowledgements* 91**

List of Figures

Figure 1.1 Illustration of Seebeck effect for power generation for two dissimilar materials (b) shows schematic moving of charge carriers when subjected to temperature gradient for p-type material 14

Figure 1.2 (a) Schematic working of thermoelectric couple producing electric power. (b) Plot showing relationship between Power generating efficiency and average *ZT* for specific temperature difference. 15

Figure 1.3 Schematic working of Peltier Effect for two dissimilar materials 17

Figure 1.4 (a) Schematic working of thermoelectric couple as refrigerator. (b) Shows typical values of cooling efficiency with respect to average *ZT* value 17

Figure 1.5 Graph of Seebeck coefficient and Electrical conductivity dependence on carrier concentration. Green region shows best spot for power factor and usually for degenerate semiconductors 19

Figure 1.6 Density of states (DOS) dependence of energy for (a) 3D Bulk Semiconductor (b) 2D quantum Well (c) 1D Quantum Wire (d) Quantum Dot 20

Figure 1.7 Figure of merit values for state of art thermoelectric materials as a function of temperature [Reprinted with permission Copyright Elsevier Ref 87] 25

Figure 2.1 (a) Heat treatment scheme (b) SPS heat treatment scheme, RT represents room temperature 27

Figure 2.2 Schematic working of Spark Plasma Sintering 28

Figure 2.3 Shows various steps and process involved in solid state reaction synthesis of a material 28

Figure 2.4 Schematic illustration of working principle in laser flash analysis (LFA) 29

Figure 2.5 Typical output signal also called thermogram obtained in LFA 29

Figure 2.6 Schematic working of Seebeck and resistivity measurement apparatus ZEM-2 30

Figure 2.7 A schematic of Electron micro probe analysis (EPMA). A fine polished sample used for analysis is shown in left bottom Ref [135] 31

Figure 2.8 Magnetic property measurement system (MPMS) and superconducting pick up coil on (left) Ref [136] 32

Figure 2.9 shows physical property measurement system (PPMS) and AC Transport Puck used as sample holder on the right side Ref [137] 33

Figure 3.1 (a) Powder XRD patterns of polycrystalline samples of $CuGa_{1-x}MnxTe2$ (x = 0-0.03). At the bottom of the XRD patterns we showed standard reference card data. (b)

Lattice constant dependence on Mn doping concentration (c) Schematic crystal structure of chalcopyrite $CuGaTe_2$ shown along c-axis. 37

Figure 3.2 The results of Rietveld refinement for the $CuGa_{1-x}Mn_xTe_2$, x = 0.0, 0.01, 0.02, 0.03 including the observed and calculated diffraction data along with their difference 38

Figure 3.3 Transport properties for the $CuGa_{1-x}Mn_xTe_2$, x = 0.0, 0.01, 0.02, 0.03. Temperature dependent plots of (a) electrical conductivity, σ (b) Seebeck coefficient, S (c) Power factor, σS^2 40

Figure 3.4 (a) Hall coefficient R_H of $CuGa_{1-x}Mn_xTe_2$ as functions of temperature. (b) Hole concentration as a function of temperature for $CuGa_{1-x}Mn_xTe_2$ (c) Carrier mobility and effective mass in $CuGa_{1-x}Mn_xTe_2$ at 325 K as functions of composition x. Lines in (c) serve as guides for the eye. 41

Figure 3.5 Seebeck coefficient graph with respect to lnσ for $CuGa_{1-x}Mn_xTe_2$ at various temperatures. Slope of broken and dotted lines is -86.14 µV/K, as proposed by the model. 42

Figure 3.6 Plot of Seebeck coefficients and lnσ for $CuGa_{1-x}Mn_xTe_2$. Slope of broken lines is -86.14 µV/K, as proposed by the model. [Rowe1995] 43

Figure 3.7 shows plots of power factor dependence on electrical conductivity for the $CuGa_{1-x}Mn_xTe_2$. Purple (solid) lines indicates the calculation on the basis of theoretical model. Red circles indicates observed values of power factor. 44

Figure 3.8 shows temperature dependence of inverse of magnetic susceptibility as a result of Mn ions. $CuGaTe_2$ contribution in measured susceptibility has been subtracted..... 45

Figure 3.9 (a) Magnetization as a function of magnetic field H (b) Hall resistivity as a function of magnetic Field (H) for the composition $CuGa_{0.97}Mn_{0.03}Te_2$. Dashed lines indicates Landaus expansion fitting. 47

Figure 3.10 Hall resistivity as a function of H for the composition $CuGa_{0.97}Mn_{0.03}Te_2$. Open and filled circles indicates AHE contribution and measured values of Hall resistivity respectively. Whereas, NHE contribution is represented by crosses in the figure... 48

Figure 3.11 Seebeck coefficient values for $CuGa_{0.97}Mn_{0.03}Te_2$ at low temperature..... 48

Figure 3.12 (a) Total thermal conductivity as a function of temperature for the $CuGa_{1-x}Mn_xTe_2$, x = 0.0, 0.01, 0.02, 0.03. (b). Plots of Lattice thermal conductivity (c) Plots of electronic contribution towards total thermal conductivity. 49

Figure 3.13 Thermoelectric Figure of merit (ZT) as a function of temperature for the $CuGa_{1-x}Mn_xTe_2$, x = 0.0, 0.01, 0.02, 0.03. 50

Figure 4.1 XRD patterns of $CuIn_{1-x}Mn_xTe_2$ with x = 0.0, 0.01, 0.02. All peaks observed in X-ray patterns were matched with those of the chalcopyrite structure. ICSD Reference card (PDF # 01-081-1937) 2θ positions are shown in the bottom of the graph with bar symbol 53

Figure 4.2 Rietveld refinement result for the powder X-ray diffraction pattern of $CuInTe_2$. Inset shows dependence of lattice constants (a on left axis, c on right axis) with respect to Mn composition 54

Figure 4.3 Temperature dependence of magnetic properties for $CuIn_{1-x}Mn_xTe_2$ with $x = 0.0$-0.02. (a) Magnetic field dependence of magnetization M measured at 5 K (b) Magnetic field dependence of magnetization M measured at 300 K 55

Figure 4.4 Inverse of magnetic susceptibility verses temperature. Contribution from pristine $CuInTe_2$ has been subtracted from measured susceptibility. Black solid lines shows fit with linear function 56

Figure 4.5 Temperature dependence of electrical properties. (a) Electrical resistivity, (b) Seebeck coefficient, for $CuIn_{1-x}Mn_xTe_2$ 57

Figure 4.6 Power factor as a function of temperature for $CuIn_{1-x}Mn_xTe_2$ where $x = 0.0$, 0.01, 0.02 58

Figure 4.7 Plots of Seebeck coefficient at temperature 324, 370, 420, and 463 K as a function of $\ln\sigma$. Black dotted lines have the slope of -86.14 μV/K. For $x = 0.02$ sample, data (shown with triangles) lie above the slope line of non-doped sample (shown with squares), indicating improvement in the effective mass term with Mn doping. 59

Figure 4.8 Relative power factors of $CuIn_{1-x}Mn_xTe_2$ with respect to that of $x = 0$ as functions of temperature. Yellow regions (T < 450K) corresponds to the degenerate semiconductor region, and white (> 450K) indicates the intrinsic semiconductor region. In degenerate semiconductor region below 450 K relative power factor values increases and then started decreasing in intrinsic region. 60

Figure 4.9 Temperature dependence of thermal transport properties. (a) Total thermal conductivity, (b) electronic thermal conductivity, (c) Figure of merit (ZT) for $CuIn_{1-x}Mn_xTe_2$ 61

Figure 5.1 Powder XRD patterns of polycrystalline samples of $CuGa_{1-x}Fe_xTe_2$ ($x = 0$, 0.01, 0.02, 0.03). At the bottom of the XRD patterns standard reference card data is shown. 64

Figure 5.2 (a) Powder XRD patterns of polycrystalline samples of $CuGa_{1-x}Fe_xTe_2$ ($x = 0.04$, 0.05). Clearly showing secondary phase peaks in the inset. (b) Plot of Lattice constants with respect to Fe composition 65

Figure 5.3 BSE images captured in EPMA for (a) $CuGaTe_2$ (b) $CuGa_{0.99}Fe_{0.01}Te_2$ (c) $CuGa_{0.98}Fe_{0.02}Te_2$, (d) $CuGa_{0.97}Fe_{0.03}Te_2$, (e) $CuGa_{0.96}Fe_{0.04}Te_2$, (f) $CuGa_{0.95}Fe_{0.05}Te_2$. M[1,2,3,4,5,] are the points mentioning the main phase and S[1,2,3] are the points referring to secondary phases. 67

Figure 5.4 displays mapping of the elements (Cu), (Ga) (Fe) (Te) and (O) for the sample (a) $CuGaTe_2$ and (b) $CuGa_{0.99}Fe_{0.01}Te_2$. 68

Figure 5.5 displays mapping of the elements (Cu), (Ga) (Fe) (Te) and (O) for the sample (a)

$CuGa_{0.98}Fe_{0.02}Te_2$.and (b) $CuGa_{0.97}Fe_{0.03}Te_2$ 69
Figure 5.6 displays mapping of the elements (Cu), (Ga) (Fe) (Te) and (O) for the sample (a) $CuGa_{0.96}Fe_{0.04}Te_2$. (b) $CuGa_{0.95}Fe_{0.05}Te_2$. 70
Figure 5.7 (a) Plots of electrical resistivity (b) Seebeck Coefficient as a function of temperature for $CuGa_{1-x}Fe_xTe_2$ where x = 0.0-0.05..... 71
Figure 5.8 Plots of Power factor as a function of temperature for $CuGa_{1-x}Fe_xTe_2$ where x = 0.0-0.05. 72
Figure 5.9 Plots of (a) total thermal conductivity (b) lattice thermal conductivity as a function of temperature for $CuGa_{1-x}Fe_xTe_2$ where x = 0.0-0.05. (c) Lattice thermal conductivity plot with inverse of temperature. Black dotted lines shows linear fitting. (d) Lattice thermal conductivity values at different temperature as a function of Fe doping concentration 73
Figure 5.10 Figure of merit (ZT) values as a function of temperature for $CuGa_{1-x}Fe_xTe_2$ where x = 0.0-0.05..... 74

List of Tables

Table 1: shows values of lattice constants, and relative densities for all the nominal compositions..... 39

Table 2: Values of effective magnetic moment, Curie constant and Weiss temperature for $CuGa_{1-x}Mn_xTe_2$ obtained by data fitting. 45

Table 3: Values of Curie constant, Weiss temperature and Effective magnetic moment (μ_{eff}). 56

Table 4: shows nominal and analyzed composition along with lattice parameters and relative density..... 66

Introduction

Energy harvesting has become the most important research topic in the modern world. There is swelling demand for electricity. Most of energy is extracted using natural energy resources. This led to depletion of fossil fuel [1], [2]. Besides this, abundant use of fossil fuel have increased environmental pollution. Hence, alternate energy sources should be in high priority to tackle energy related issues. Renewable energy sources like solar cell, Fuel cell, Wind power are already being used as a substitute. Most of the energy generated form fossil fuel is being wasted in the form of heat. For example, in vehicles (> 60 %) of energy produced from gas is wasted and only 40 % is used [2]. Similarly in homes major part of electricity is wasted in the form of heat. Thermoelectric (TE) energy conversion can help in recovering this waste energy. TE devices are capable to convert waste heat directly into useful electricity. Generally, dimensionless Figure of merit, $ZT = S^2\sigma T/\kappa$ is used to evaluate TE material. Where S is Seebeck coefficient, σ is electrical conductivity, κ represents thermal conductivity and T is symbol for absolute temperature [3]. Short detail of mechanism and other important equations to understand working of thermoelectric generator (TEG) are presented in chapter 1. Good thermoelectric materials have high Seebeck coefficient and electrical conductivity, whereas thermal conductivity should be low to maintain temperature gradient inside the material. This is very difficult for a material to have these qualities simultaneously [4]. Various approaches and techniques are used to de-link these parameters in order to enhance overall ZT value. i.e. Nano structuring, Band gap engineering, charge carriers optimization, Nano inclusions etc [1], [4]–[7]. High ZT is mandatory to make TE devices more common. In comparison with other renewable techniques, thermoelectric energy conversion offers multiple advantages [8], [9]. First of all, there are no moving parts in a thermoelectric device thereby TE device need no maintenance and work for longer period of time. TE devices are compact in size which enables them to extract waste heat from most of working places. TE devices can be designed to withstand harsh environment conditions as well. Hence, quest for new and efficient thermoelectric materials is in high demand. In this thesis we discussed an alternate method to improve the ZT value. In this context we studied chalcopyrite type materials and carried out their TE properties. $CuGaTe_2$ based materials are being studied extensively for TE applications [10]–[19]. Because of their Diamond and zinc blende type structure their properties are most favorable for an ideal TE material. Moreover their ZT value is higher than most TE materials being under research making them very close to be used in TE devices. The aim of this research is to improve TE properties by new and previously developed methods. We proposed that by substituting a magnetic ion into a dilute magnetic semiconductor we can enhance power factor value, thereby overall ZT of TE material. The interactions between charge carriers and magnetic moments of magnetic element contribute towards enhancement of power factor by increasing effective mass. (Magnetic

enhancement). The other part of the thesis discuss about secondary phase assisted thermoelectric properties enhancement. In this part we discussed importance of microstructure analysis. By controlling microstructure we can reduce lattice thermal conductivity more effectively. Highest ZT value of 0.83 was achieved by implying Mn ions in $CuGaTe_2$ [20]. Which is 40% enhancement of ZT value. In the other case we measured ZT value of 0.92 by controlling microstructure and reducing thermal conductivity. Which is around 60% of ZT enhancement [21]. We expect to apply these mechanisms in order to enhance thermoelectric properties of various other TE families and materials.

Outline of Thesis

In the first chapter of this thesis we present a brief introduction to thermoelectricity. We discussed the thermoelectric effects which are Seebeck effect, Thomson Effect and Peltier effect. Moreover we discussed equations governing Figure of merit (*ZT*) and efficiency. Also commonly used thermoelectric materials and approaches to enhance TE properties are briefly discussed. Lastly this chapter pictures the current state of thermoelectric materials for energy conversion applications.

In the second chapter we discussed the synthesis method used in fabrication of materials. This chapter presents various stages of synthesis as well. Also we present mechanism and working of essential experimental techniques used to characterize materials.

In the third chapter we showed results of thermoelectric properties of $CuGa_{1-x}Mn_xTe_2$. A new idea of magnetic enhancement in power factor is presented. It has been demonstrated that by substituting a magnetic ion in $CuGaTe_2$, a significant enhancement in the power factor is observed. Using theoretical model interpretations and evaluating magnetic properties we showed power factor surpass normal carrier tuning effect. Owing to reduced thermal conductivity and carrier magnetic moments correlations we observed around 40 % enhancement in the power factor. Results demonstrate that magnetic ion doping is an effective technique to enhance thermoelectric properties. In addition, open an opportunity for research on other thermoelectric families.

In Fourth chapter we presented thermoelectric and magnetic properties of $CuIn_{1-x}Mn_xTe_2$. Results showed that the Mn ions doped in $CuInTe_2$ are in the Mn^{3+} state. From the Curie-Weiss fitting, a strong antiferromagnetic interaction between Mn and carriers was inferred, which suggests the magnetic interaction is a probable origin for the enhanced power factor. Thermoelectric and magnetic properties of $CuIn_{1-x}Mn_xTe_2$ provides further evidence of carrier magnetic moments correlations presented in Chapter 3. Results reinforced the idea of magnetic enhancement in chalcopyrite type compounds.

In the fifth Chapter we report results of Fe substitution and its effects on thermal transport and structural properties in chalcopyrite-type $CuGaTe_2$. In this work role of secondary phases and microstructural analysis towards improvement in thermoelectric properties of chalcopyrite $CuGaTe_2$ is demonstrated. Power factor has been improved with Fe addition. Thereby, Figure of merit (*ZT*) was enhanced and maximum value of 0.92 is obtained at 770 K for composition $CuGa_{0.98}Fe_{0.02}Te_2$. This is around 60 % improvement as compared to pristine $CuGaTe_2$.

Chapter 1: Thermoelectric Phenomenon and Brief Background

1.1 Thermoelectricity

Thermoelectricity is the phenomenon which enables waste heat conversion into useful electricity. This conversion of heat into electricity is based on Seebeck effect [3]. In thermoelectricity there are three main effects discussed as follows.

1.2 Seebeck Effect

The process in which voltage differential is developed across the junctions of two dissimilar materials when subjected to temperature gradient is known as Seebeck effect [22]. (See Figure 1.1). When a TE material subjected to a temperature gradient, the charge carriers inside the material tend to move from hot side to cold side producing an electric current. The Seebeck effect was first discovered in 1821 by Thomas Johann Seebeck. A schematic illustration of Seebeck effect for power generation in a p-type material is shown in Figure 1.1 Voltage difference (ΔV) is developed across the material. This change in voltage is directly proportional to the temperature gradient (ΔT). Eq. 1 relates Seebeck coefficient with temperature gradient.

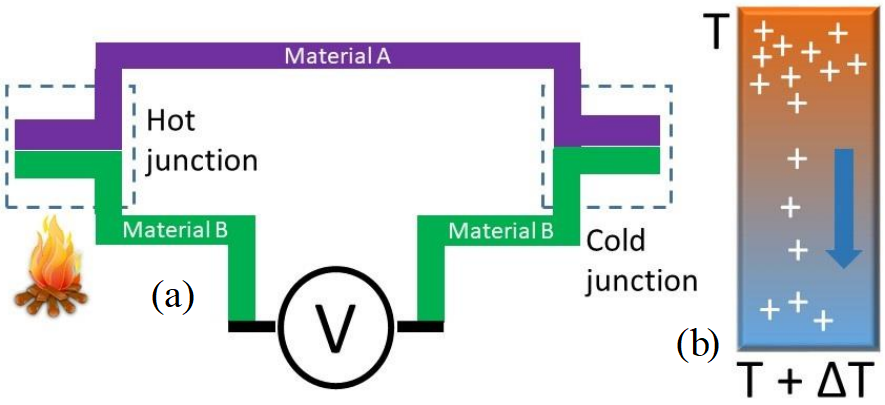

Figure 1. 1 Illustration of Seebeck effect for power generation for two dissimilar materials (b) shows schematic moving of charge carriers when subjected to temperature gradient for p-type material

$$S = \frac{\Delta V}{\Delta T} \qquad (1)$$

$$S = \frac{8\pi^2 k_B^2}{3eh^2}\left(\frac{\pi}{3n}\right)^{2/3} m^* T \qquad (2)$$

Where

- ✧ k_B Boltzmann and Planck's constant
- ✧ h Planck's constant
- ✧ m^* Effective mass
- ✧ n Carrier concentration

Eq. 2 is another way of expressing Seebeck coefficient for a degenerate semiconductor [23]. Seebeck coefficient depends on no of parameters as described in the Eq. 2. From equation 2 Seebeck is inversely proportional to amount of carriers *n*. Thereby, Large carrier concentration leads to lower Seebeck coefficient. It has been recommended for a material to have only one type of charge carriers to produce maximum value of Seebeck coefficient [24]. In opposite case, mixed charge carriers will cancel out the effect. Large effective mass also contribute to high Seebeck coefficient value. Effective mass is related to band structure. High density of states at fermi surface results in high effective mass [25].

1.3 Efficiency and Figure of Merit (*ZT*)

Performance of thermoelectric materials is evaluated by Figure of merit (*ZT*) [3]. According to the equation

$$ZT = \frac{S^2\sigma T}{\kappa_{tot}} = \frac{S^2\sigma T}{\kappa_{latt} + \kappa_e} \qquad (3)$$

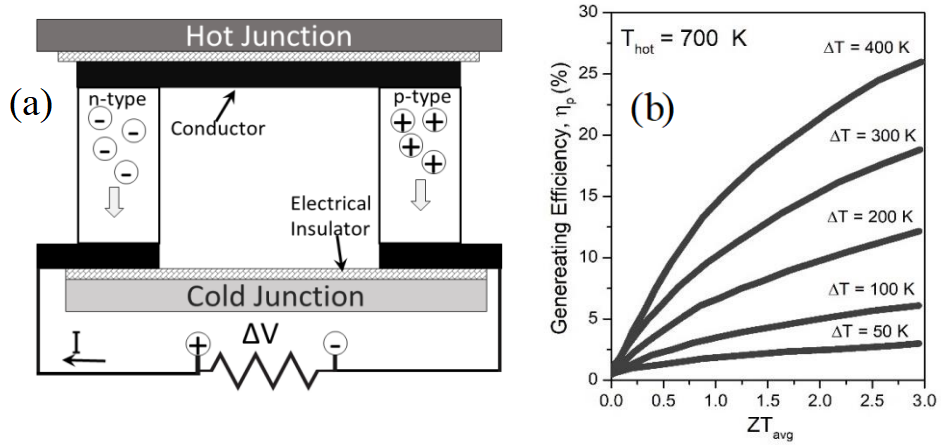

Figure 1. 2 (a) Schematic working of thermoelectric couple producing electric power. (b) Plot showing relationship between Power generating efficiency and average *ZT* for specific temperature difference.

Where S is Seebeck coefficient, σ is electrical conductivity and $\kappa_{tot}, \kappa_{latt}, \kappa_e$ are total thermal conductivity, Lattice thermal conductivity and electronic thermal conductivity. Total thermal conductivity is sum of electronic and lattice thermal conductivity $\kappa_{tot} = \kappa_{latt} + \kappa_e$. Efficiency of thermoelectric material for power generation is defined as [26]

$$\eta_p = \frac{\Delta T}{T_{hot}} \frac{\sqrt{1 + ZT_{avg}} - 1}{\sqrt{1 + ZT_{avg}} + \frac{T_{cold}}{T_{hot}}} \qquad (4)$$

Here, ΔT is difference in temperature, T_{hot}, T_{cold} are the temperature of hot side and cold side. Figure 1.2 (a) shows schematic working of single TE module. It contains both *n*-type and *p*-type leg with heat source and heat sink. Difference in energy drives the charge carriers from hot to cold side generating potential difference (ΔV). As described in Eq. 4 efficiency of TE device depend on ZT value of a material and temperature gradient ΔT. Figure 1.2 (b) shows relationship between percentage efficiency and ZT value of a material at specific ΔT. For instance, efficiency of around 20 % can be achieved with a material having $ZT = 2$ with ΔT of 400 K [27]. Hence, materials with high ZT value is first priority for efficient TE devices. For a long time ZT~1 remained highest value [24], [28]. Thereby, applications of TE materials were restricted to government sector i.e. deep space missions. Now with advanced research and technology materials with ZT >1 are also available in the market. Thus, TE materials are gaining importance in niche applications as well. E.g. Watches, cell phone charging, fans etc.

1.4 Peltier Effect

Peltier effect is reverse of Seebeck effect. The process in which temperature differential is developed across the junctions of two dissimilar materials when an electric current pass through it is known as Peltier effect [29]. Peltier effect was discovered after Seebeck effect discovery in 1834 by Jean Charles Athanase Peltier. Peltier Coefficient π_{ab} (T) is defined as follows [29]

$$\pi_{ab}(T) = \frac{\Delta Q}{I} \qquad (5)$$

- ΔQ= fraction of heat absorbed or liberated at the junctions
- I= Current

Peltier effect provides an alternate method of refrigeration [30]–[33]. Peltier cooling have multiple advantages over normal refrigeration. Such as no harmful gasses are used in the process, light weight, noiseless and enhanced reliability due to solid state devices [30]–[32]. A schematic illustration of Peltier effect is shown in Figure. 1.3.

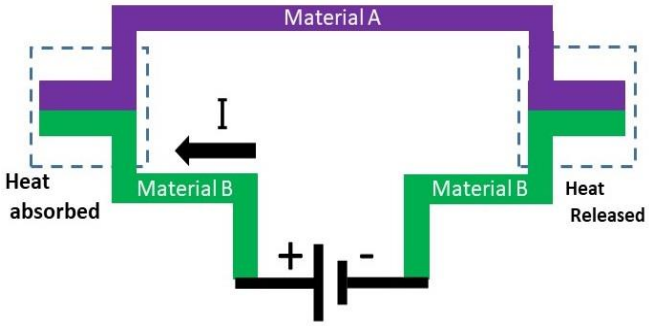

Figure 1. 3 Schematic working of Peltier Effect for two dissimilar materials

1.5 Coefficient of performance (COP).

Figure. 1.4 (a) illustrate schematic working of thermoelectric refrigerator (TER). Cooling efficiency in terms of ZT can be written by equation 6 [29], [31], [32]. Similar to power generation performance of thermoelectric refrigerator will be higher for materials with high ZT values. Figure. 1.4 (b) shows typical values of cooling efficiency with respect to average ZT value [34], [35] .

$$\eta_c = \frac{T_{cold}}{\Delta T}\frac{\sqrt{1+ZT_{avg}} - \frac{T_{hot}}{T_{cold}}}{\sqrt{1+ZT_{avg}}+1} \qquad (6)$$

Thermoelectric cooling efficiency is also referred to as coefficient of performance (COP). COP is defined as the ratio of cooling capacity (Q_c) and energy supplied. Despite of their advantages over traditional cooling techniques, TER are not commonly available yet due to low COP. New techniques and methods were suggested recently to enhance COP [30], [32], [33], [36]–[38]. Based on these advancements it is expected that TER will play a crucial role for alternate cooling applications in future.

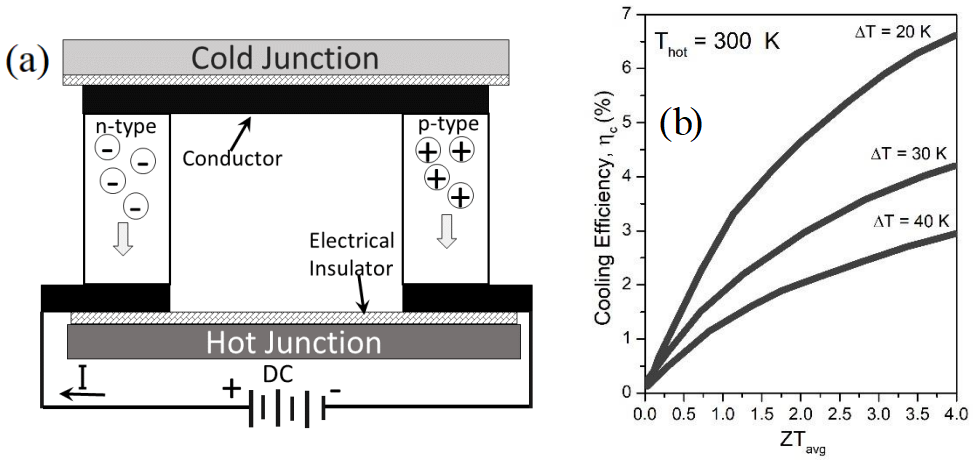

Figure 1. 4 (a) Schematic working of thermoelectric couple as refrigerator. (b) Shows typical values of cooling efficiency with respect to average ZT value

1.6 Thomson Effect

After the discovery of Seebeck and Peltier effect William Thomson discovered the third thermoelectric effect in 1851 known as Thomson effect. According to Thomson effect, if current is passed through a homogeneous conductor having temperature differential. It will absorb or release heat energy [3], [4]. The amount of heat absorbed/released depend on amount and direction of current *I*. Thomson coefficient (β) relation with heat (q) can be written as follows

$$q = \beta I \Delta T \text{ ---------- (7)}$$

2. Challenges in Thermoelectricity / TE Paradoxes

It is evident from preliminary introduction that high ZT is utmost requirement for efficient thermoelectric devices. In this discussion we highlighted some obstacles which come across in enhancing efficiency of thermoelectric devices.

2.1. Seebeck coefficient and Electrical conductivity. ($S \sim \sigma$)

Seebeck Coefficient can be defined as the amount of induced voltage established in a material as a result of temperature gradient. ZT value get most effected by value of Seebeck coefficient because it is directly proportional to the square of Seebeck coefficient as described in equation 6. Seebeck coefficient value varies with types of materials. Metals have the lowest Seebeck coefficient values than semiconductors and insulators. As expressed in Eq. 2 Seebeck coefficient is inversely proportional to charge carriers concentration n, thereby in order to increase Seebeck coefficient value it comes with expense of reduction in electrical conductivity σ. For semiconductor with single type of charge carriers electrical conductivity is related to carrier concentration n as,

$$\sigma = en\mu_e \qquad (8)$$

So the first solution to this contradiction is optimizing carrier concentration to find optimum power factor (σS^2). This can be best visualize by the graph of Seebeck coefficient and electrical conductivity dependence of carrier concentration as seen in Figure 1.5. Generally semimetals and degenerate semiconductors have favorable carrier concentration for high power factor. Band structure engineering (BSE) is one of the commonly used technique to enhance power factor [17], [39], [40]. Seebeck coefficient in terms of band structure parameters for a degenerate semiconductor is given by Mott relation[41].

$$S = \frac{\pi^2}{3}\frac{k_B^2 T}{e}\left\{\frac{d\left[\ln\left(\sigma(E)\right)\right]}{dE}\right\}_{E=E_F} \qquad (9)$$

$$= \frac{\pi^2}{3}\frac{k_B^2 T}{e}\left\{\frac{1}{n}\frac{dn(E)}{dE} + \frac{1}{\mu}\frac{d\mu(E)}{dE}\right\}_{E=E_F}$$

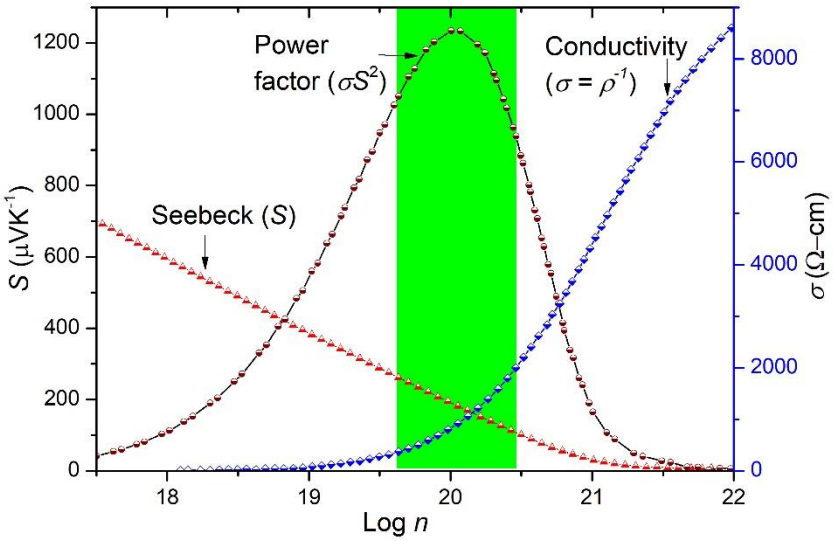

Figure 1. 5 Graph of Seebeck coefficient and Electrical conductivity dependence on carrier concentration. Green region shows best spot for power factor and usually for degenerate semiconductors

Where k_B is the Boltzmann constant, e is the carrier charge, and μ is the energy-dependent carrier mobility. Eq. 9 explains increase in Seebeck coefficient by increasing local density of states (DOS). However this optimization by BSE is quite challenging due to very weak control over it [24], [25], [42], [43]. Another conflict exist between density of state effective mass (m^*) and mobility of charge carriers μ. High effective mass m^* which is related to flat band contributes towards high Seebeck coefficient values (see Eq. 2) while large effective mass of charge carriers will clearly have low motilities. Which again reduces electrical conductivity as shown in Eq. 8. In the next section we will go through some advanced techniques reported to overcome this tradeoff between ($S \sim \sigma$) to achieve high power factor.

2.2. Electronic thermal conductivity and electrical conductivity ($k_e \sim \sigma$)

To hold the temperature gradient inside TE material thermal conductivity is required to be low as much as possible. Mainly there are two main contributions towards total thermal conductivity. Electronic thermal conductivity k_e (heat transported through charge carriers) and k_{latt} (heat transported by phonons).

$$k_{tot} = k_e + k_{latt} \qquad (10)$$

For metals and degenerate semiconductors Wiedemann Franz Law is written as [44], [45]

$$k_e = LT\sigma \qquad (11)$$

Where L is the Lorenz number, for degenerate limit its value is estimated as ($2.4x10^{-8}$ $W\Omega K^{-2}$). Lorenz number value varies with carrier concentration n. From Eq.11 it is clear that electrical conductivity will get affected in order to get low thermal conductivity. This is also a major conflict we have to deal within thermoelectricity.

3. Approaches to tackle challenges

In context of the contradictions described above many techniques has been studied and applied to TE materials. These techniques and methods helped in overcoming the challenges thereby showed better properties. Here we discuss some of the commonly used methods to improve TE properties.

3.1 Nano structuring

Nano structuring proved to be very useful in enhancing thermoelectric properties. For many years highest ZT value was confined to the range of 0.8-1.0 for bulk bismuth antimony telluride (BiSbTe). B. Poudel et.al showed monocrystalline BiSbTe reached value of 1.4 [46]. There are several other examples in which enhancement of thermoelectric properties via Nano structuring were implied[47]–[56]. Nano structuring assists in improving thermoelectric properties in two ways. Firstly thermopower ($S^2\sigma$) can be enhanced with the help of increasing DOS near Fermi level by quantum confinement[51], [57], [58]. Decrease in dimensionality can cause change in DOS (see Figure 1.6) which allow to control S and σ independently to some extent. Hicks and Dresselhaus were first to exploit the effects of quantum confinement and enhanced thermopower ($S^2\sigma$) in Bi_2Te_3.[59]–[61] Secondly with the help of Nano-structuring thermal conductivity can be reduced greatly. The mechanism behind reducing thermal conductivity is increase of interfaces and grain boundaries. These interfaces can scatter phonons more effectively thereby decreasing thermal conductivity[47], [62]. Hence, Nano structuring is a powerful technique to gain control over TE parameters and delink S and σ.

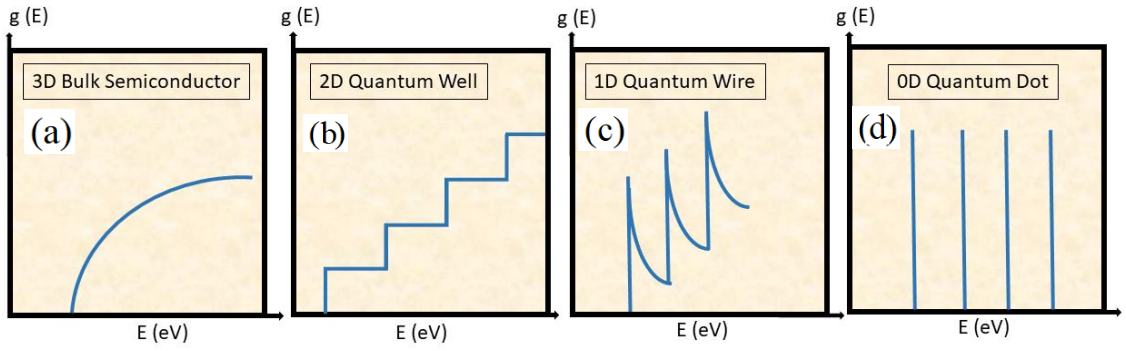

Figure 1. 6 Density of states (DOS) dependence of energy for (a) 3D Bulk Semiconductor (b) 2D quantum Well (c) 1D Quantum Wire (d) Quantum Dot

3.2 Phonon thermal Transport Engineering

It is seen in Eq. 10 Thermal conductivity consists of two major terms. Heat transported by lattice vibrations (Phonons) k_{latt} and charge carriers k_e. In metals and degenerate semiconductors heat transported through carriers is dominant, whereas in semiconductors and non-metals heat is mainly transported via lattice vibrations. Thermoelectric materials are mostly semiconductors so phonon thermal transport engineering plays an important role in enhancing Figure of merit *ZT*. According to Kinetic theory lattice thermal conductivity can be expressed by following equation[63], [64].

$$k_{Latt} = \frac{1}{3} C v l \qquad (12)$$

Where *C, v, l* represents specific heat, phonon velocity and phonon mean free path respectively. Eq. 12 can be modified using $l = v\tau$, where τ is phonon relaxation time.

$$k_{Latt} = \frac{1}{3} C v^2 \tau \qquad (13)$$

Generally, thermal conductivity can be decreased by decreasing phonon mean free path (decreasing phonon relation time) via enhanced phonon scattering[5], [24], [29]. There are three types of scattering. 1) Impurity scattering, it is the scattering of phonons due to dislocations, defects and alloying process. Impurity scattering is elastic scattering. Impurity elements usually have different mass and atomic radii as compared to the host crystal atoms. Thereby act as scattering center for phonons. 2) Boundary scattering, it is the scattering of phonons due to grain boundaries. This type of scattering helps in scattering low frequency phonons. 3) phonon-phonon scattering, It is inelastic scattering explained by Umklapp process [65] and this type of scattering occurs due to lattice anharmonicity. Other methods to reduce thermal conductivity includes decreasing of propagation velocity of phonons. Proven techniques to reduce velocity of phonon is by bond softening[64], [66]. If the restoring force is weak it leads to low phonon prorogation velocity. Secondly it was observed that heavy atoms inside the crystals also assist in decreasing phonon velocity thereby reduced thermal conductivity. Third parameter in Eq. 13 is Specific heat. Decreasing specific heat can help in decreasing thermal conductivity, however this is considered as a difficult task. W. Kim[64] discuss large unit cell approach to tackle specific heat.

3.3 Band Structure Engineering (BSE)

To improve thermoelectric Figure of merit (*ZT),* mostly research is based on reducing thermal conductivity. However, phonon thermal conductivity cannot be decreased after amorphous limit [8]. Hence other principles and techniques must be explored in order to further improve *ZT* value. Although other techniques involving band structure engineering are seldom used. The

reason is very weak control over the parameters and strong interdependence [31]. These reasons make it very challenging task. It is proved that taking control of electronic properties will give boost to thermoelectric performance. In 1959, Chasmar and Stratton introduced another performance indicator parameter for electronic properties also known as quality factor and B factor(β), which is proportional to mobility and effective mass as[9], [67], [68]

$$\beta \propto \frac{\mu N_V m^{*3/2}}{k_{latt}} \qquad (14)$$

Here m^* is the density of state effective mass and N_V is valley degeneracy. It was experimentally proved that large valley degeneracy will enhance Quality factor without any detrimental effect on other parameters [39]. N_V can be related to the effective mass as $m^* = N_V^{2/3} m_b^*$ (m_b^* is the mass of single valley) [31]. Hence if N_V is increased there will not be any negative effect on mobility. Other techniques to enhance power factor which involves Band structure engineering are Band convergence, Energy filtering, Carrier Pocket engineering etc. [39], [40], [43], [69]–[72]. There are several other examples of enhanced thermoelectric performance through BSE. Liu et al [42] showed increased values of Seebeck coefficient in $Mg_2Si_{1-x}Sn_x$ by enhancing density of state effective mass through band convergence without affecting mobility values.

4. Promising thermoelectric materials.

Since the discovery of Seebeck effect many materials were discovered having excellent thermoelectric properties. State of art thermoelectric materials includes Bi_2Te_3, PbTe, SiGe, SnSe. As performance of thermoelectric materials are temperature dependent. Bi_2Te_3 is the well-known champion material around room temperature. PbTe show good performance in mid temperature range. SiGe and SnSe exhibit good thermoelectric properties at higher temperatures. In this section we will look briefly into the properties of these well-known thermoelectric materials.

4.1 Bismuth Telluride Bi_2Te_3

In 1954 Goldsmith and Douglas reported Bi_2Te_3 having promising TE properties for refrigeration applications [73]. Bi_2Te_3 exhibit hexahedral-layered structure which consists of five atomic layers (Te1–Bi–Te2–Bi–Te1) with the band gap of 1.3 eV [1]. Pure Bi_2Te_3 have Seebeck coefficient of 220 μVK^{-1}, Electrical conductivity value of 400 $(\Omega.cm)^{-1}$ and thermal conductivity value of 2.1 W/m K [73]. Since then Bi_2Te_3 based alloys captured much attention for power generation applications around room temperature. Both *n*-type and p-type Bi_2Te_3 display favorable thermoelectric properties [26]. One of the reason behind excellent thermoelectric properties is multi-valley character of

Bi_2Te_3 [1], [4]. For many years Figure of merit for Bi_2Te_3 remained around unity [24]. To further improve thermoelectric properties many techniques were applied to optimize carrier concentration and for reduction of thermal conductivity [26]. *ZT* value of 1.33 at 398 K was reported by alloying 20% Bi_2Te_3 with 80% Sb_2Te_3 [74]. Poudel et al. Utilizing Nano structuring technique helped in enhancing *ZT* value of BiSbTe up to 1.4 at 373 K [46]. Major contribution in this enhancement was attributed to reduction in phonon thermal conductivity. By combining melt spinning technique with spark plasma sintering Xie et al reported 50 % enhancement (~1.5) in the *ZT* value for p type Bi_2Te_3 nanocomposites [75]. Furthermore, Incorporation of SiC nanoparticles in $Bi_{0.3}Sb_{1.7}Te_3$ improved overall thermoelectric properties and highest *ZT* value of 1.33 obtained at 373K [76]. One of the highest *ZT* value of 1.8 was obtained for bismuth antimony telluride with composition $Bi_{0.5}Sb_{1.5}Te_3$ by a squeezing out technique [77]. Properties of *n*-type Bi_2Te_3 were also improved since then. Fang et al reported improved *ZT* value of 1.21 for the composition $Y_{0.2}Bi_{1.8}Se_{0.3}Te_{2.7}$ synthesized using hydrothermal method [78]. Effect on *ZT* value by various synthesis routes for Bismuth telluride based materials can be seen in a recent review [26].

4.2 Lead Telluride PbTe

Another material known for many decades with promising thermoelectric properties is PbTe [1], [3], [4], [24]. PbTe and PbSe are also presented with the formula PbX, Where X = Te, Se and referred as lead chalcogenides [1]. PbTe as compared with Bi_2Te_3 have lower *ZT* values. On the other hand it is well stable up to higher temperature. Melting point of Bi_2Te_3 is 858 K whereas for PbTe it is 1196 K. Thereby PbTe is favorite in mid temperature waste heat recovery applications [4], [29]. Another advantage PbTe have over Bi_2Te_3 is higher energy band gap (PbTe band gap is is 0.32 eV which is higher than Bi_2Te_3 0.13 eV) which restricts unwanted contributions of minority charge carriers [1]. Both *n*-type and *p*-type PbTe can be synthesized by stoichiometry change. Pb-rich will make *n*-type PbTe and Te-rich will form *p*-type PbTe [79]. Considering the potential of PbTe in thermoelectric applications many attempts were made to further enhance its thermoelectric properties by band structure engineering, alloying, nano-structuring and other techniques [39], [55], [62], [70], [80]–[83]. Hsu et al reported that alloying PbTe with $AgSbTe_2$ lead to exceptional high *ZT* value of 2.2 at 800 K [84]. Heremans et al. utilized distortion of density of states by the use of Thallium impurity to enhance thermoelectric Figure of merit and reported value of 1.5 at 773 K for the composition $Tl_{0.02}Pb_{0.98}Te$ [70]. Enhancement of power factor was made through Cr and I co-doping [85]. Recent reviews on thermoelectric materials advancements discussed various techniques applied to enhance Figure of merit in PbTe based materials [1], [26].

4.3 SiGe Alloys

SiGe alloys are considered promising thermoelectric materials to be used in high temperature TE applications (> 900 K) [4], [86]. SiGe alloys have an advantage of containing non-toxic elements over state of art thermoelectric materials like Bi_2Te_3 and PbTe which are comprised of toxic elements [86]–[88]. Figure of merit *(ZT)* of SiGe is around 1 at 1000 K. However, at room temperature *ZT* is only 0.1 due to considerably large thermal conductivity. Thereby most of the research is focused on minimizing lattice thermal conductivity. In 1981 D. M Rowe showed large reduction of thermal conductivity ~ 28% by decreasing grain size in *n*-type SiGe. Results demonstrates that thermal conductivity was decreased through increased phonon scattering at grain boundaries [89]. In 1991 C. Vining et.al showed further reduction of thermal conductivity in pressure sintered Si-Ge alloys by reduced particle size up to 2 µm. Results demonstrates about 50 % reduction in thermal conductivity but could not improve *ZT* from previous value of 1 due to equivalent decrease in electrical conductivity [90]. This barrier was later crossed via nano-structure approach. *ZT* value of 1.3 was reported by Wang et.al for *n*-type Si-Ge alloy. High power factor was maintained simultaneously with reduction in thermal conductivity [91]. Thermoelectric performance for *n*-type SiGe alloys is usually superior than *p*-type. Recently in p-type SiGe large *ZT* value of 1.3 was obtained thru TiO_2 nano-inclusions and modulation doping [92]. Apart from bulk Si nanowires were also developed with applications towards flexible thermoelectric modules [93], [94]. Another study on Si nanowires suggested controlling roughness can further limit thermal conductivity due to frequency dependent phonon scattering [95]. A recent review by D. Beretta et.al compiled brief research history and advancements in Si-Ge alloys [96].

4.4 SnSe

Efficient and economically viable thermoelectric materials is essential for thermoelectric energy applications. Tin Selenide emerged as high performance thermoelectric material in mid to high temperature range [97]. SnSe compared to other state of art materials exhibit less toxic and more earth abundant materials [98]. SnSe crystalizes in an orthorhombic structure with space group (*Pnma*) below 800 K. In 2014 Zhao et.al reported high Figure of merit ~2.3 at 923 K for SnSe single crystals [99]. This ultra-high Figure of merit is based on very low thermal conductivity (0.2-0.3 W/mK) and large Seebeck coefficient due to large anharmonicity in crystal lattice and multi valley band character [98], [100]. Power factor was further enhanced for hole doped SnSe which was facilitated by multiple electronic valance bands [101]. Considering the large potential of SnSe in thermoelectric applications vast amount of research has been done since the discovery in 2014 [97], [98], [102]–[104]. Initially high *ZT* value was obtained in single crystal SnSe. Thereby to be able to produce it on large scale SnSe was synthesized using alternate methods [102]–[110]. Yiwen et.al reported SnSe poly-crystals were synthesized using powders obtained thru Solvothermal technique.

Which demonstrates enhanced performance in mid temperature range. Overall SnSe exhibit remarkable thermoelectric properties making it an exciting material for energy applications. Chen et.al summarized various strategies and their impact on SnSe transport properties. This review also elaborates solutions to overcome challenges in future enhancement of SnSe TE properties [100].

4.5 Other High Performance TE Materials

Quest for efficient thermoelectric materials started since the discovery of Seebeck effect. Apart from materials discussed above various other classes and materials have been shown great potential for thermoelectric applications [1], [4], [29], [111]. These types/classes of materials are usually based on the possessing specific features in crystal structure or elements. Relationship between crystal structure and thermal/electrical transport properties assisted in understanding linkage between thermoelectric parameters. A brief introduction of some of high performance thermoelectric materials and types is given below.

Skutterudite is well known class of thermoelectric materials [22], [29], [68]. Skutterudite possess general formula type of MX_3 where M = Ir, Co, Rh and X = Sb, As, P. It exhibits octahedral structure with empty space at center so called "void" [4], [87]. These voids referred to as key feature of skutterudites. Void inside skutterudite can be filled with donor or accepter atom. Thereby, charge carriers concentration can be easily optimized. Voids when filled with heavy or light weight atoms produce distortion in crystal lattice thereby acts as phonon scattering centers [1], [112], [113]. Thus leads to low lattice thermal conductivity. The effect of multiple filler atoms on skutterudite based Co_4Sb_{12} was studied by Jennifer et.al. [112] Thermoelectric properties were significantly enhanced by reduction in thermal conductivity and *ZT* value of 1.3 was achieved. Other studies also showed significantly improved thermoelectric properties [112], [114]–[117].

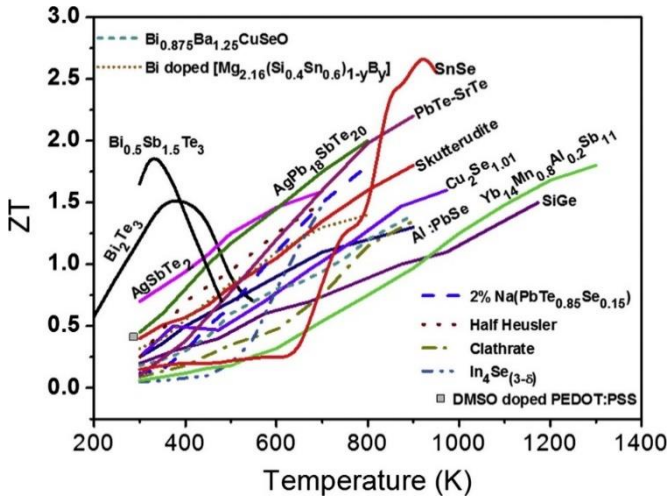

Figure 1. 7 Figure of merit values for state of art thermoelectric materials as a function of temperature [Reprinted with permission Copyright Elsevier Ref 87]

Clathrates is another class of thermoelectric materials which also falls in the type of caged like compounds like skutterudite [4], [29], [87], [118]. Clathrates exhibit general formula $A_xB_yC_{46-y}$ [118]. Clathrates like skutterudite have voids which can be filled with guest atoms. Guest atoms works as rattlers which enable low lattice thermal conductivity. Based on atoms coordination system Clathrates are divided into two types Type1 Clathrates and Type2 Clathrates. Clathrates have been extensively studied for thermoelectric energy applications [118]–[123]. High Figure of merit was obtained in $Ba_8Ga_{16}Ge_{30}$ (ZT = 1.3) thru Czochralski technique [124]. Falmbigl et.al reported improved Figure of merit value of 0.9 through band tuning in type 1 clathrate [125].

Another important class of thermoelectric materials are Half-Heusler alloys (HH)[29], [126]. Half-Heusler are intermetallic compounds exhibiting general formula XYZ [87], [127]. Where X is usually rare earth element or nobel/ transition metal and Y is noble or transition metal and Z is main group element. Half-Heusler compounds are renowned for stability at higher temperatures and strong mechanical properties [6], [127]–[130]. Recent developments in Half-Heusler compounds are compiled by Chen et.al and Huang et.al [6], [131]. Figure. 1.7 Shows ZT values with respect to temperature of various class of thermoelectric materials [87].

Chapter 2: Characterization Techniques and Synthesis Process

This chapter is devoted to the synthesis process and characterization techniques used in this thesis. In the start we will discuss overview and important stages of synthesis process. Later we will present basic working principle of characterizations techniques along with data analysis details.

1. Synthesis Process.

All materials were synthesized using melt and anneal method followed by spark plasma sintering. High purity starting materials usually in the form of powders were weighed in stoichiometric amounts and dry mixed. After dry mixing starting materials were then inserted in the quartz tubes. These quartz tube were then evacuated and sealed. For heat treatment these tubes were then placed in heating furnace. Heating scheme was carefully selected. For the case of $CuGaTe_2$ heating scheme is displayed in Figure 2.1 (a). After heat treatment obtained ingots were fine crushed into powders with mortars. Powder obtained was pressed into pellet and sintered using Spark Plasma Sintering (SPS). Spark Plasma Sintering or field assisted sintering is the method used for consolidation of powders and offers multiple advantages e.g. rapid sintering, less grain growth and can be applied to sinter wide range of materials [132], [133]. Schematic process of SPS can be seen in Figure 2.2. Spark Plasma Sintering (SPS) utilizes uniaxial pressure simultaneously along with electric current to achieve rapid densification. Effect of heating rate, applied pressure and role of current in SPS is reviewed by Munir.et.al [134]. SPS heating scheme is displayed in Figure. 2.1 (b). Sintered samples were then cut and used for characterizations. A schematic of various steps in synthesis process are shown in Figure. 2.3.

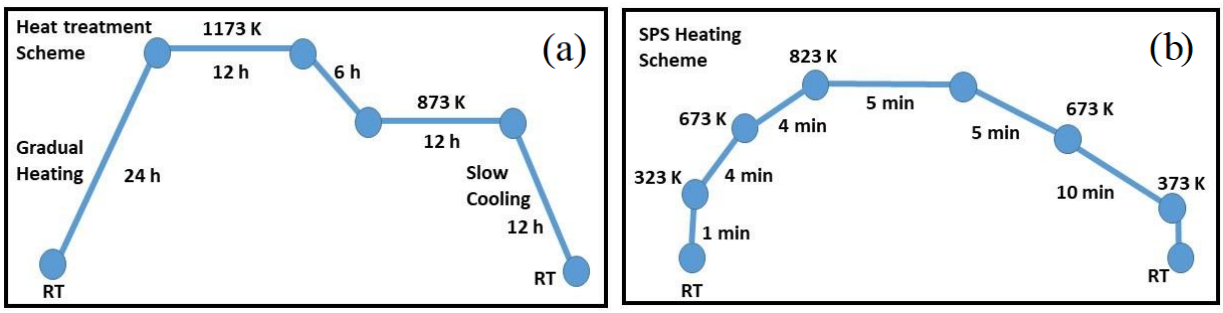

Figure 2. 1 (a) Heat treatment scheme (b) SPS heat treatment scheme, RT represents room temperature

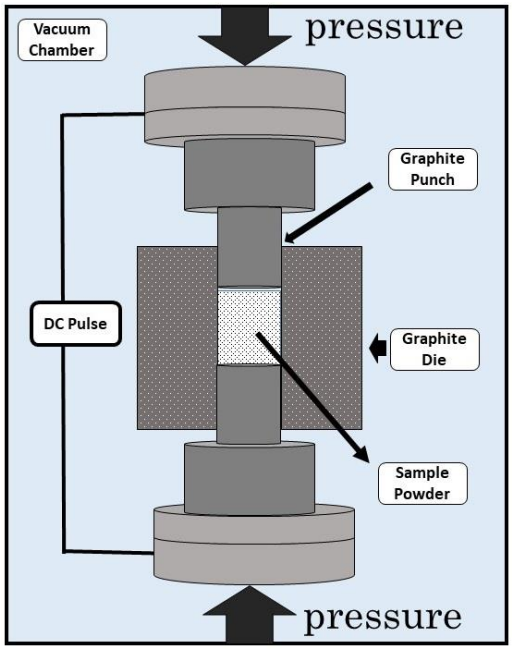

Figure 2. 2 Schematic working of Spark Plasma Sintering

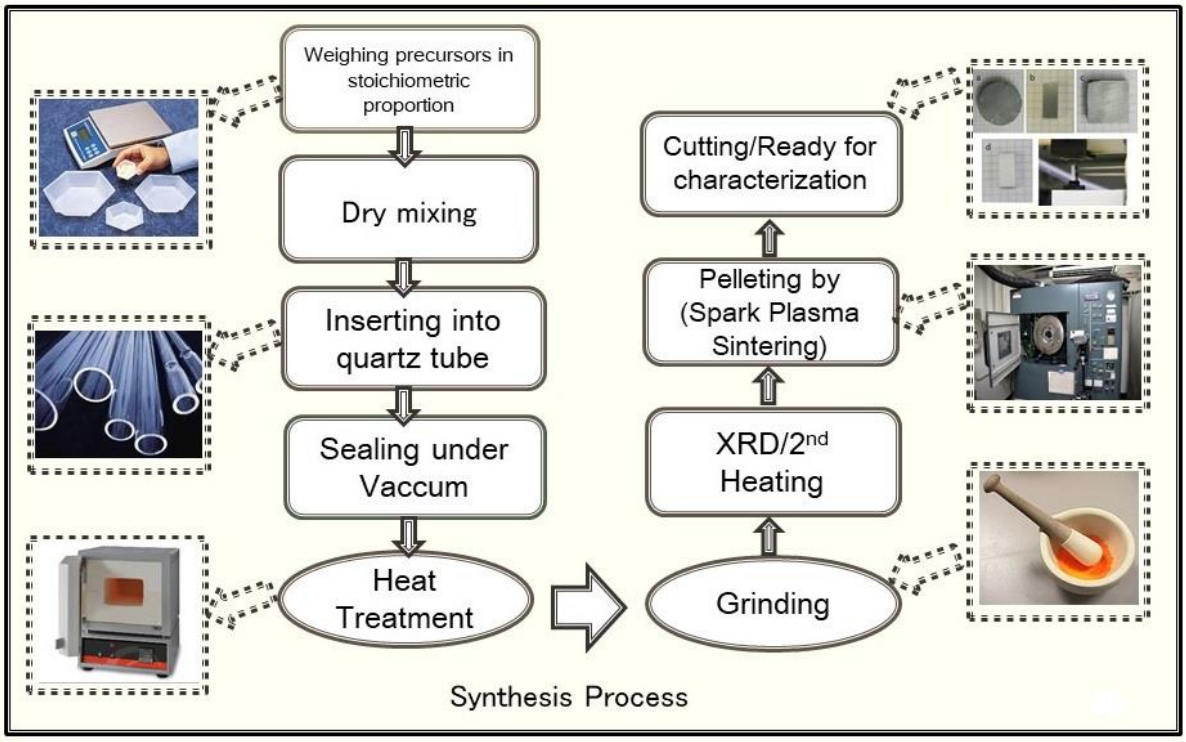

Figure 2. 3 Shows various steps and process involved in solid state reaction synthesis of a material

2. Laser Flash Analysis (LFA)

Thermal conductivity measurements were carried out using Laser flash analysis (LFA). Sample is prepared in the form of thin disk (thickness~ 2mm, diameter ~ 10mm). Both round and square samples can be measured using LFA. Measurements are performed in controlled atmosphere by heating the sample from one side with finite energy pulse and infrared detector on the other side of the sample measure the change in temperature. Schematic illustration of LFA is seen in the Figure 2.4. The typical output signal (red line) also called thermogram is shown in the Figure 2.5. Thermogram is the plot between change in back side temperature and time. Thermal diffusivity (λ) is obtained by the formula shown in Figure 2.5. In the formula $t_{0.5}$ represents half rise time and d^2 is the cross sectional area. Thermal conductivity is then calculated by the product of specific heat (C_p) thermal diffusivity (λ) and density (D) of sample.

$$\kappa = C_p \ \lambda . \mathrm{D}$$

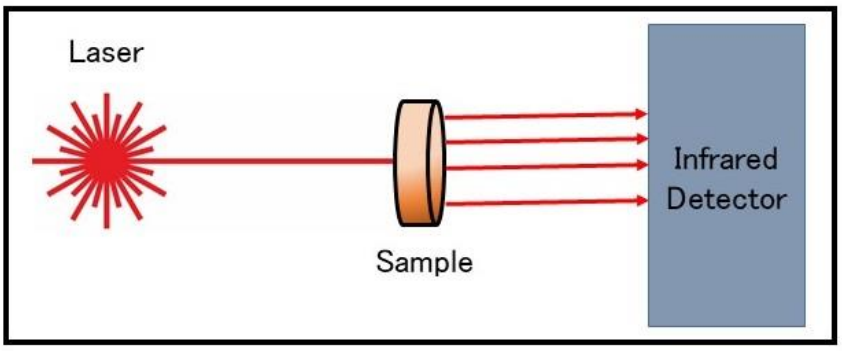

Figure 2. 4 Schematic illustration of working principle in laser flash analysis (LFA)

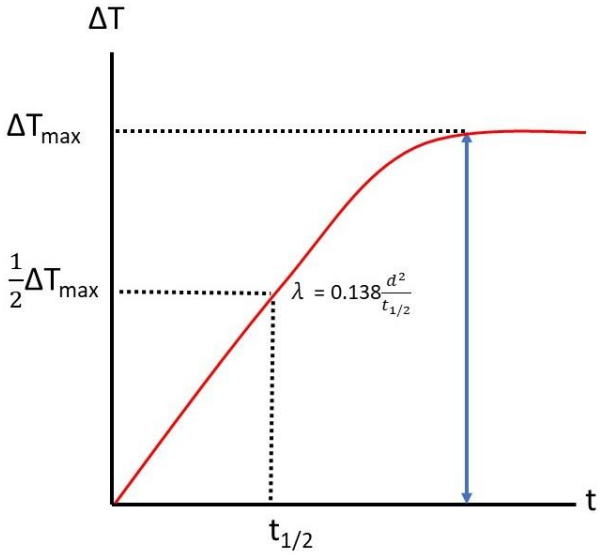

Figure 2. 5 Typical output signal also called thermogram obtained in LFA

3. Seebeck Coefficient and Electrical resistivity Measurement

ZEM-2 have been used to measure electrical resistivity and Seebeck coefficient simultaneously. A schematic working of ZEM-2 is shown in the Figure 2.6. A rectangular sample with dimension of 2 mm x 2 mm x 8 mm is required for the measurement. Sample is placed vertically between the upper and lower block. Lower block also serve as a heater. For Seebeck coefficient, temperature is measured at two points (Hot side temperature, T_h and Cold side Temperature, T_c) by two thermocouples which are pressed on the side of rectangular sample to get temperature gradient (ΔT). Seebeck voltage (ΔV) is also measured by the thermocouples as shown in Figure 2.6. Resistivity is measured by four probe method. For temperature dependent data sample is heated by infra-red image furnace. For homogeneous temperature sample is shielded by a nickel cover. Seebeck coefficient and electrical resistivity is then obtained using following equations.

$$S = \frac{\Delta V}{T_h - T_c}$$

,

$$\rho = \frac{V}{I} * \frac{W * L}{d}$$

where W x L is cross sectional area of the sample and d is separation between the two probes.

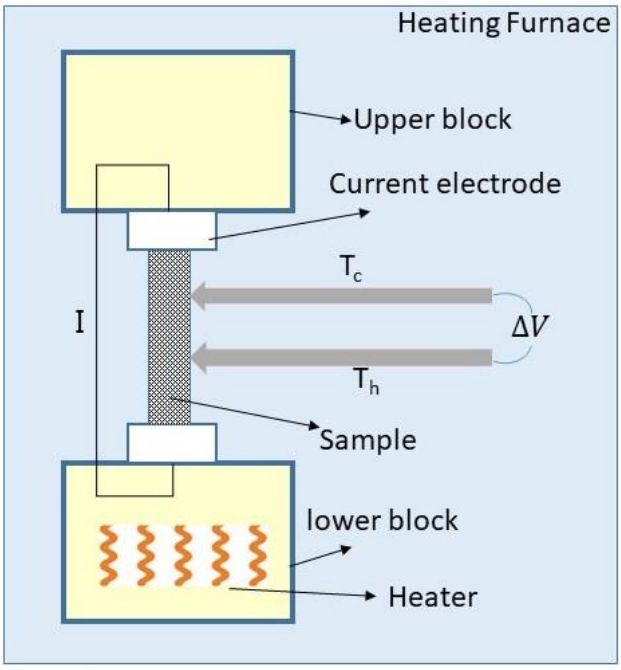

Figure 2. 6 Schematic working of Seebeck and resistivity measurement apparatus ZEM-2

4. Electron Probe Micro Analyzer (EPMA)

Electron Probe Micro analyzer (EPMA) is a powerful tool for elemental analysis of a compound. EPMA has ability to scan materials up to a micro area (5 µm). EPMA is non-destructive analysis technique and can be applied analyze wide range of materials. As shown in the schematic structure of EPMA in Figure 2.7 (obtained from [135]). EPMA consists of an electron source and number of electromagnetic lenses to generate a focused electron beam to interact with the specimen. Samples are required to be well polished and mounted on 1-inch epoxy as shown in left bottom of the Figure. Non-conductive samples are also required to be coated with carbon. In EPMA, a fine polished sample is irradiated with a fine beam of electron generating characteristic X-rays, secondary electrons and back scattered electrons. These X-rays are unique to an element are then collected by highly sensitive wavelength dispersive spectrometers (WDS). More information regarding morphology is obtained by measuring intensities of Back scattered electrons (BSE) and secondary electrons (SE). BSE and SE are useful in imaging a surface also provides information on composition of material.

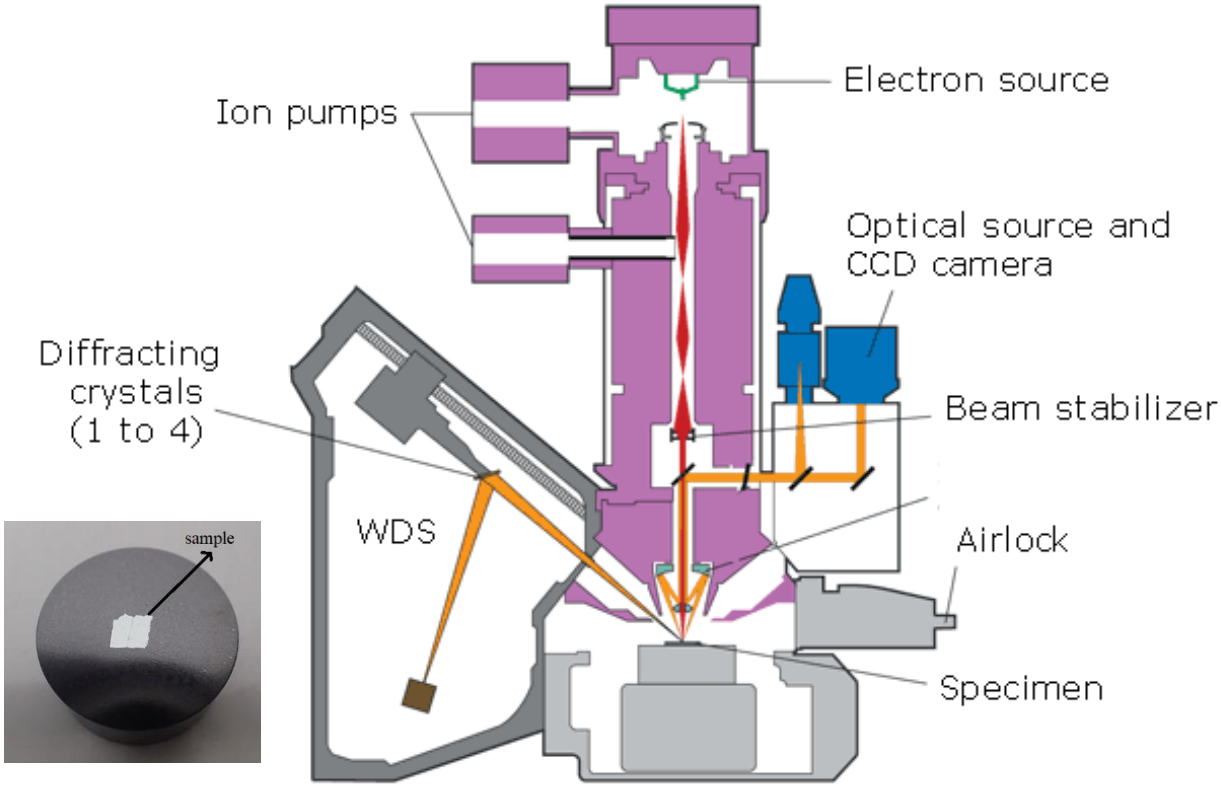

Figure 2. 7 A schematic of Electron micro probe analysis (EPMA). A fine polished sample used for analysis is shown in left bottom Ref [135]

5. Magnetic Property Measurement System (MPMS)

Magnetic properties of samples were measured by using a superconducting quantum interference device magnetometer, MPMS-5S (Quantum Design, Co.). Temperature dependence of magnetization was measured in the temperature range of 5-330 K. Field dependence of the magnetization was measured from 0 to 50 kOe. MPMS is a powerful tool for analyzing magnetic properties of materials. Essential components of MPMS are temperature control system, superconducting SQUID amplifier system and computer operating system. Usually sample is wrapped by thin plastic sheet and enclosed in plastic straw and attached with sample rod. Then Sample rod is inserted in electronic control assembly. To get the correct value of magnetic moment Full DC scan is recommended. This is to ensure all the coils can be able to sense magnetic moment of specimen. Measurements are performed by moving the sample through superconducting sensing coils as shown in Figure 2.8 [obtained from [136]]. When sample is moved through the coils an induced electric current is developed in the coils due to magnetic moment of the sample. The amount of change in current cause change in SQUID voltage which is directly proportional to magnetic moment of sample.

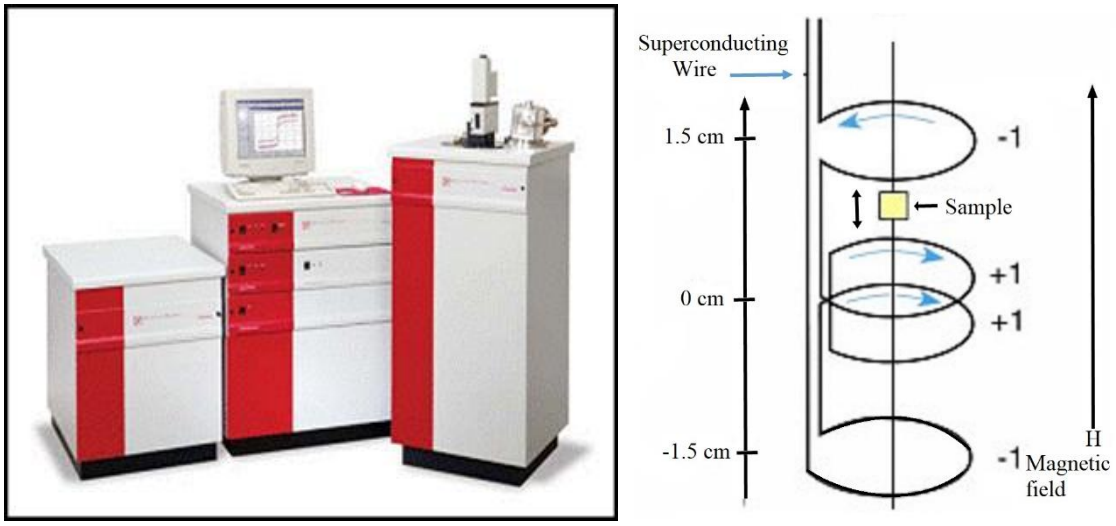

Figure 2. 8 Magnetic property measurement system (MPMS) and superconducting pick up coil on (left) Ref [136]

6. Physical Property Measurement System (PPMS)

Carrier concertation and Hall coefficient was measured by Physical Property Measurement system (PPMS). Measurement was done under the applied current of 10 mA and scanning magnetic field from -70 kG to 70kG. AC transport Measurement system (ACT) and Thermal transport option (TTO) in PPMS is used to measure Hall effect and low temperature thermoelectric property measurements respectively. For Hall coefficient measurement both four and five wire configuration are available in ACT option. Sample is mounted on AC transport Puck (sample holder) as shown in Figure 2.9 [obtained from [137]]. Then AC transport puck is inserted into cryostat chamber for measurements. Hall Resistivity as a function of magnetic field is measured and using below equations hall coefficient and carrier concentration was estimated.

$$R_H = \frac{\rho_H}{H}$$

$$R_H = \pm\frac{1}{ne}$$

Where R_H is Hall Coefficient, ρ_H is hall resistivity and n is carrier concentration.

.

Figure 2. 9 shows physical property measurement system (PPMS) and AC Transport Puck used as sample holder on the right side Ref [137]

Chapter 3: Mn Incorporated $CuGaTe_2$: Power Factor Enhancement

1. Background

Generally, dimensionless Figure of merit, $ZT = S^2\sigma T/\kappa$ is used to evaluate TE material. Where S is Seebeck coefficient, σ is electrical conductivity, κ represents thermal conductivity and T is for absolute temperature [22]. Commonly used techniques to elevate ZT value for developing efficient thermoelectric materials are briefly discussed in chapter 1. These techniques are being applied in wide range of materials. However, ZT value is restricted for a certain period of time. It appears we have extracted possible improvements from these techniques already. For example, after discovery of Seebeck effect, Bi_2Te_3, was known to be the best thermoelectric material at room temperature with ZT value of ~1 [62]. This value was limited to 1 for long period of time. Then, this barrier was crossed with the help of Nano structuring [62]. Thus, for further improvement it is necessary to discover new TE materials as well as to develop novel strategies and mechanisms [2]. In this regard, we studied the method of magnetic enhancement towards power factor in chalcopyrite type compounds. Motivation behind this research work comes from previously obtained large power factor around 1 $mWK^{-2}m^{-1}$ in carrier doped $CuFeS_2$ [11]. It has been suggested that origin of this high power factor was related to charge carriers and magnetic moments interactions. The purpose of this study is to understand mechanism of power factor enhancement in dilute semiconductors as well as to investigate if this kind of magnetic interactions can be applied to other thermoelectric materials as well. In this regard we studied Mn ion doping in similar type of chalcopyrite type compound $CuGaTe_2$.

2. Literature Review

We chose $CuGaTe_2$ because it exhibit similar tetragonal structure to that of $CuFeS_2$. Secondly $CuGaTe_2$ has a large potential to be used in TE devices in near future. $CuGaTe_2$ was recently discovered as a potential candidate for thermoelectric applications. Plirdpring et.al. reported remarkably high ZT value of 1.4 at 950 K [10]. However, this value was not achieved afterwards. But the study opened an opportunity for chalcopyrite type materials for thermoelectric applications. Since then many studies were done on $CuGaTe_2$ based compounds reporting good thermoelectric properties. For example, $CuGaTe_2$ composite with Cu_2Se showed remarkably reduced values of thermal conductivity and at the same time improvement in electrical

conductivity which led to 74% improvement in *ZT* value [138]. $CuGaTe_2$ exhibit high values of figure of merit at considerably higher temperature region (>800 K) and show poor performance at mid temperature region (500-700 K). Thereby, large effort was put towards enhancing thermoelectric properties of $CuGaTe_2$ in the later region. Yusufu et.al. reported *ZT* value of 0.7 at 700 K by replacing Cu with Ag. This enhancement was owed to lower lattice thermal conductivity. [139]. Compared with an ideal thermoelectric material chalcopyrite type materials have large thermal conductivity. Jiawen et.al showed 75% reduction to thermal conductivity. It was achieved via generating strain fluctuations in the matrix of $CuGaTe_2$ by means of mass difference between substituted elements [14]. Another report showed more than 70 % of reduction in thermal conductivity by combined doping effect of Gd and Te [140]. Introducing graphite nano-sheets in $CuGaTe_2$ matrix showed positive effect in simultaneously altering electric as well as thermal transport properties and led to around 20% *ZT* improvement [141]. An effort to decrease thermal conductivity using nanostructure effect was done which showed positive impact on thermal conductivity, However electrical properties were adversely effected, Hence no overall improvement was observed by Kumagai et.al [16]. Seebeck coefficient improvement was shown by Li et.al by In substitution at Ga site [15]. Numerous other studies also reflect the capability of chalcopyrite $CuGaTe_2$ based compounds to be used as potential thermoelectric material in near future [142]–[146].

3. Abstract

In this Chapter we present results of thermoelectric properties of $CuGa_{1-x}Mn_xTe_2$ where $x = 0.0$, 0.01, 0.02, 0.03. We synthesized Mn doped $CuGaTe_2$ by melt and anneal method followed by spark plasma sintering. All samples synthesized were phase pure and exhibit tetragonal structure which was confirmed with Powder X-ray diffraction technique. Furthermore Mn^{2+}/Ga^{3+} substitution was confirmed by increase in lattice parameters values. This substitution was supported by further evidence obtained from Hall measurements and magnetic properties analysis. Thermoelectric properties were then evaluated and analyzed. Large and improved power factor obtained after Mn substitution in wide temperature range. Role of charge carriers and magnetic moment of Mn interactions towards this improvement in power factor is discussed in detail. Large negative wises temperature was obtained in magnetic susceptibility. Which indicates strong antiferromagnetic interactions on Mn spins. We then performed magneto transport measurements and observed distinct anomalous Hall Effect. Which reinforces contribution of magnetic moment and charge carriers interactions towards enhancement in power factor. We obtained *ZT* value of 0.83 for $CuGa_{0.99}Mn_{0.01}Te_2$, which is 40 % enhancement to that of pristine sample. All results clearly indicates carrier and magnetic moment co-relation plays an essential role in enhancement of power factor.

4. Experiments

Polycrystalline samples of $CuGa_{1-x}Mn_xTe_2$ where $x = 0.0, 0.01, 0.02, 0.03$ were synthesized using melt and anneal method followed by Spark Plasma Sintering. Synthesis process is presented in Chapter 2 section 1. Densities of all synthesized samples were measured by the mass and volume ratio method. Relative density values were in the range of 98-99 %. See Table 1. Structural analysis was performed using RINT TTR-3 diffractometer (Rigaku Co., Akishima, Tokyo, Japan) with Cu Ka radiation. Cathode current of 150 mA with an accelerating voltage of 40 kV was used. Lattice parameters values were obtained by performing Rietveld Refinement using FullProf Suite Software. Thermal properties were analyzed using Differential Thermal Analysis (DTA) and thermogravimetric analysis (TG) measured by Thermo-Plus EVO (Rigaku Co.). Thermoelectric properties, Seebeck Coefficient and Electrical resistivity were measured using ULVAC ZEM-2 with a bar shaped sample with the dimensions of 3 mm x 3 mm x 8 mm. Laser Flash method (ULVAC TC7000) is used to measure thermal diffusivity of samples. Thermal conductivity was then measured from equation $\kappa = \lambda . Cp . \rho$, Cp value was measured by DSC. Below room temperature TE properties were measured by using Quantum Design Physical Property Measurement System (PPMS). Magnetic properties were measured using superconducting quantum interference magnetometer, MPMS-5S (Quantum Design, Co.). Temperature dependent magnetization was measure in the range of 5-323 K under constant field of H = 50 kG.

5. Structural Analysis

Powder X-ray patterns of $CuGa_{1-x}Mn_xTe_2$ where $x = 0.0, 0.01, 0.02, 0.03$ are presented in Figure 3.1 (a) All samples were found to be phase pure and exhibit tetragonal structure with space group *I-42d.* All the peaks were indexed with that of chalcopyrite structure (PDF#047-1454). To check how lattice parameters were changed after Mn substitution Rietveld refinement analysis was performed and are shown in Figure 3.1(b). Rietveld refinement was done for structural analysis by using FullProf Suite software. Tripled pseudo-Voigt function was employed to analyze peak shape. Brag positions are shown on black line which agreed with synthesized structure peaks. Refinement results depicts single phase chalcopyrite structure for all nominal samples. Refined Lattice parameters were plotted against Mn percentage doping as shown in Figure 3.1 (b). Lattice parameters were linearly increased with increase in Mn doping % almost obeying Vegard law. Linear increase in lattice parameters indicates successful substitution of Mn^{2+} at Ga^{3+} site. Further evidence of this substitution (Mn^{2+}/Ga^{3+}) were obtained from Hall measurements and Magnetic properties. Values of lattice parameters and density are listed in Table 1. A schematic structure of $CuGaTe_2$ along c-axis is shown in Figure. 3.1 (c) [20].

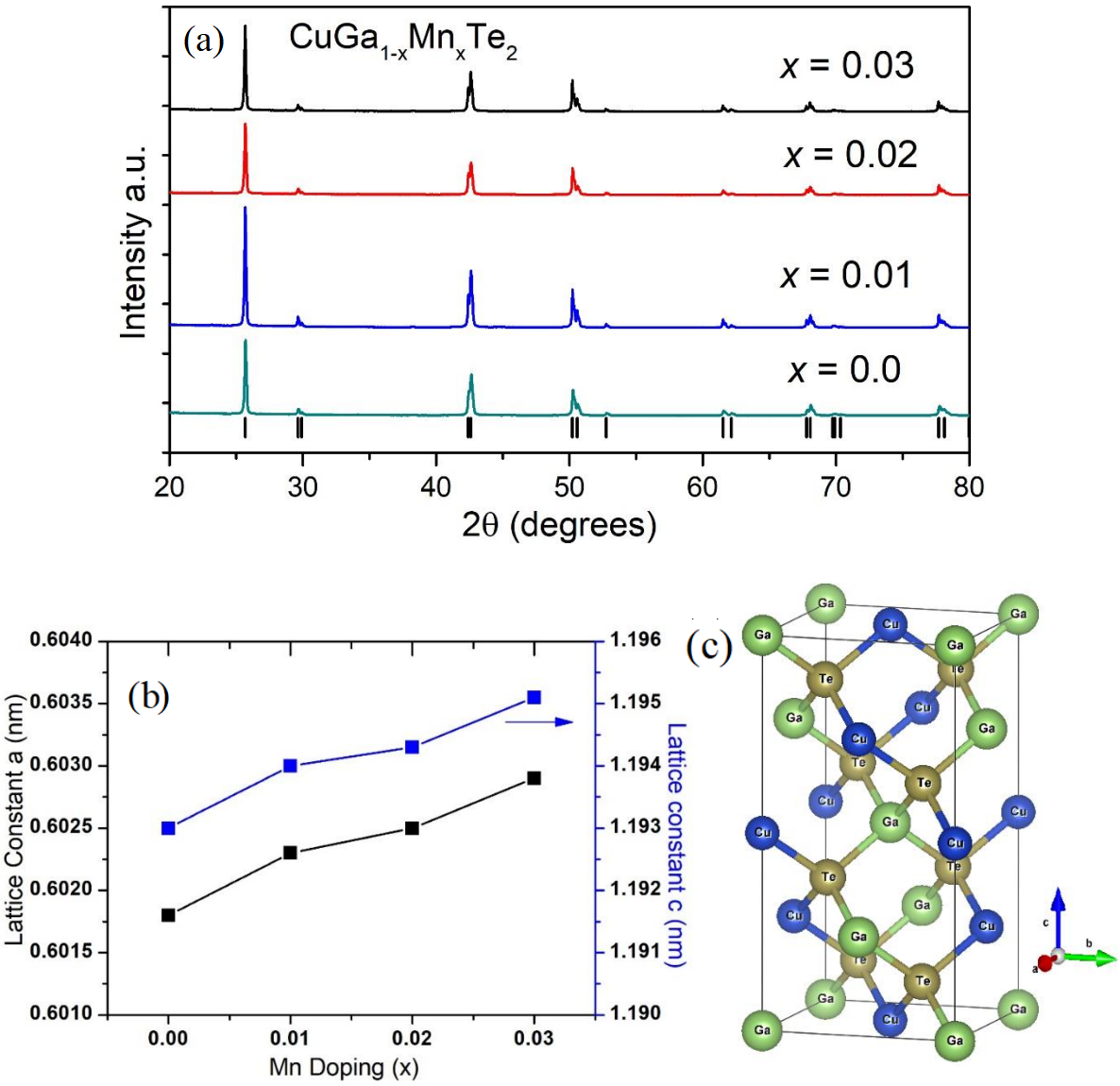

Figure 3. 1 (a) Powder XRD patterns of polycrystalline samples of $CuGa_{1-x}MnxTe2$ (x = 0-0.03). At the bottom of the XRD patterns we showed standard reference card data. (b) Lattice constant dependence on Mn doping concentration (c) Schematic crystal structure of chalcopyrite $CuGaTe_2$ shown along c-axis [21].

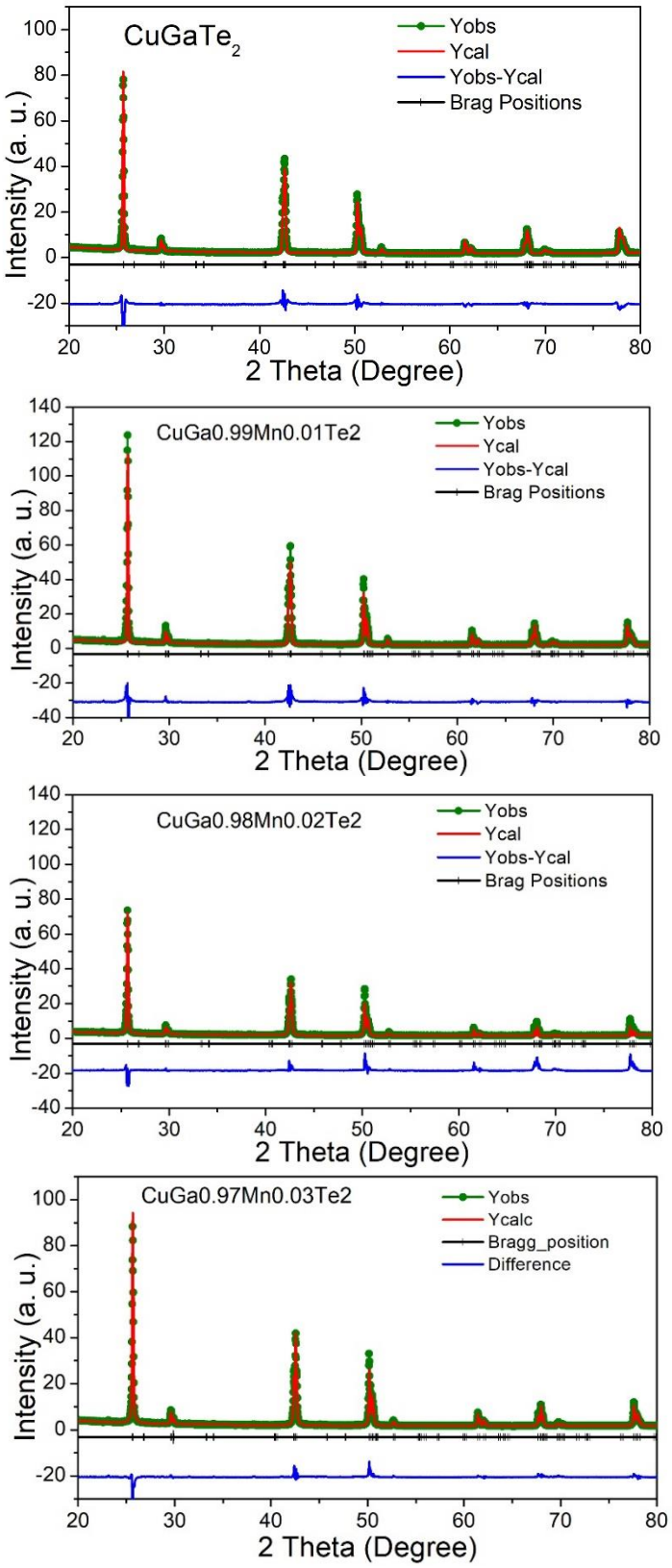

Figure 3. 2 The results of Rietveld refinement for the $CuGa_{1-x}Mn_xTe_2$, x = 0.0, 0.01, 0.02, 0.03 including the observed and calculated diffraction data along with their difference

Table 1 shows values of lattice constants, and relative densities for all the nominal compositions.

Sample	Density (% Th)	Lattice parameters	
		a(nm)	c(nm)
$CuGaTe_2$	99%	0.6018	1.1930
$CuGa_{0.99}Mn_{0.01}Te_2$	98%	0.6023	1.1940
$CuGa_{0.98}Mn_{0.02}Te_2$	99%	0.6025	1.1943
$CuGa_{0.97}Mn_{0.03}Te_2$	98%	0.6029	1.1951

6. Thermoelectric Properties

6.1 Electrical conductivity, Seebeck and Power factor.

Temperature dependent electrical conductivity and Seebeck coefficient values are presented in Figure 3.3 (a) and (b) respectively. Upon increasing temperature above 500 K electrical conductivity showed increase. This indicates an intrinsic semiconducting behavior. Which is attributed to thermal excitation of charge carriers above 500 K. Electrical conductivity values for pristine sample was found to be in good agreement with literature data [18], [138], [147], [148]. Large improvement in electrical conductivity value is observed after Mn substitution as seen in Figure 3.3 (a). At 325 K, value of σ increased from 2.49 k $(\Omega\text{-cm})^{-1}$ for pristine $CuGaTe_2$ to 25.26 k $(\Omega\text{-cm})^{-1}$ for sample composition $CuGa_{0.97}Mn_{0.03}Te_2$. This increase in conductivity is attributed to increase in charge carrier concentration n, as a result of Mn^{2+} substitution at Ga^{3+} site. In case of Mn substituted samples, temperature dependence of electrical conductivity revealed shift from degenerate to intrinsic semiconducting behavior. Below 500 K electrical conductivity decreases with the increase in temperature while above 500 K, σ increases with increase in temperature. This behavior was also seen in literature for chalcopyrite type compounds. Although, this shift is weak as compared to silver doped chalcopyrite [18]. In Figure 3.3 (b) Seebeck coefficient values are presented. All samples exhibit positive values of Seebeck. This indicates *p*-type behavior where holes are majority charge carriers. Temperature dependence of Seebeck coefficient revealed typical semiconducting behavior. Interestingly, Seebeck exhibit high values even after Mn substitution. For example, at 670 K Seebeck coefficient is 280 µV/K for pristine $CuGaTe_2$, but Seebeck coefficient for $CuGa_{0.97}Mn_{0.03}Te_2$ is nearly as large as 230 µV/K, However electrical conductivity at same temperature increased by twofold. As a result, Power factor $S^2\sigma$ is enhanced significantly in the wide temperature range. Temperature dependent graphs of power factor $S^2\sigma$ are displayed in Figure. 3.3 (c). Power factor $S^2\sigma$, for the case of Mn doped samples increased to 0.6-0.9 mW/K^2m. Which is around double of its value compared at room temperature. Moreover, at 670 K power factor further increased to 1.3-1.4 mW/K^2m. This is more than 30 % enhancement from that of pristine $CuGaTe_2$.

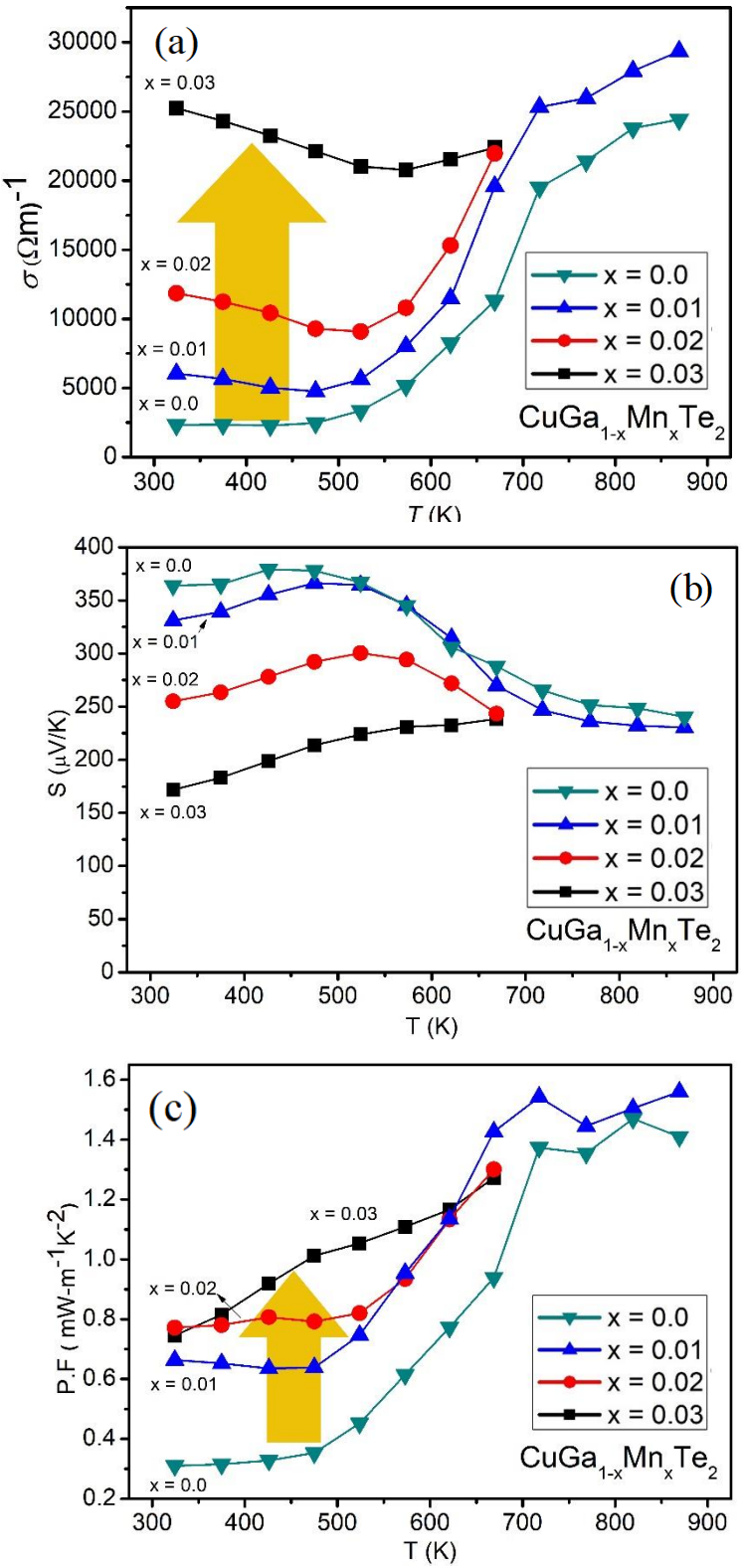

Figure 3. 3 Transport properties for the $CuGa_{1-x}Mn_xTe_2$, $x = 0.0$, 0.01, 0.02, 0.03. Temperature dependent plots of (a) electrical conductivity, σ (b) Seebeck coefficient, S (c) Power factor, σS^2 [21]

For single parabolic band model considering the degenerate semiconductor limit Seebeck Coefficient relationship with carrier concentration and effective mass can is described by Mott formula,

$$S = \frac{8\pi^2 k_B^2}{3eh^2}\left(\frac{\pi}{3n}\right)^{\frac{2}{3}} m^* T$$

Where k_B, h indicates the Boltzmann constant and the Planck's constant respectively, n and m^* represents carrier concentration and charge carrier effective mass. From above equation, Seebeck Coefficient is inversely proportional to the charge carrier concentration and directly proportional to effective mass. This implies that with increase in carrier concentration Seebeck coefficient will decrease automatically. However, for the present case Seebeck stayed at higher values even after hole doping. Here, we propose enhancement in effective mass could be the possible reason which prevented drop in Seebeck Coefficient values. To clarify, we carried out Hall measurements. Figure. 3.4 (a), (b) shows graphs of Hall coefficient and charge carrier concentration. In Figure 3.4 (c) estimated values of effective mass and mobility is displayed.

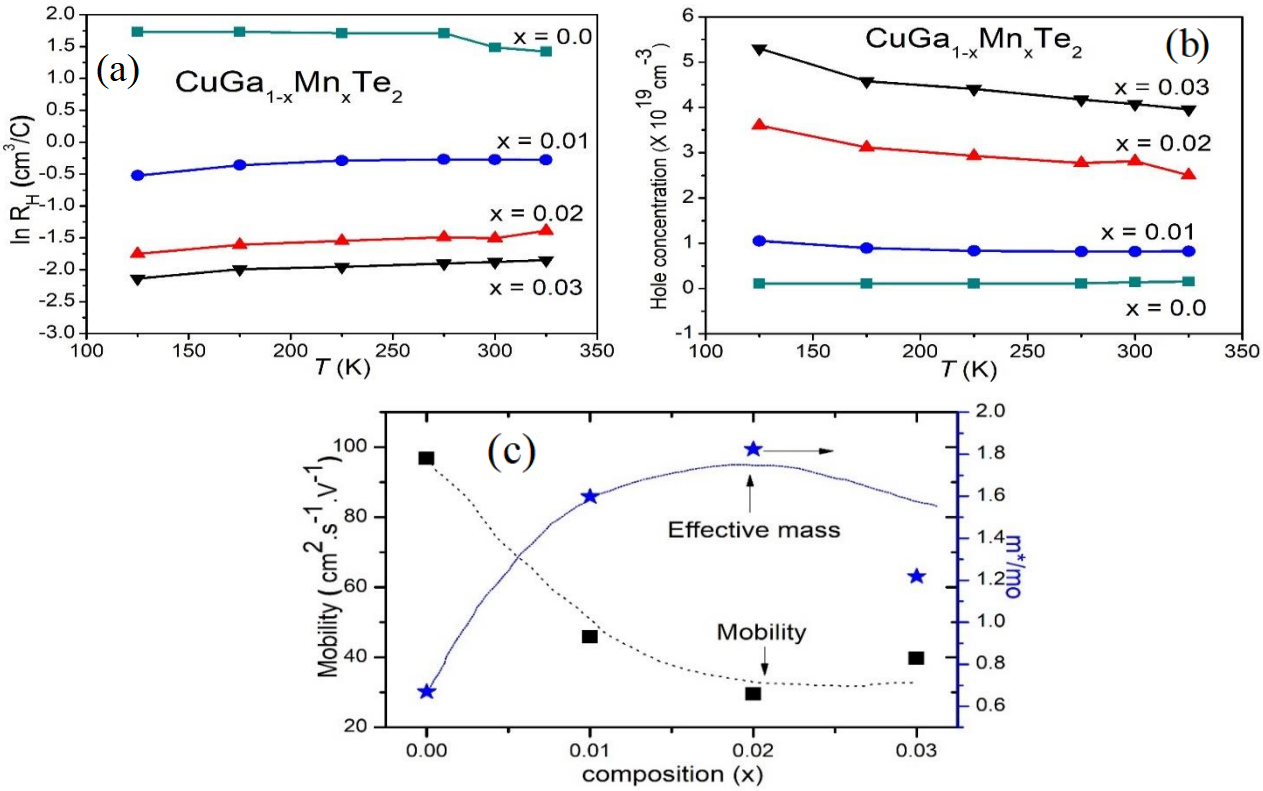

Figure 3. 4 (a) Hall coefficient R_H of $CuGa_{1-x}Mn_xTe_2$ as functions of temperature. (b) Hole concentration as a function of temperature for $CuGa_{1-x}Mn_xTe_2$ (c) Carrier mobility and effective mass in $CuGa_{1-x}Mn_xTe_2$ at 325 K as functions of composition x. Lines in (c) serve as guides for the eye [21].

From Figure. 3.4 (b), It is evident that carrier concentration increased systematically as a result of Mn doping which is consistent with electrical properties as well. Furthermore, this increase in carrier concentration also endorses Mn substitution at Ga site.

In Figure 3.4 (c), the important result is large enhancement in effective mass. Effective mass increased from $0.66m_0$ for $CuGaTe_2$ to $1.82m_0$ for $CuGa_{0.98}Mn_{0.02}Te_2$, where m_0 is the mass of free electron. Therefore, as proposed earlier the most probable reason behind high values of Seebeck effect is this increase in effective mass of carriers by magnetic moment and charge carrier interactions.

6.2 Seebeck vs ln σ Plot

Hall measurement were performed below room temperature therefore effective mass and carrier concentration values for higher temperature are unknown. However, improvement in Seebeck coefficient and power factor was observed in wide temperature range. To clarify this point, we plotted graph between Seebeck coefficient and ln σ as shown in Figure 3.5. According to a theoretical model, relation between Seebeck coefficient and conductivity can be written as [149],

$$S = m(b - ln\sigma)$$

In this equation, b is the parameter which includes the effective mass term, $T^{3/2}(m^*/m_0)^{3/2}\mu$, and $m = k_B/e = 86.14\ \mu$V/K. This relationship described above also been applied for various materials including degenerate semiconductors [150]–[152]. Figure 3.5 show graph between Seebeck vs ln σ at 324 K, 374 K, 426 K and 475 K. The slope of broken and dotted lines is -86.14μV/K as suggested by the model. The negative sign indicates holes as majority carriers. It is clear that data points for doped samples lies above the line to that of pristine sample. This indicates enhancement in the b value (which includes effective mass term).

Increase in effective mass is higher for 1% Mn doped sample as compared with 2 and 3 % doped Mn samples. This is attributed to the decrease in mobility with excess Mn doping. In Figure 3.6, Plots between Seebeck and log of conductivity is plotted up to 669 K.

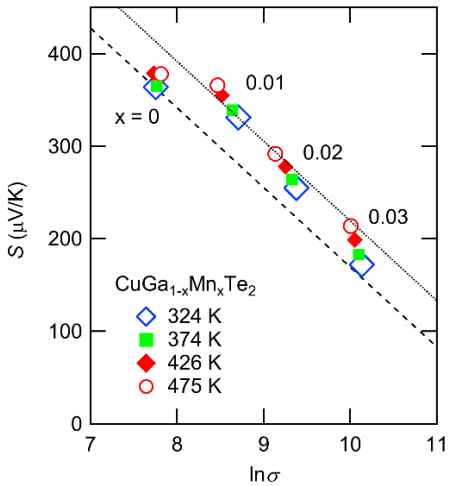

Figure 3. 5 Seebeck coefficient graph with respect to lnσ for $CuGa_{1-x}Mn_xTe_2$ at various temperatures. Slope of broken and dotted lines is -86.14 μV/K, as proposed by the model [21].

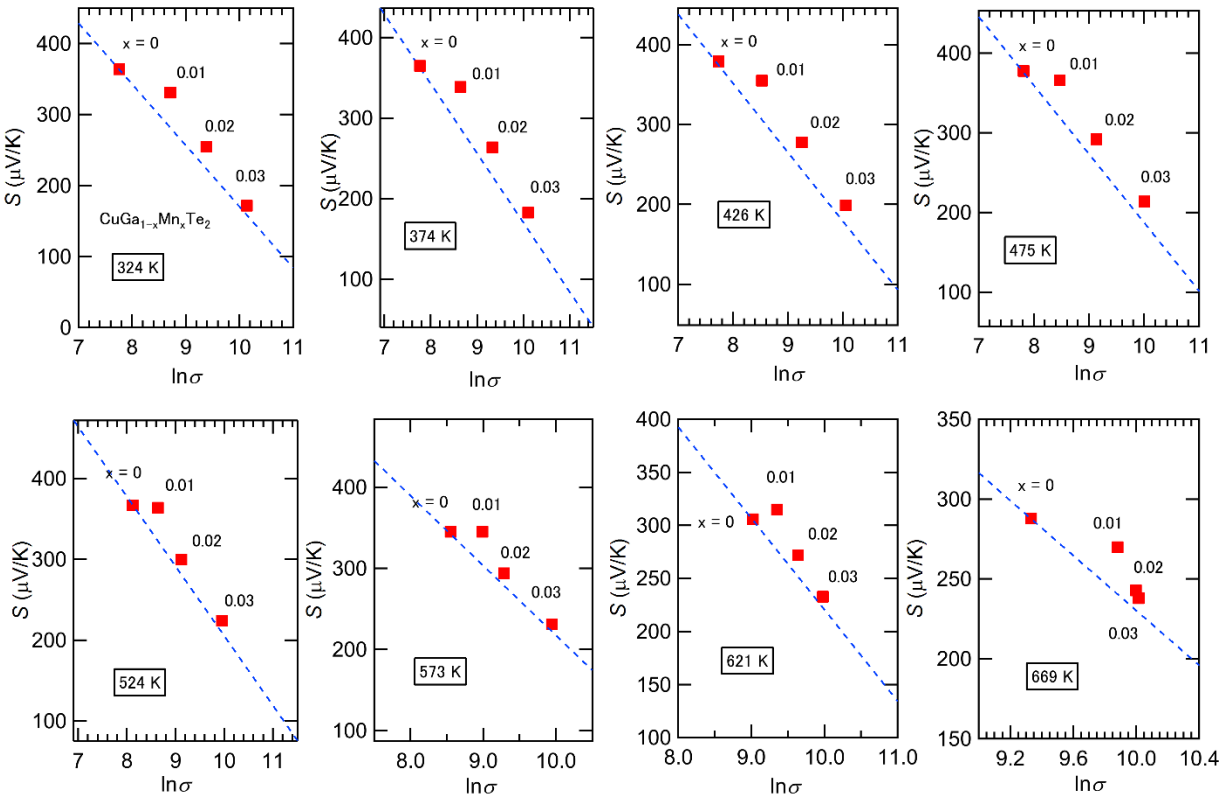

Figure 3. 6 Plot of Seebeck coefficients and $\ln\sigma$ for $CuGa_{1-x}Mn_xTe_2$. Slope of broken lines is -86.14 μV/K, as proposed by the model. [21]

From the relationship described above power factor was evaluated considering the assumption of constant μ and m^* [149]. Observed values of Seebeck coefficient and electrical conductivity was used to calculate power factor of pristine sample. Power factor vs conductivity plots at 324 K, 475 K and 621 K are presented in Figure 3.7. Here, increase in electrical conductivity represents increase in carrier concentration. Solid purple lines in the Figure 3.7 represents calculation based on theoretical model and the maximum values of power factor obtained through carrier concentration optimization, whereas red dots are values of power factors observed in experiment. Figure. 3.7 demonstrates that the observed values of power factor are consistently higher than the optimized values. The enhancement is seen significantly up to 524 K. These results reinforces that enhancement in power factor is larger than which is achievable through carrier tuning. In the next section we will demonstrate strong coupling between magnetic moments and charge carriers through magneto transport results analysis. Previously this type of mechanism was proposed for $CuFeS_2$ [11]–[13]. Furthermore, it has been reported in a theoretical study for $CuFeS_2$, that Seebeck coefficient have larger values for ordered magnetic state as compared with disordered state [153].

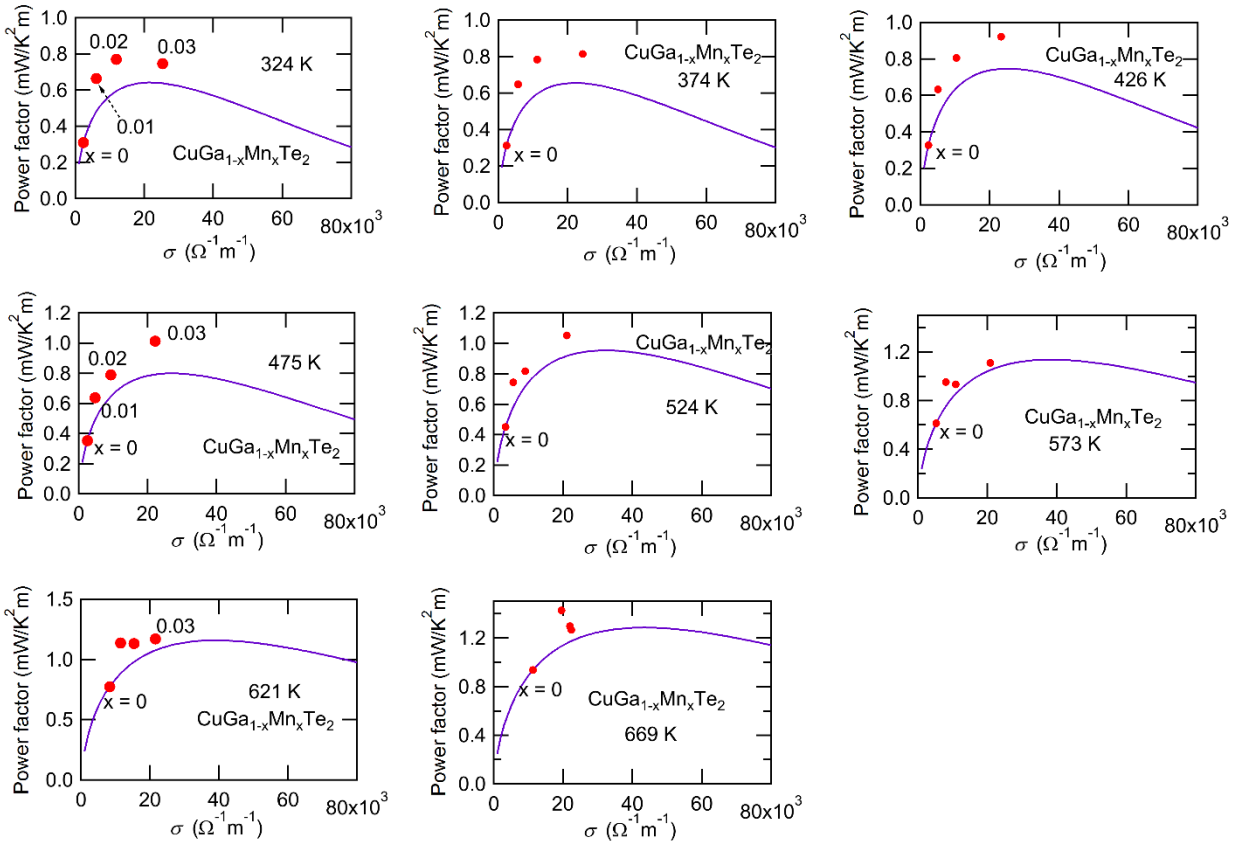

Figure 3. 7 shows plots of power factor dependence on electrical conductivity for the $CuGa_{1-x}Mn_xTe_2$. Purple (solid) lines indicates the calculation on the basis of theoretical model. Red circles indicates observed values of power factor [21].

7. Magnetic Properties

7.1 Magnetic Susceptibility

Magnetic properties were investigated in order to clarify interactions of magnetic moments and charge carriers. Inverse of magnetic susceptibility of $CuGa_{1-x}Mn_xTe_2$ with respect to temperature is shown in Figure 3.8. For a paramagnetic system magnetic susceptibility is usually expressed by Curie Weiss function,

$$\chi_{\mathrm{Mn}} = \frac{C - \theta}{T} + \chi_0$$

Where C is Curie constant, θ is Weiss temperature and χ_0 is temperature independent term. χ_0 is usually originates due to diamagnetism of core electrons. We estimated Mn contribution in susceptibly χ_{Mn} by subtracting χ_0 (susceptibility value measure for pristine ($CuGaTe_2$). Figure 3.8 shows $1/\chi_{\mathrm{Mn}}$ follows a linear function as expected. Weiss Temperature (θ) and effective magnetic moment (P_{eff}) values were obtained by fitting data and are shown in Table 2.

The values of effective magnetic moment are roughly close to the expected values for Mn^{2+}. Weiss temperature exhibit negative values which are usually associated with antiferromagnetic.

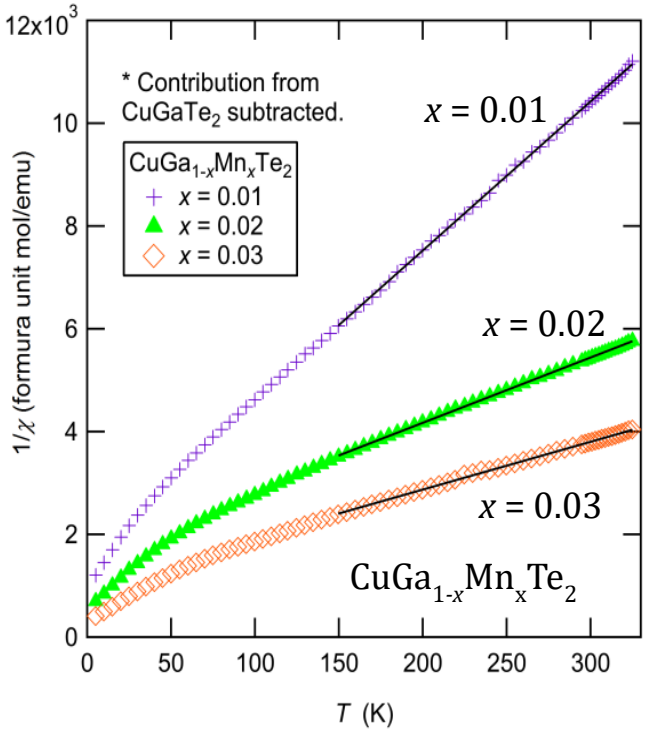

Figure 3. 8 shows temperature dependence of inverse of magnetic susceptibility as a result of Mn ions. $CuGaTe_2$ contribution in measured susceptibility has been subtracted [21]

Table 2 Values of effective magnetic moment, Curie constant and Weiss temperature for $CuGa_{1-x}Mn_xTe_2$ obtained by data fitting.

$CuGa_{1-x}Mn_xTe_2$	C (emu K/mol)	p_{eff}/μ_B	θ (K)
x = 0.01	0.0344	5.24	-59.1
x = 0.02	0.0788	5.61	-129.0
x = 0.03	0.1073	5.35	-108.5

interactions on Mn spins. Weiss temperature show large negative value of 59.1 K for 1% Mn doped $CuGaTe_2$. Usually negative Weiss temperature values are linked with indirect super exchange or antiferromagnetic exchange interactions between magnetic ions. However, it is hard to explain large negative Weiss temperature for very low doped $CuGaTe_2$. Weiss temperature can be written as following.

$$\theta = -2S(S+1)\frac{N_N j}{3k_B}$$

Where, j is exchange interaction between magnetic ions, and N_N is the neighboring magnetic ions number [154]. For $CuGa_{1-x}Mn_xTe_2$ system j value is unknown. Thereby, we supposed it to be similar to $Zn_{1-x}Mn_xTe$, which is -10 K [154], [155]. If we use this value of exchange interaction (j = -10 K). The observed Weiss temperature, θ is reproduced only if $N_N \sim 1$. Since, in $CuGaTe_2$ there are only eight cation sites thereby the large value of Weiss temperature (θ = -59.1 K) is hard to explain on the basis of Mn-Mn interactions. Considering Mn ions are only substituted at Ga site, the distance between Mn-Mn ions would become longer than $Zn_{1-x}Mn_xTe$ system and j value will become much shorter which further contradicts with observed Weiss temperature. Thus, the possible origin of this large negative Weiss temperature is because of interactions between Mn spins and valence or conduction band electrons.

This type of onsite exchange interactions can be explained by sp-d model [154]. These interactions are similar to Kondo type interactions. Theoretically, influence of magnetic impurities were discussed by Kondo [156]. Previously, large thermopower in metallic ferromagnetic $Ga_{1-x}Mn_xAs$ was explained on basis of Kondo model [157]. It has been reported that Seebeck coefficients values for $Ga_{1-x}Mn_xAs$ and are significantly larger than non-magnetic $Ga_{1-x}Be_xAs$ [157]. The origin of this large thermopower was explained by two possible reasons. Firstly contribution from Mn-3d impurity band and secondly Kondo type exchange interaction with similar carrier concentration. They showed that the contribution from Mn-3d band plays the major role. However, for $CuGa_{1-x}Mn_xTe_2$ Mn concentration is smaller to that $Ga_{1-x}Mn_xAs$. Hence, Kondo type exchange interactions would become more important in the present case.

7.2 Magneto-transport properties

To obtain more evidence of correlation between magnetic moment and carriers we measured magneto-transport properties. Hall resistivity can be described as

$$\rho_{xy} = R_o H + 4\pi M R_s$$

Where, M is magnetization and R_o and R_s are constants. The first term in above equation is known as normal Hall effect whereas second term represents anomalous Hall effect (AHE). Large value of AHE has been reported for ferromagnetic materials like, $Yb_{14}MnSb_{11}$ [158], $Ga_{1-x}Mn_xAs$ [159], and $Fe_{1-x}Co_xSi$ [160] and other magnetic semiconductors. Therefore, magnitude of anomalous Hall Effect (AHE) is good indication of magnetic moment and charge carrier correlation. In paramagnetic materials, H is linear to both normal and anomalous Hall term and cannot be separated. However, at low temperature M depends on H non-linearly and it is possible to separate the anomalous Hall term. Therefore, field dependence of magnetization was measured for 3 % Mn doped sample. Magnetization as a function of H at 5 K, 10 K, 15 K, 20 K and 50 K are shown in Figure 3.9 (a). Figure 3.9 (a) demonstrates increase in magnetization with convex curvature for the temperature below 20 K. Figure 3.9 (b) displays Hall resistivity as a function of H. Hall resistivity is linear to H at 325 K having positive slope. This indicates p-type conductivity. When temperature is decreased further, a negative contribution develops

and Hall resistivity becomes nonlinear to H. This result is in agreement with the convex curvature of M at 20 K indicating AHE contribution is dominant. The observed data was then fit with the above equation to separate AHE contribution. Data above H = 50 kG was extrapolated using phenomenological Landau expansion of free energy with equilibrium condition $dF/dM = 0$ [161].

$$F(M) = -HM + \left(\frac{a}{2}\right)M^2 + \left(\frac{b}{4}\right)M^4 + \cdots$$

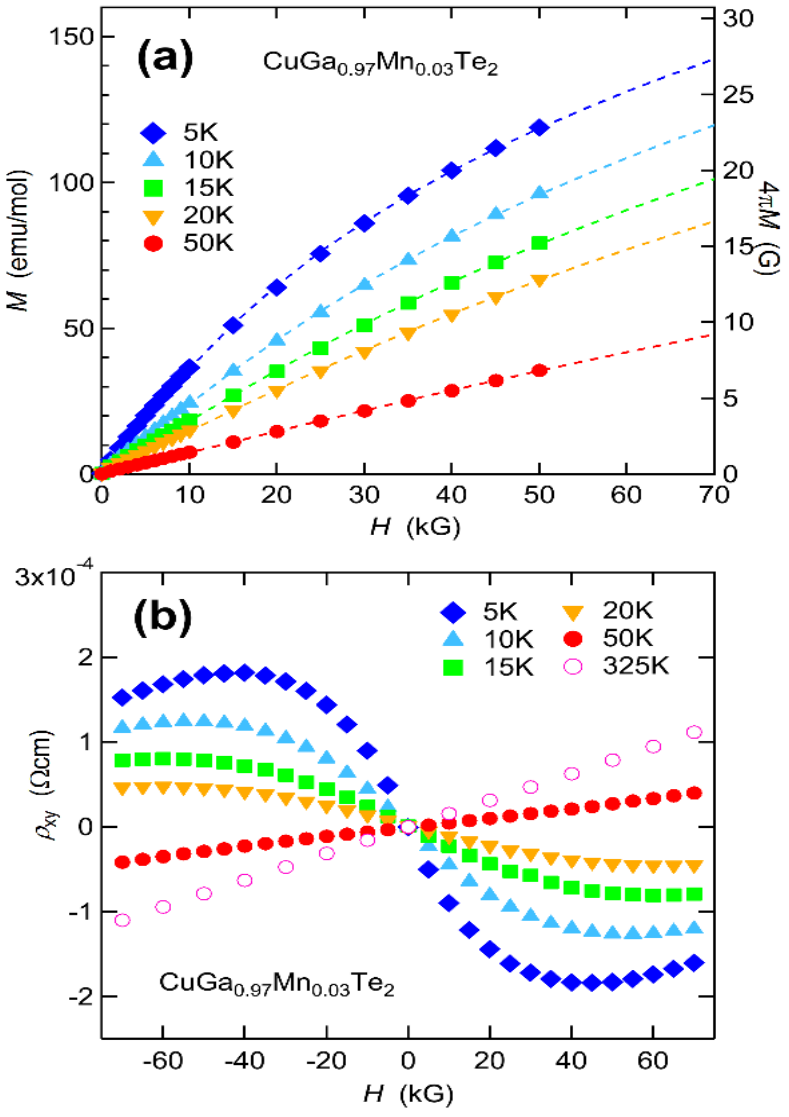

Figure 3. 9 (a) Magnetization as a function of magnetic field H (b) Hall resistivity as a function of magnetic Field (H) for the composition $CuGa_{0.97}Mn_{0.03}Te_2$. Dashed lines indicates Landaus expansion fitting [21].

Dashed lines in Figure 3.9 (a) shows the fitted results. ρ_{xy} was then analyzed using $M(H)$ data and results are displayed for T = 5 K in Figure 3.10. As seen in Figure 3.10 the AHE contribution is multiple of 10^{-4} Ω-cm. This is remarkably large as compared with AHE ~10^{-6} Ω-cm for $Fe_{1-x}Co_xSi$ [160] and also comparable to AHE ~5 x 10^{-4} for $Ga_{1-x}Mn_xAs$ [159]. Negative value of

constant R_S is indicative of antiferromagnetic coupling between magnetic moments of Mn and charge carriers and is in agreement with negative Weiss temperature. The other reason for nonlinear Hall resistivity is existence of multiple carrier bands with different mobilities [162]–[164]. However, for $CuGa_{0.97}Mn_{0.03}Te_2$ we observed positive Seebeck coefficient values down to 5 K as shown in Figure 3.11. Hence, no evidence for multiple carrier bands is observed for the present case. Overall large anomalous Hall Effect is indicative of strong coupling between magnetic moments and carrier correlation.

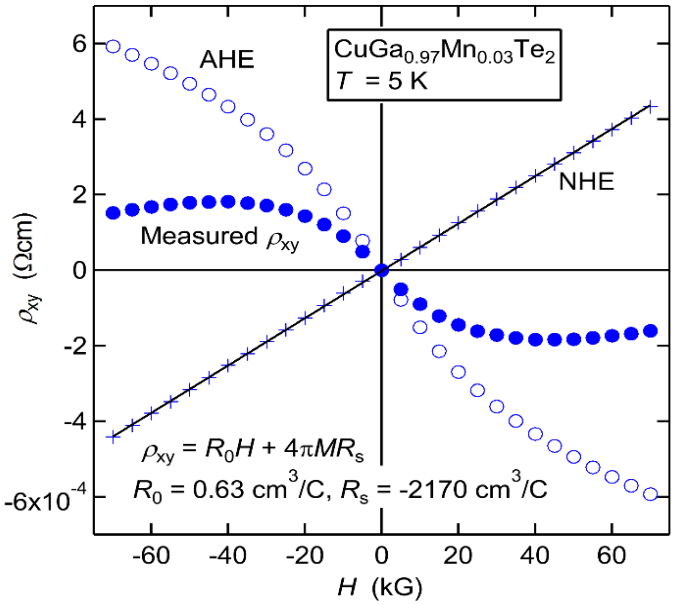

Figure 3. 10 Hall resistivity as a function of H for the composition $CuGa_{0.97}Mn_{0.03}Te_2$. Open and filled circles indicates AHE contribution and measured values of Hall resistivity respectively. Whereas, NHE contribution is represented by crosses in the figure [21].

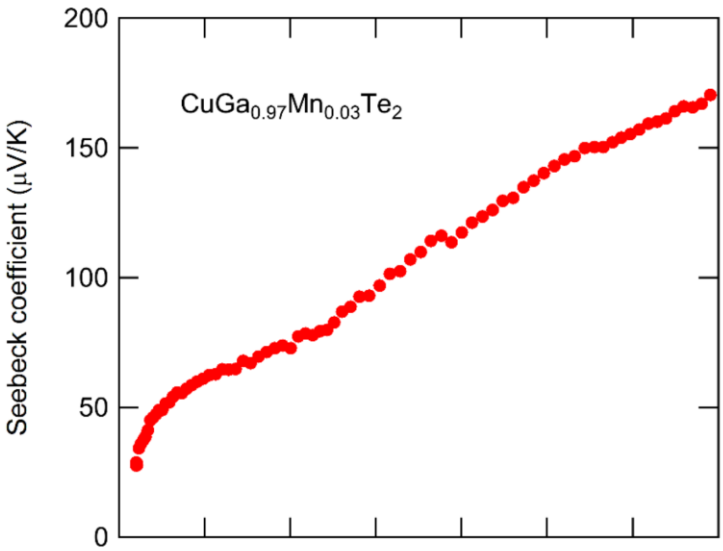

Figure 3. 11 Seebeck coefficient values for $CuGa_{0.97}Mn_{0.03}Te_2$ at low temperature [21].

8. Thermal Conductivity and Figure of merit.

Temperature dependent plots of total thermal conductivity (κ_{tot}), lattice thermal conductivity (κ_{latt}) and electronic contribution towards total thermal conductivity (κ_{el}) are shown in Figure 3.12. As seen in Figure. 3.12 (a) thermal conductivity for $CuGa_{1-x}Mn_xTe_2$ decreases with increase in temperature for all samples. For Mn substituted samples thermal conductivity was decreased compared to the pristine sample. This reduction is seen in whole temperature range. This decrease in thermal conductivity is attributed to enhanced phonon scattering. Mn substituted at Ga site acts as an effective scattering center. For $x = 0.01$, lowest thermal conductivity value of 1.6 $Wm^{-1}K^{-1}$ was observed. Electronic thermal conductivity was estimated by Wiedemann-Franz law $\kappa_{el} = L\sigma T$ where L, σ and T are Lorentz number, electrical conductivity and temperature respectively. Lorenz number value for degenerate limit (2.44×10^{-8} $W\Omega K^{-2}$) was used in estimation. Major contribution towards total thermal conductivity comes from lattice vibration as seen in Figure. 3.12 (b) and (c).

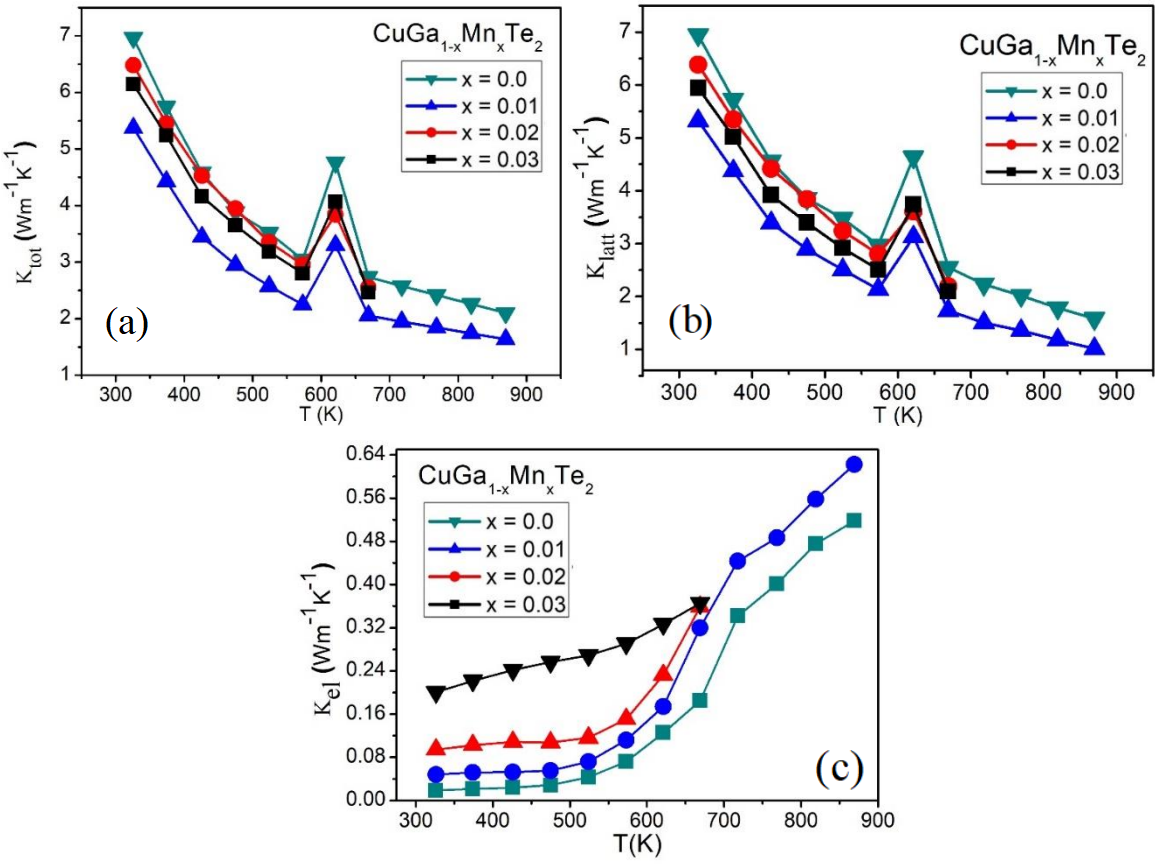

Figure 3. 12 (a) Total thermal conductivity as a function of temperature for the $CuGa_{1-x}Mn_xTe_2$, x = 0.0, 0.01, 0.02, 0.03. (b). Plots of Lattice thermal conductivity (c) Plots of electronic contribution towards total thermal conductivity [21].

In all synthesized samples a peak in thermal conductivity was observed around 630 K. This peak was originated in heat capacity and Differential Scanning Calorimetry (DSC). All chalcopyrite samples showed this cusp in DSC at similar temperature. To check for any phase transition we performed high temperature XRD for $CuInTe_2$ sample. As for the case of $CuGaTe_2$, atomic numbers of Cu and Ga are very close thereby it is quite difficult to distinguish ordered and disordered state in $CuGaTe_2$ through XRD. Results can be seen in Appendix Figure A. No phase transition is observed up to 773 K.

Finally we calculated Figure of merit (*ZT*) for $CuGa_{1-x}Mn_xTe_2$ where x = 0.0-0.03. Temperature dependent *ZT* values are shown in Figure 3.13. Maximum value of 0.83 was calculated for 1 % Mn doped sample at 870 K. This corresponds to 40% enhancement in *ZT* value with that of pristine sample. This improvement in *ZT* value is attributed to enhancement in power factor due to increase in effective mass and lower thermal conductivity simultaneously. Overall magnetic ion doping proved to be an effective strategy to improve thermoelectric properties of $CuGaTe_2$.

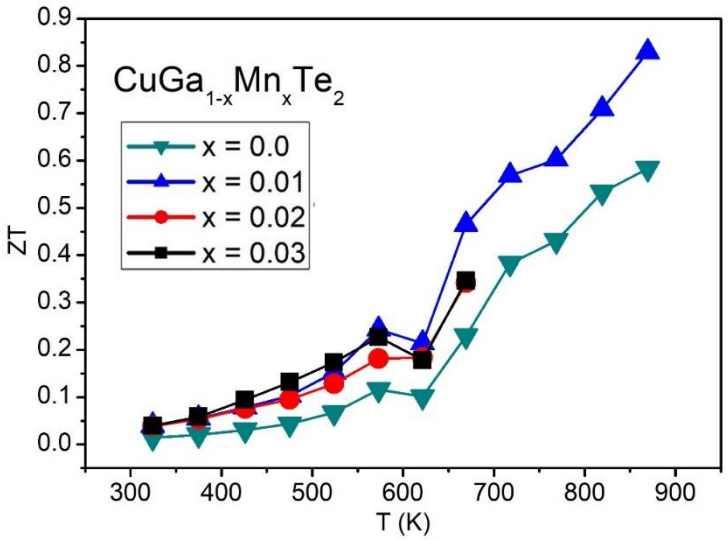

Figure 3. 13 Thermoelectric Figure of merit (*ZT*) as a function of temperature for the $CuGa_{1-x}Mn_xTe_2$, x = 0.0, 0.01, 0.02, 0.03 [21].

9. Summary

Polycrystalline samples with composition $CuGa_{1-x}Mn_xTe_2$ where x = 0.0-0.03 were successfully synthesized by solid state reaction method. Following are important highlights of research.

1. Electrical conductivity was greatly enhanced while Seebeck coefficient retains large values. i.e., Seebeck coefficient value of 280 mVK^{-1} observed at T = 670 K for pristine $CuGaTe_2$, while, for $CuGa_{0.97}Mn_{0.03}Te_2$ is almost as large as 230 mVK^{-1}. However, at the same temperature electrical conductivity remarkably increased to around twice the values when the Mn doping concentration was increased from x = 0 to 0.03.

2. Power factor was improved greatly as a result of improved carrier concentration and effective mass simultaneously. Effective mass was improved by magnetic moment of Mn and charge carrier interactions.

3. To differentiate the carrier tuning effect from magnetic enhancement Seebeck coefficients were plotted as a function of $\ln\sigma$. Based on theoretical model Seebeck vs $\ln\sigma$ plot revealed enhancement in effective mass term $T^{3/2}(m^*/m_0)^{3/2}\mu$. We also evaluated power factor from the linear relationship of S and $\ln\sigma$; $S = m(b - \ln\sigma)$. The plot between power factor and σ revealed that power factor values for Mn incorporated samples are higher than maximum values expected after carrier tuning effect.

4. Reciprocal of magnetic susceptibility due to Mn ions as a function of temperature revealed large negative Weiss temperature values θ = -59.1 K for $CuGa_{0.99}Mn_{0.01}Te_2$. Negative values indicates antiferromagnetic interactions on Mn spins. Large Weiss temperature value for dilute system was discussed to be more likely due to onsite exchange interaction between Mn spins and conduction and/or valence band electrons.

5. Evidence of strong coupling between Mn magnetic moments and carrier holes was also seen from Anomalous Hall effect (AHE). Contribution from AHE term (10^{-4} Ω cm) was comparable to ferromagnetic $Ga_{1-x}Mn_xAs$ and $Fe_{1-x}Co_xSi$ was observed.

In conclusion we demonstrated that magnetic elements like Mn doping into semiconductors can be an effective strategy to improve power factor and thereby Figure of merit (ZT).

Chapter 4: Thermoelectric and Magnetic Properties of Mn Doped $CuInTe_2$

1. Introduction

In the previous chapter we discussed synthesis and thermoelectric properties of $CuGa_{1-x}Mn_xTe_2$ where x = 0.0-0.03. We demonstrated that enhancement in the power factor by magnetic ion doping is an effective strategy for chalcopyrite type compounds. To elucidate this mechanism of magnetic enhancement further we selected another member of chalcopyrite family $CuInTe_2$. In this study, we report the Mn-doping effect to $CuInTe_2$. It was demonstrated that the interaction of magnetic moment with charge carriers can be helpful in enhancing power factor in $CuFeS_2$ and in $CuGa_{1-x}Mn_xTe_2$.[20] In the former compound, first-principles calculation studies have revealed that the antiferromagnetic state in $CuFeS_2$ is essential for the high power factor. [153], [165] For the latter compound, power factor enhancement beyond the carrier-optimized value was achieved, and was explained by the interaction between Mn^{2+} magnetic moment and carriers, as observed by the magnetization and anomalous Hall-effect measurements. Recently, Mn-doping effect has been argued in $Mg_{1-x}Mn_xSi$ [166]. Other magnetic semiconductors have also been found with good thermoelectric properties. [167], [168]

$CuInTe_2$ belongs to chalcopyrite family and attracted much attention for its favorable thermoelectric properties [15], [19], [169]–[171]. Many theoretical and experimental studies confirms $CuInTe_2$ based compounds can be promising for thermoelectric applications. For example, ZT value of as high as 1.72 was predicted by calculations based on density functional theory. This study also discuss Cu and In site as potential doping site to tune its thermoelectric properties [172]. Enhanced carrier concentration was achieved by Cd doping and as a result power factor was improved. At the same time Cd incorporation decreased thermal conductivity. Thereby about 100% improvement was observed at room temperature reported by Cheng et.al [171]. Kucek et.al reported Ni doping at Cu site improved 50 % ZT value in mid temperature range [173].

We synthesized polycrystalline samples of $CuIn_{1-x}Mn_xTe_2$ with x = 0.0, 0.01, 0.02. Electrical resistivity decreased slightly while maintaining high Seebeck values, which led to improved power factor. Thermal conductivity showed noticeable decrease by Mn-doping. As a consequence, maximum ZT value of 0.82 was observed at 854 K for x = 0.02 sample. Magnetic properties are measured and are discussed in relation to thermoelectric properties. Inverse of magnetic susceptibility with temperature is fit with a Curie Weiss function. The results show that the Mn

ions doped in $CuInTe_2$ are in the Mn^{3+} state. From the Curie-Weiss fitting, a strong antiferromagnetic interaction between Mn and carriers was inferred, which suggests the magnetic interaction is a probable origin for the enhanced power factor. Temperature dependences of electrical resistivity and Seebeck coefficient change their character at 450 K from degenerate semiconductor behavior to intrinsic semiconductor one, and the power factor enhancement rapidly diminishes above 450 K. This suggests that electronic correlation inside Mn-related impurity band plays an important role for the enhanced power factor at the low-temperature side.

2. Experimental Section

Experimental process is same as we used for $CuGa_{1-x}Mn_xTe_2$. See the details in chapter 1, Section 2

3. Results

3.1 Structural Analysis

Powder XRD patterns for $CuIn_{1-x}Mn_xTe_2$, where x = 0.0, 0.01, 0.02 are presented in Figure 4.1. All synthesized samples were found to be phase pure and exhibit tetragonal crystal structure with space group *I -4 2 d*. No secondary phase peaks were detected in XRD patterns [174]. All the peaks observed were matched with that of chalcopyrite structure. Bar symbols at the bottom of the graphs are showing 2θ positions from the ICSD Reference card (PDF # 01-081-1937). In order to obtain lattice parameters Rietveld refinement was performed using FullProf software. Rietveld refinement results are plotted in Figure 4.2. Obtained lattice parameters were plotted as a function of Mn doping concentration as shown in Figure 4.2. Lattice parameters were scarcely changed attributed to minute Mn doping concentration. Values of lattice parameters were in good agreement with previous reports, $Cu_{1-x-\delta}Ag_xInTe_2$ [175] and $Cu_{1-x}InTe_2$ [176].

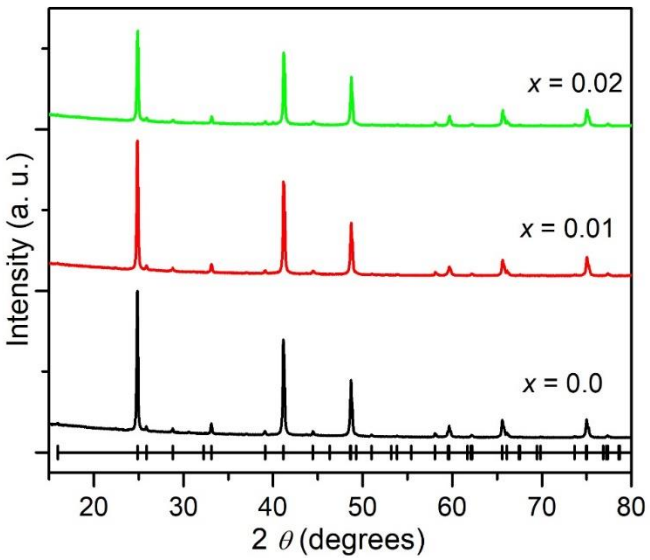

Figure 4. 1 XRD patterns of $CuIn_{1-x}Mn_xTe_2$ with x = 0.0, 0.01, 0.02. All peaks observed in X-ray patterns were matched with those of the chalcopyrite structure. ICSD Reference card (PDF # 01-081-1937) 2θ positions are shown in the bottom of the graph with bar symbol

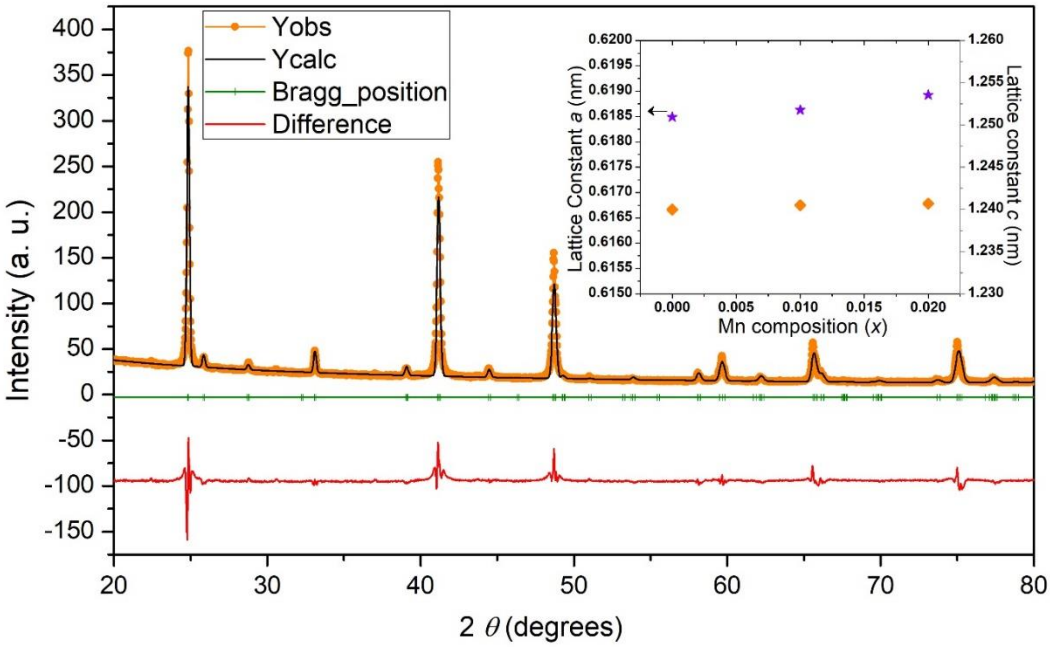

Figure 4. 2 Rietveld refinement result for the powder X-ray diffraction pattern of $CuInTe_2$. Inset shows dependence of lattice constants (a on left axis, c on right axis) with respect to Mn composition

4. Magnetic Properties

Magnetic Properties for $CuIn_{1-x}Mn_xTe_2$ (x = 0.0, 0.01, 0.02) were carried out to investigate the effect of magnetic ion substitution. Field dependence of magnetization for all synthesized samples are presented in Figure 4.3 (a) and (b). As expected, non-doped sample ($CuInTe_2$) shows diamagnetic behavior. However, for Mn substituted paramagnetic behavior was observed at 5 K and 300 K. Magnitude of magnetization increased with increased Mn doping concentration. Inverse of magnetic susceptibility (χ_{Mn}) as a function of temperature plots are shown in Figure 4.3. (χ_{Mn}) was determined by subtracting the magnetic susceptibility of pristine $CuInTe_2$ from Mn doped samples. Here, (χ_{Mn}) represents the Mn contribution towards total susceptibility(χ_{tot}). Graph demonstrates linear behavior between $1/(\chi_{Mn})$ and temperature. This suggests that around room temperature magnetic susceptibility is governed by Curie Weiss function.

$$\chi = \chi_o + \frac{C}{T - \theta}$$

In above equation, C is Curie constant, θ is Weiss temperature and χ_o is temperature-independent susceptibility. We subtracted any effects other than from Mn and now only dealing

with (χ_{Mn}). Linear relationship is demonstrated in Figure 4.4 by black solid lines. Here, the Curie constant is expressed as follows

$$C = \frac{N\mu_{eff}^2}{3k_B}$$

Where N is the number of magnetic moments and k_B the Boltzmann constant, and μ_{eff} is the effective magnetic moment. Here, μ_{eff} is

$$\mu_{eff} = 2\sqrt{S(S+1)}\mu_B$$

In the Table values of Weiss temperature, effective magnetic moment and Curie constants are summarized. Effective magnetic moment μ_{eff} calculated values are roughly close to 4.89 μ_B which is expected value for Mn^{3+} valence state. Also these values are much smaller than 5.92 μ_B, which is expected value for Mn^{2+} valence state. Therefore, in $CuIn_{1-x}Mn_xTe_2$ Mn ions are most likely exhibit trivalent state. This is in contrast to the case of $CuGa_{1-x}Mn_xTe_2$ [20] and $CuIn_{1-x}Mn_xS_2$ [177], where Mn^{2+} states were suggested for both the compounds. As shown in Table 4.4 Weiss temperature exhibit negative values. This indicates antiferromagnetic interactions on Mn spins as discussed in detail in Chapter 1. This large negative Weiss temperature can be best explained by Kondo-type interaction i.e., on-site interaction between charge carriers and magnetic moments. It is possible these interactions contribute in maintaining high Seebeck values or even results in enhanced values by increasing carrier effective mass.

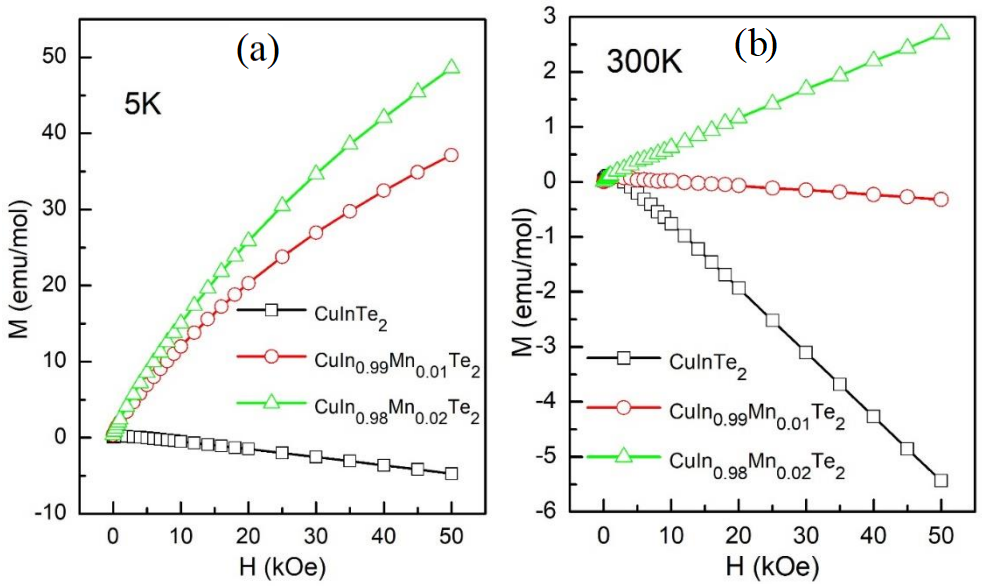

Figure 4. 3 Temperature dependence of magnetic properties for $CuIn_{1-x}Mn_xTe_2$ with x = 0.0-0.02. (a) Magnetic field dependence of magnetization M measured at 5 K (b) Magnetic field dependence of magnetization M measured at 300 K

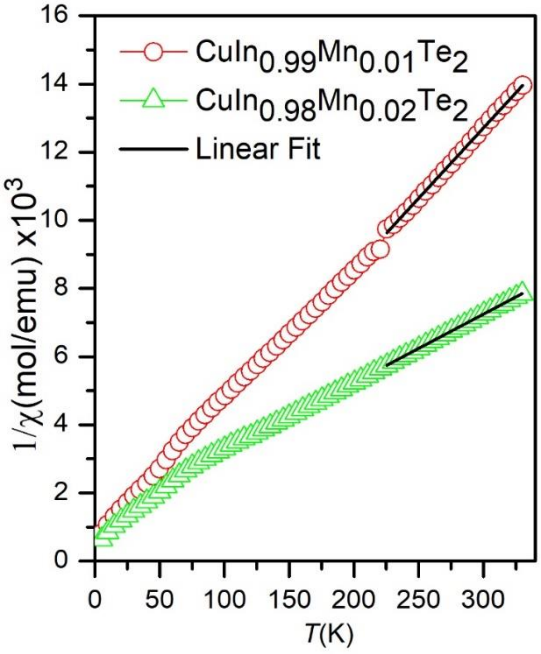

Figure 4. 4 Inverse of magnetic susceptibility verses temperature. Contribution from pristine $CuInTe_2$ has been subtracted from measured susceptibility. Black solid lines shows fit with linear function

Table 3 Values of Curie constant, Weiss temperature and Effective magnetic moment (μ_{eff}).

Sample composition	**$CuIn_{0.99}Mn_{0.01}Te_2$**	**$CuIn_{0.98}Mn_{0.02}Te_2$**
θ **(K)**	-19.02	-47.80
C **(emu K/mole)**	0.024	0.049
μ_{eff} (μ_B)	4.40	4.46

5. Thermoelectric properties

Plots of electrical resistivity as function of temperature for $CuIn_{1-x}Mn_xTe_2$ where x = 0.0, 0.01, 0.02 are presented in Figure 4.5 (a). Electrical resistivity shows an increasing behavior below 450 K making a small peak followed by the decrease in resistivity with further increase in temperature. Initial increase in electrical resistivity is a typical behavior for degenerate semiconductors for which electrical transport is governed by charge carriers produced from defects and impurities.

Above 500 K, decrease in resistivity as a function of temperature suggest intrinsic

semiconducting behavior. In this region electrical transport is dominated by thermally activated charge carriers. Electrical resistivity showed decrease in the temperature region 323 – 500 K for Mn substituted samples. This is most probably due to an increase in the charge carriers concentration. This change in carrier concentration is small which is contrary to our previous research work of Mn doped $CuGaTe_2$ [20]. Where we observed large increase in hole carriers with Mn doping concentration. As seen in Chapter 1 magnetic properties confirmed Mn^{2+} valence state. Hence, reduction in electrical resistivity for Mn substituted samples was naturally expected. In another report of $CuIn_{1-x}Mn_xS_2$ [177] electrical resistivity also show reduction due to Mn doping. However, in the present case of $CuIn_{1-x}Mn_xTe_2$ resistivity change showed small decrease. This is in agreement with the Mn^{3+} valence state observed in the magnetic properties. In this case, carrier concentration is not sensitive to Mn concentration. For higher temperature T > 550 K resistivity difference between doped and pristine samples is diminished because thermally excited charge carriers overcome doping effect.

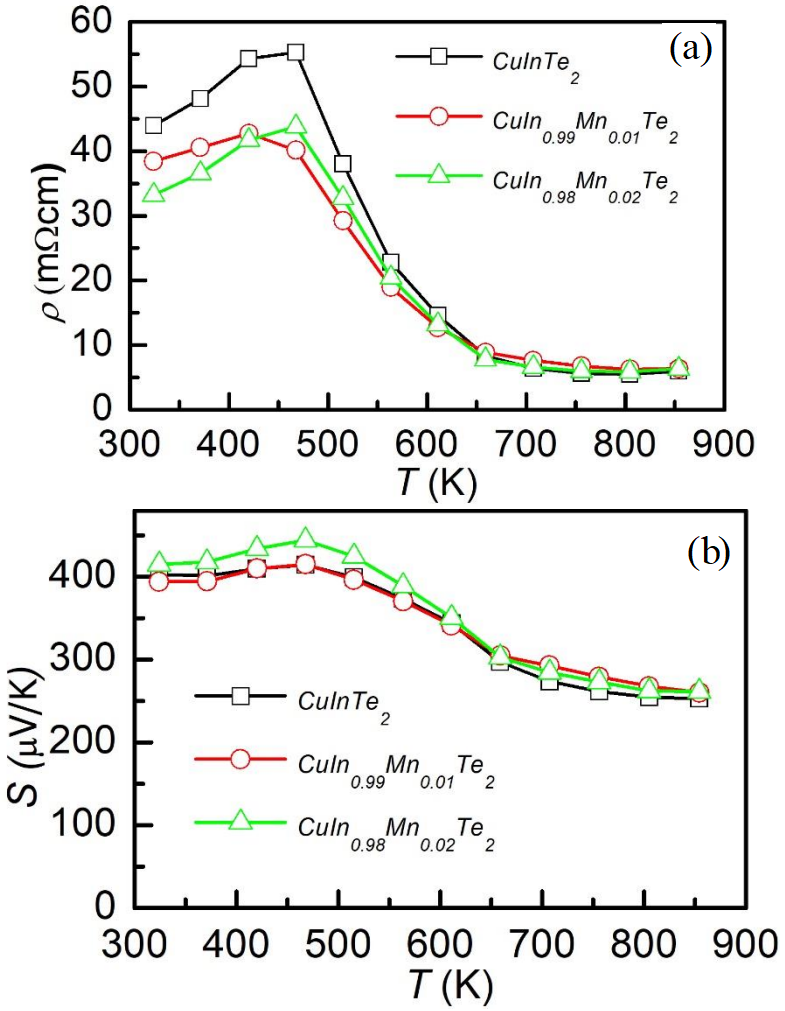

Figure 4. 5 Temperature dependence of electrical properties. (a) Electrical resistivity, (b) Seebeck coefficient, for $CuIn_{1-x}Mn_xTe_2$

Figure 4.5 (b) shows plots of Seebeck coefficient for $CuIn_{1-x}Mn_xTe_2$ where $x = 0.0, 0.01, 0.02$. All synthesized samples showed positive Seebeck coefficient values. This indicates to holes as majority charge carriers. Seebeck coefficient showed decrease with increase in temperature for all samples. This behavior is attributed to thermally activated excess charge carriers at higher temperature and is consistent with resistivity response. Hence, it is expected that increase in the carrier concentration causes decrease in the electrical resistivity while Seebeck coefficient also drops. At lower temperature region this is in agreement with resistivity behavior. Interestingly, Seebeck coefficients for Mn doped samples did not show any decrease as compared to value of pristine sample. Furthermore, slightly higher Seebeck values were observed for $CuIn_{0.98}Mn_{0.02}Te_2$. These results suggests increase in $m^*3/2\mu$ term for Mn substituted samples. Where μ represents carrier mobility [149]. Since μ is expected to be reduced by Mn-doping because of the concomitant disorder, this indicates that the increase in the effective mass m^* is significant. Here, we propose charge carriers and magnetic moment correlation is the reason which stop the drop of Seebeck coefficient values. As a result of which power factor S^2/ρ values are improved. Power factor for all samples as a function of temperature are presented in Figure 4.6.

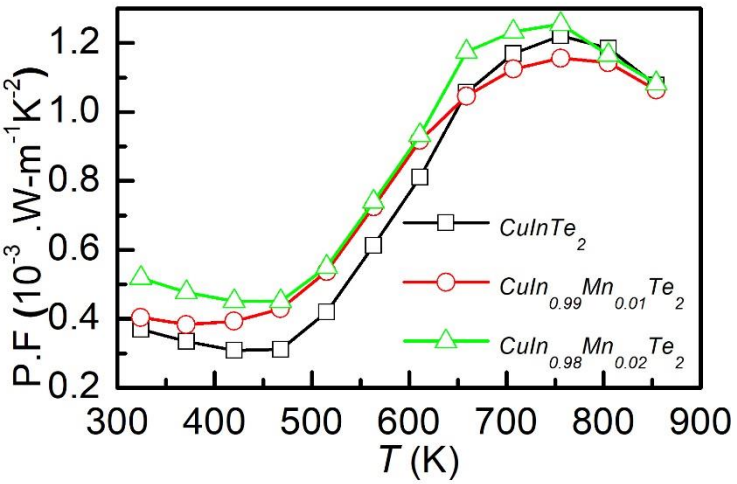

Figure 4. 6 Power factor as a function of temperature for $CuIn_{1-x}Mn_xTe_2$ where $x = 0.0, 0.01, 0.02$

For sample composition $CuIn_{0.98}Mn_{0.02}Te_2$ power factor value at 323 K is 0.52 mW-m^{-1}K^{-2} which is almost 50% enhancement to the power factor value of 0.36 mW-m^{-1}K^{-2} observed for pristine sample ($CuInTe_2$) at same temperature. As seen in plots power factor enhancement with respect to non-doped $CuInTe_2$ is greater at lower temperatures while this enhancement becomes smaller at higher temperature, and especially, above 700 K, there is little enhancement. We observed change in the temperature dependence for resistivity and Seebeck coefficient around 450 K, this behavior if analyzed can give some hints to the detailed conduction mechanism as shown later

To investigate further Seebeck coefficient is plotted as a function of lnσ. Results are presented in Figure 4.7. Seebeck coefficient as a function of lnσ plot were suggested by Min and Rowe as a better thermoelectric performance indicator [149]. Seebeck coefficient based on theoretical model can be written in the form; $S = m(b - \ln\sigma)$, where b is the parameter which involves the term $T^{3/2}(m^*/m_0)^{3/2}\mu$, and $m = k_B/e = 86.14\mu V/K$. Figure 4.7 shows plots of Seebeck coefficient as a function of lnσ at different temperature (324, 370, 420, and 463 K). In the Figure 4.7 broken lines have the slope -86.14 µV/K. Slope is negative because of holes as majority carriers. Data for Mn substituted samples lies above the line that passes through the data of pristine sample $CuInTe_2$. This graph demonstrates improvement in b value ($\sim T^{3/2}(m^*/m_0)^{3/2}\mu$) with Mn doping. However, the enhancement is smaller for 1% doped sample only at 420 and 463 K.

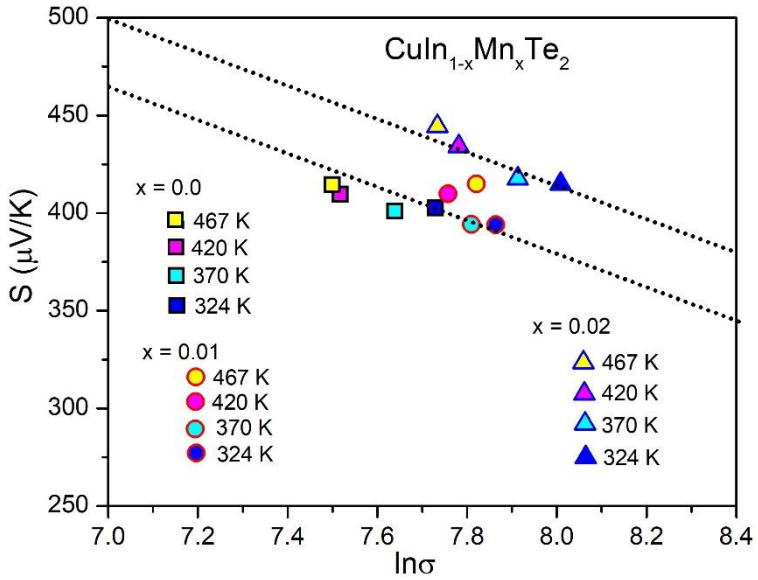

Figure 4. 7 Plots of Seebeck coefficient at temperature 324, 370, 420, and 463 K as a function of lnσ. Black dotted lines have the slope of -86.14 µV/K. For $x = 0.02$ sample, data (shown with triangles) lie above the slope line of non-doped sample (shown with squares), indicating improvement in the effective mass term with Mn doping.

To analyze conduction mechanism relative power factors values of $CuIn_{1-x}Mn_xTe_2$ with respect to that of $x = 0$ as functions of temperature were plotted. Results are presented in Figure 4.8. Two regions were distinguished from the graph. Below and above 450 K Power factor values tends to increase in extrinsic region and drops after 450 K in intrinsic region. This behavior is consistent to that observed in electrical properties. Below 450 K, (degenerate semiconductor region) Carriers are mainly condensed in the impurity related band, therefore strong interaction is expected for Mn d-levels and carriers. On the other hand, at elevated temperatures inter-band excitation of carriers dominates thereby the coupling between charge carriers and

magnetic moment of Mn becomes smaller. As pointed out in magnetic properties that Mn ions exists in trivalent state and so does the In ions thereby coupling with hole carrier and Mn ions may not be strong. Which leads to weaker interactions at elevated temperature. Contrary to study of $CuGa_{1-x}Mn_xTe_2$ in which carriers were doped as a result of Mn^{2+} and Ga^{3+} substitution. Thereby, in $CuGa_{1-x}Mn_xTe_2$ system, holes and Mn ions tend to couple more strongly than in the present case of $CuIn_{1-x}Mn_xTe_2$. Nevertheless, it should still be emphasized that even for the case of isoelectronic substitution, power factor enhancement is significant up to about 500 K.

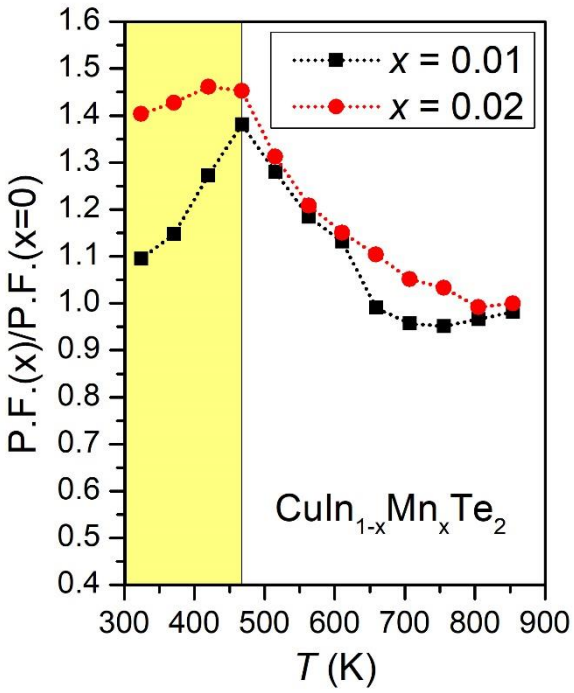

Figure 4. 8 Relative power factors of $CuIn_{1-x}Mn_xTe_2$ with respect to that of $x = 0$ as functions of temperature. Yellow regions (T < 450K) corresponds to the degenerate semiconductor region, and white (> 450K) indicates the intrinsic semiconductor region. In degenerate semiconductor region below 450 K relative power factor values increases and then started decreasing in intrinsic region.

Plots of thermal conductivity as a function of temperature are presented in Figure 4.9. For all nominal samples thermal conductivity value decreased with increase in temperature. This is attributed to dominant Umklapp scattering of phonons at higher temperature. Upon Mn substitution reduction in thermal conductivity is observed. Estimated reduction of 15 to 20 % in thermal conductivity is observed as compared with that of pristine $CuInTe_2$. For example, for sample composition $CuIn_{0.98}Mn_{0.02}Te_2$, value of thermal conductivity at 324 K is 4.8 $Wm^{-1}K^{-1}$ whereas, for $CuInTe_2$ value is 5.9 $Wm^{-1}K^{-1}$ at same temperature, which is 20 % reduction. This decrease in thermal conductivity can be attributed to the difference in mass and ionic radii of substituted elements. Klemen's and Callaway model suggests that mass difference can cause increased scattering parameter which leads to lower thermal conductivity [178], [179]. To

account for electronic and lattice part of thermal conductivity we estimated electronic thermal conductivity by using Wiedemann Franz Law $k_e = LT\sigma$ [42], where L, and k_e, symbolizes Lorenz number and electronic thermal conductivity respectively. Here, Lorenz number value for the degenerate limit, $L = 2.4\text{x}10^{-8}$ $W\Omega K^{-2}$ is assumed. Results are plotted in Figure 4.9 (b). Figure 4.9 (b) confirms that contribution from carriers are minimal and major contribution towards total thermal conductivity is from lattice thermal conductivity.

By combining all the properties we obtained Figure of merit value. Results are plotted in Figure 4.9 (c) as a function of temperature. For $CuIn_{0.98}Mn_{0.02}Te_2$, highest ZT value calculated is 0.82 at 854 K for $CuIn_{0.98}Mn_{0.02}$ which corresponds to around 30 % enhancement from that of the non-doped $CuInTe_2$. This improvement in ZT value was achieved by reducing thermal conductivity and enhanced power factor simultaneously. ZT can be further improved by reducing thermal conductivity utilizing other methods i.e. nano structuring [8] and/or incorporating micrometer sized secondary phases [21]

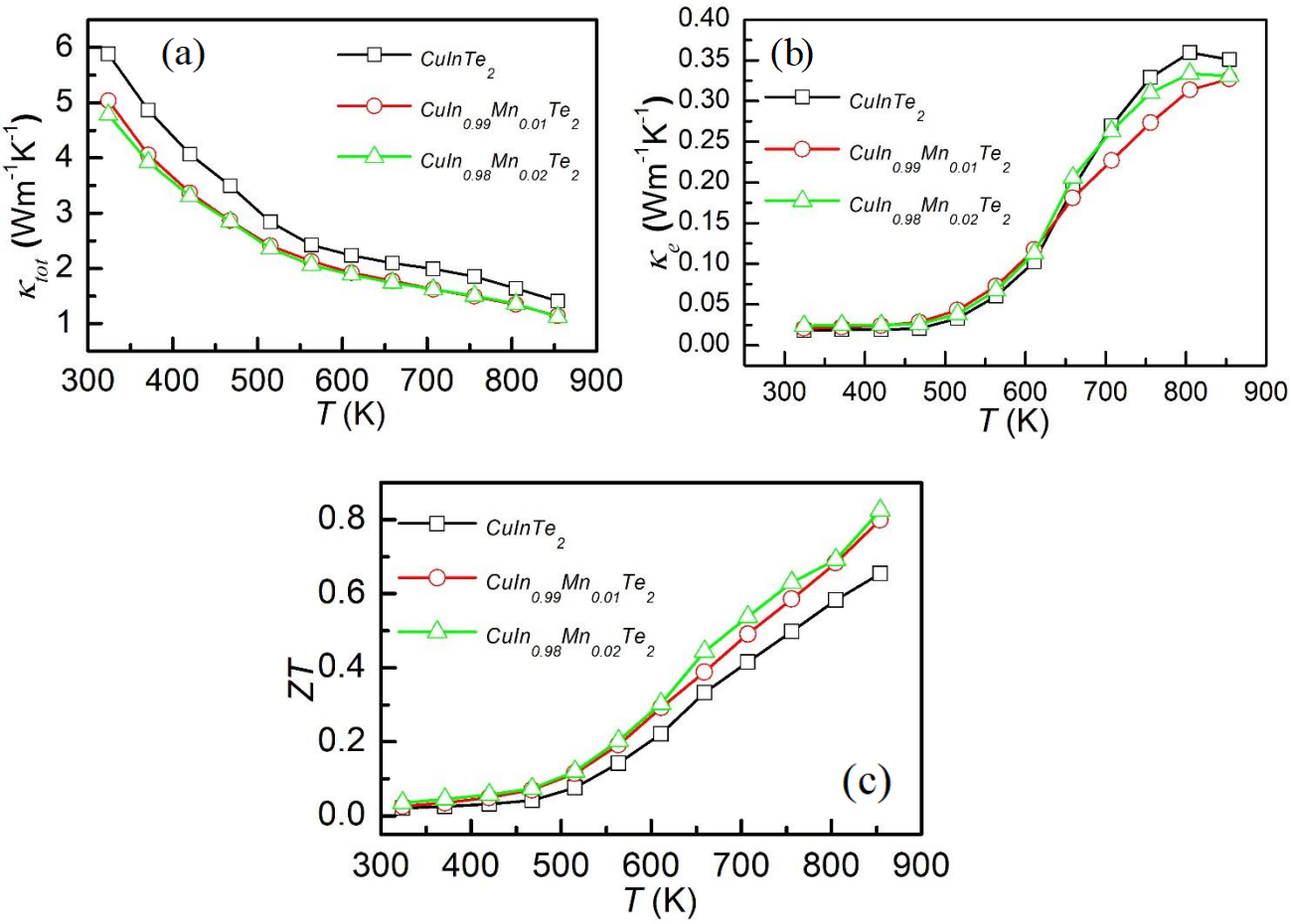

Figure 4. 9 Temperature dependence of thermal transport properties. (a) Total thermal conductivity, (b) electronic thermal conductivity, (c) Figure of merit (ZT) for $CuIn_{1-x}Mn_xTe_2$.

6. Summary

In this research we studied influence of Mn substitution with In in $CuInTe_2$. Polycrystalline samples of $CuIn_{1-x}Mn_xTe_2$ where x = 0.0, 0.01, 0.02 were synthesized and characterized for thermoelectric and magnetic properties.

- Seebeck coefficients did not show any decrease after Mn substitution and even slightly higher Seebeck values were observed for $CuIn_{0.98}Mn_{0.02}Te_2$. As proposed in the previous section magnetic moment charge carrier interaction could be the possible reason in the enhancement of Seebeck coefficient via increased effective mass.

- To clarify Seebeck coefficient as a function of $\ln\sigma$ were plotted. Graph revealed Seebeck values for Mn doped samples reside above the line that passes through Seebeck coefficients of pristine sample. This indicates enhancement in effective mass term after Mn doping.

- Power factor calculated at 323 K for non-doped $CuInTe_2$ is 0.36 $mW\text{-}m^{-1}K^{-2}$, while a higher value of 0.52 $mW\text{-}m^{-1}K^{-2}$ is observed for $CuIn_{0.98}Mn_{0.02}Te_2$ at the same temperature. This is close to 50% improvement.

- Conduction mechanism change was observed after 450 K. Two regions were distinguished. Major improvement in the power factor was seen in extrinsic region while at higher temperatures carrier and magnetic moment coupling become weaker. Hence, the difference in the power factor to that of non-doped sample becomes smaller. This suggests that electronic correlation inside Mn-related impurity band plays an important role for the enhanced power factor at low-temperature side.

- Magnetic susceptibility verses temperature showed paramagnetic behavior with large negative Weiss temperature, which suggested antiferromagnetic interactions on Mn spins are dominant. Fitting to the magnetic susceptibility data indicated that the doped Mn ions are most likely in the trivalent state.

Overall thermoelectric properties were improved. These results also reinforces previous research results for Mn doped $CuGaTe_2$. Results presented in this chapter are submitted to journal of electronic materials and are under revision [174].

Chapter 5: Secondary Phase Assisted Enhancement in TE Properties of Fe doped $CuGaTe_2$

1. Introduction

Since the discovery of thermoelectric phenomenon many techniques were introduced to resolve the existing conflicts inside the thermoelectric materials. Some of them were discussed in chapter 1. In the third and fourth chapter we discussed influence of magnetic ions as an effective strategy towards improvement of power factor on chalcopyrite type compounds. In this chapter we will present results of microstructure analysis and secondary phase assisted improved thermoelectric properties of $CuGaTe_2$ by Fe doping. Solubility limit of Fe was discussed through morphological analysis. Solubility limit inside $CuGaTe_2$ was found to be very less. Therefore, secondary phases were generated. Impact of secondary phases on thermoelectric properties was also analyzed through microstructure analysis. Secondary phases plays a crucial role on altering thermoelectric properties. Pure phase compounds are always considered for good properties. However, impurity phases can also be helpful if controlled through careful synthesis and microstructural analysis.

In this Chapter we report results of Fe substitution and its effects on thermal transport and structural properties in chalcopyrite-type $CuGaTe_2$ [21]. Polycrystalline samples with the composition $CuGa_{1-x}Fe_xTe_2$ where $x = 0.0$ to 0.05 were synthesized by melt and anneal method followed by Spark plasma sintering. Structural and morphological analysis were done using powder XRD and Electron probe micro analysis (EPMA). Which indicates poor solubility of Fe inside $CuGaTe_2$ and presence of secondary phases. E.g. CuTe and $FeTe_2$. However we observed large reduction in thermal conductivity especially for 2 % Fe doped sample. However, further addition of Fe results in greater thermal conductivity. Power factor has been improved with Fe addition as well. Thereby, Figure of merit (ZT) was enhanced and maximum value of 0.92 is obtained at 770 K for composition $CuGa_{0.98}Fe_{0.02}Te_2$. This is around 60% improvement as compared to pristine $CuGaTe_2$. In this work role of secondary phases and microstructural analysis towards improvement in thermoelectric properties of chalcopyrite $CuGaTe_2$ is demonstrated.

2. Method and Materials

Polycrystalline samples having composition $CuGa_{1-x}Fe_xTe_2$ where x = 0.0 to 0.05 were synthesized by melt and anneal method followed by Spark plasma sintering. Specimens with high purity were used for synthesis Fe (99.99%), Cu (99.99%), Te (99.9999%), Ga (99.9999%). Details of synthesis process can be seen in Chapter 2. For microstructure analysis we used electron probe micro analysis (EPMA) using JEOL JXA-8900F. Wavelength dispersive spectroscopy (WDS) was used to check the chemical composition of the samples. Cu, Fe, Te, and GaP were used as standard materials for chemical composition analysis. For other techniques details see Chapter 4.

3. Structural Analysis

X-ray diffraction patterns for all the synthesized samples are presented in Figure 5.1. All the peaks were indexed with that of tetragonal structure (space group *I-4 2 d*). Small peaks of secondary phases like Fe and $FeTe_2$ were observed for the composition $CuGa_{0.96}Fe_{0.04}Te_2$ and $CuGa_{0.95}Fe_{0.05}Te_2$ as seen in Figure 5.2 (a). Lattice parameters were refined by Rietveld Refinement Technique. Lattice parameters obtained were consistent with previously reported results [180], [181]. Figure 5.2 (b) shows plot of lattice parameters values as a function of Fe concentration. As expected, Lattice parameters did not showed any significant change because of similar ionic sizes for Fe^{3+} and Ga^{3+}. Refined lattice parameters values along with relative densities are summarized in Table 4.

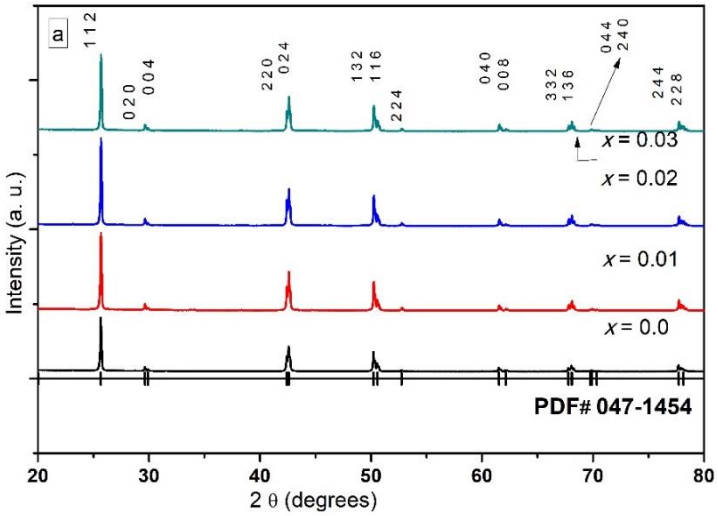

Figure 5. 1 Powder XRD patterns of polycrystalline samples of $CuGa_{1-x}Fe_xTe_2$ (x = 0, 0.01, 0.02, 0.03). At the bottom of the XRD patterns standard reference card data is shown.

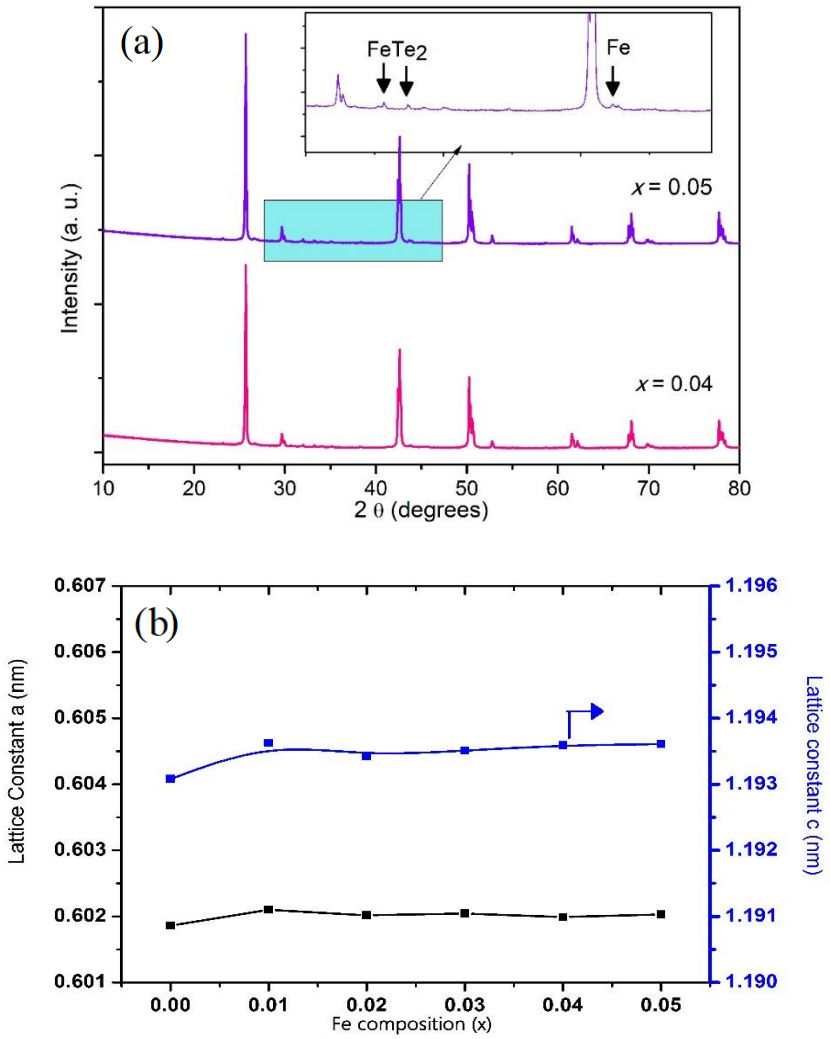

Figure 5. 2 (a) Powder XRD patterns of polycrystalline samples of $CuGa_{1-x}Fe_xTe_2$ (x = 0.04, 0.05). Clearly showing secondary phase peaks in the inset. (b) Plot of Lattice constants with respect to Fe composition.

4. Microstructure and compositional analysis

XRD patterns clearly indicated minority phases inside Fe doped $CuGaTe_2$ system. This was an indication for poor solubility of Fe. To investigate this point further Electron probe micro analysis (EPMA) was used to analyze all nominal compositions for elemental compositions. SEM Images obtained in EPMA are shown in Figure 5.3. Arrows inside images refers to the points analyzed.

Figure 5.4-5.6 shows Cu, Fe, Ga and Te elemental maps for all samples. It was observed in Figure 5.3 that small amount of oxygen is dispersed over grain boundaries. Main phase chemical

composition was homogeneous. In Table 4 we summarized analyzed and nominal compositions. Results clearly shows poor solubility (< 1%) of Fe at Ga site whereas main phase composition for all nominal samples is close to $Cu_{1.00}Ga_{1.00}Te_{2.00}$. Small amount of Fe seems to be substituted in $CuGaTe_2$ phase (only about 0.02 atomic % for composition $CuGa_{0.99}Fe_{0.01}Te_2$). Secondly, EPMA analysis confirms presence of secondary phases like CuTe and $FeTe_2$. Initially, up to the 2 % of Fe substitution secondary phase $FeTe_2$ have small size of few micrometer as seen in Figure 5.5 which shows Fe-rich phase is dispersed over grain boundaries. However, when Fe doping concentration is increased (for $x \geq 0.03$) we observed increase in the grain size of Fe-rich secondary phase. E.g. for 5% Fe doped sample it size grows to the order of 10 μm almost similar to the grain size of $CuGaTe_2$ phase. These results are also consistent with results of XRD patterns. Where secondary phase appears for higher doped samples. For low doped samples peaks were not seen because of low grain sizes. In the next section we explained the effect of these secondary phases on thermoelectric properties.

Table 4 shows nominal and analyzed composition along with lattice parameters and relative density

S. no	Nominal composition	Analysed composition	Relative Density	Lattice constant (nm) a	c
1	$CuGaTe_2$	$Cu_{0.964}Ga_{1.024}Te_{2.012}$	99%	0.60186(50)	1.19308(10)
2	$CuGa_{0.99}Fe_{0.01}Te_2$	$Cu_{0.992}Ga_{1.010}Fe_{0.001}Te_{1.998}$	97.6%	0.60210(20)	1.19362(41)
3	$CuGa_{0.98}Fe_{0.02}Te_2$	$Cu_{0.991}Ga_{1.010}Fe_{0.001}Te_{1.998}$	98.3%	0.60201(07)	1.19343(20)
4	$CuGa_{0.97}Fe_{0.03}Te_2$	$Cu_{0.992}Ga_{1.004}Fe_{0.002}Te_2$	99.1%	0.60204(06)	1.19351(17)
5	$CuGa_{0.96}Fe_{0.04}Te_2$	$Cu_{1.00}Ga_{1.012}Fe_{0.002}Te_{1.984}$	96.1%	0.60199(08)	1.19359(28)
6	$CuGa_{0.95}Fe_{0.05}Te_2$	$Cu_{0.996}Ga_{1.004}Fe_{0.003}Te_{1.996}$	95.0%	0.60203(04)	1.19360(15)

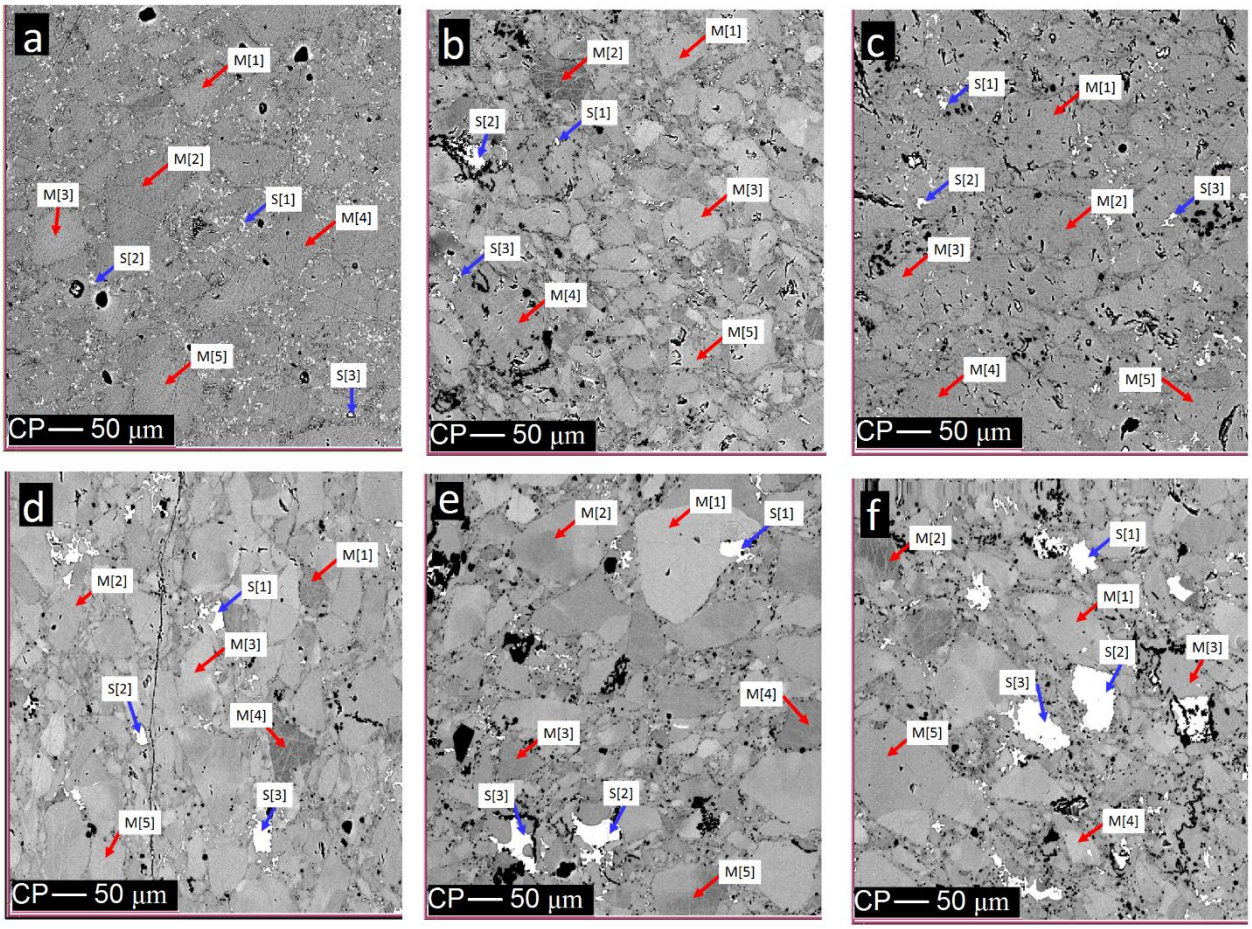

Figure 5. 3 BSE images captured in EPMA for (a) $CuGaTe_2$ (b) $CuGa_{0.99}Fe_{0.01}Te_2$ (c) $CuGa_{0.98}Fe_{0.02}Te_2$, (d) $CuGa_{0.97}Fe_{0.03}Te_2$, (e) $CuGa_{0.96}Fe_{0.04}Te_2$, (f) $CuGa_{0.95}Fe_{0.05}Te_2$. M[1,2,3,4,5,] are the points mentioning the main phase and S[1,2,3] are the points referring to secondary phases.

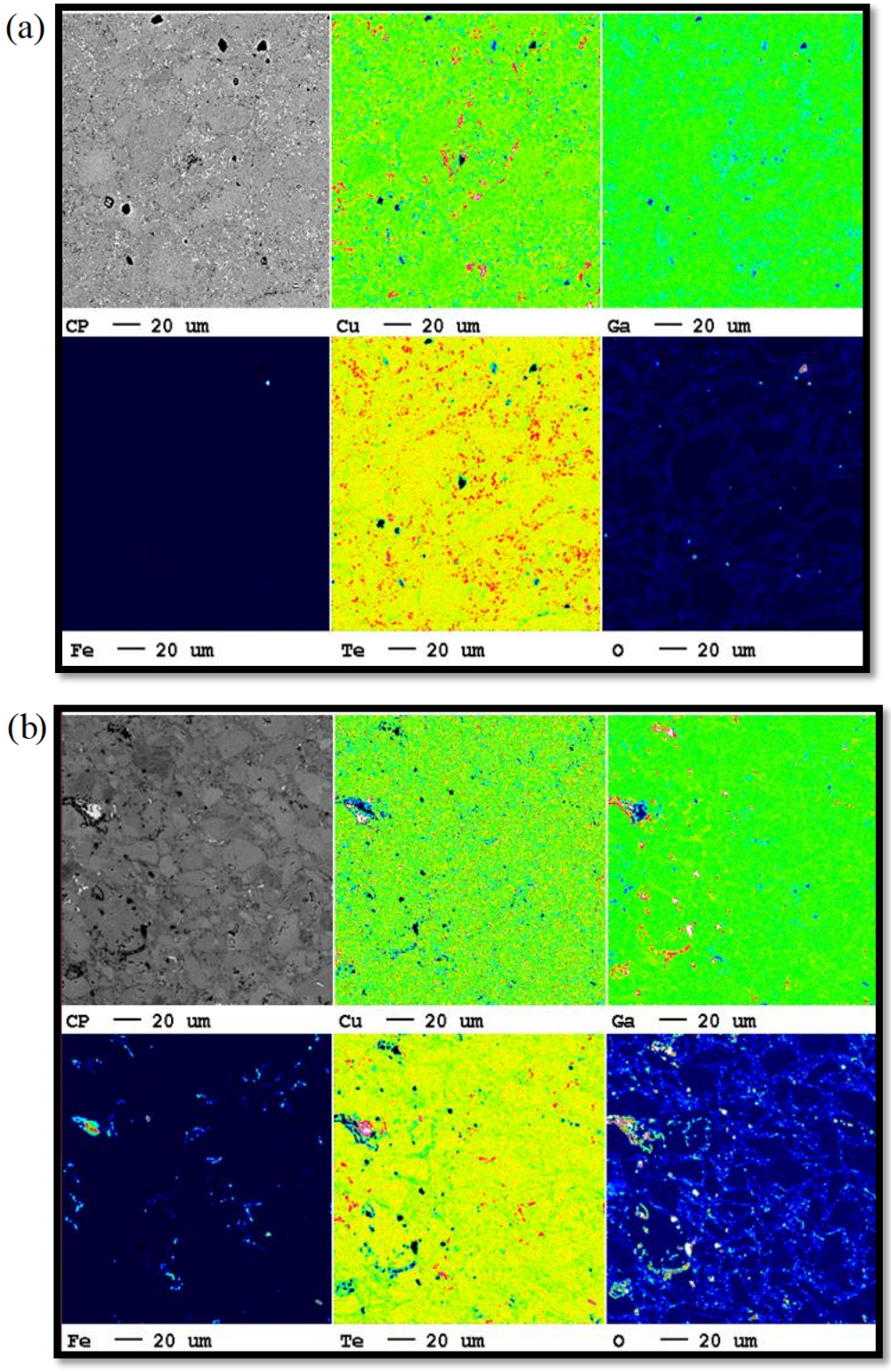

Figure 5. 4 displays mapping of the elements (Cu), (Ga) (Fe) (Te) and (O) for the sample (a) $CuGaTe_2$ and (b) $CuGa_{0.99}Fe_{0.01}Te_2$.

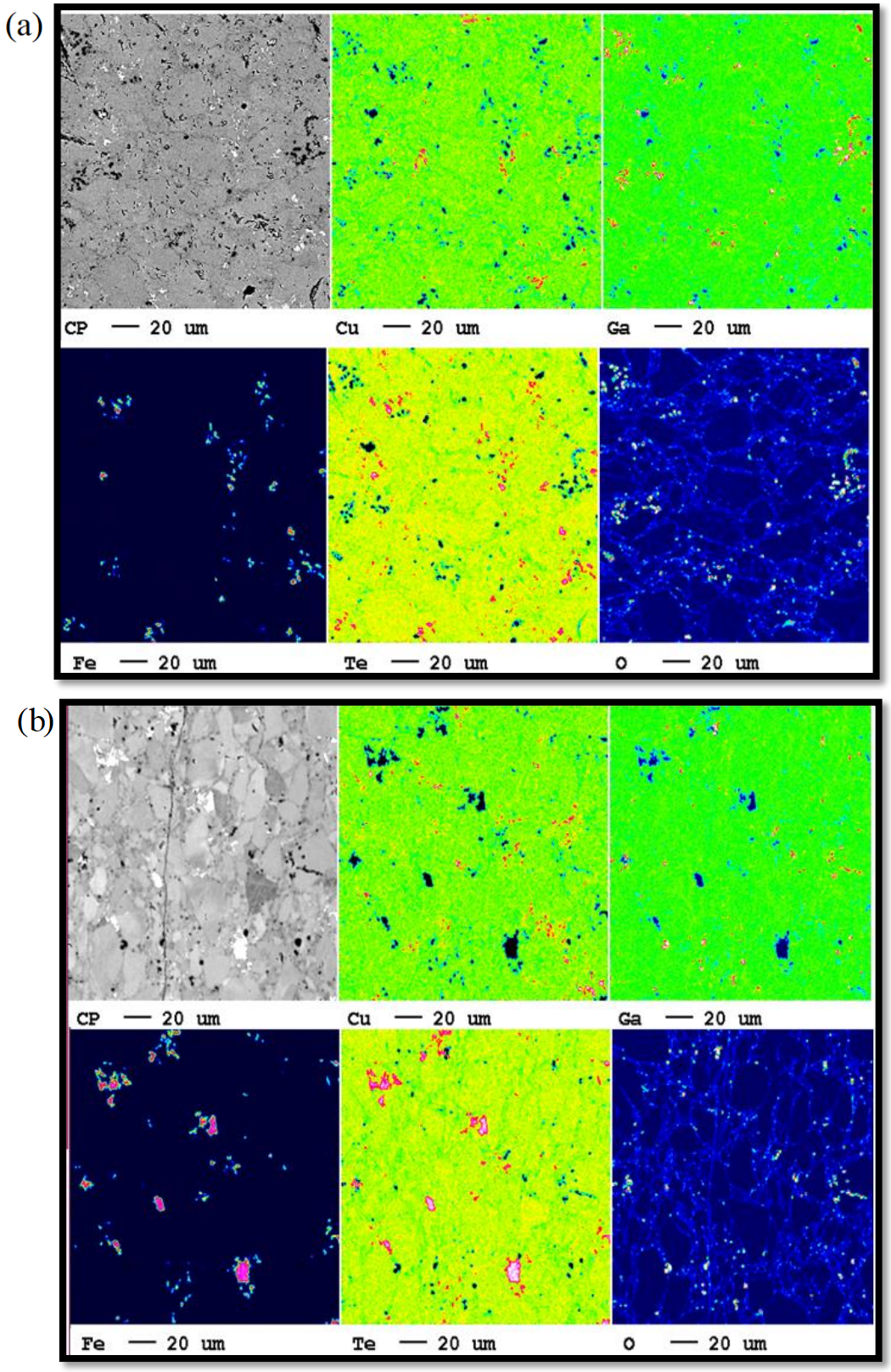

Figure 5. 5 displays mapping of the elements (Cu), (Ga) (Fe) (Te) and (O) for the sample (a) $CuGa_{0.98}Fe_{0.02}Te_2$.and (b) $CuGa_{0.97}Fe_{0.03}Te_2$

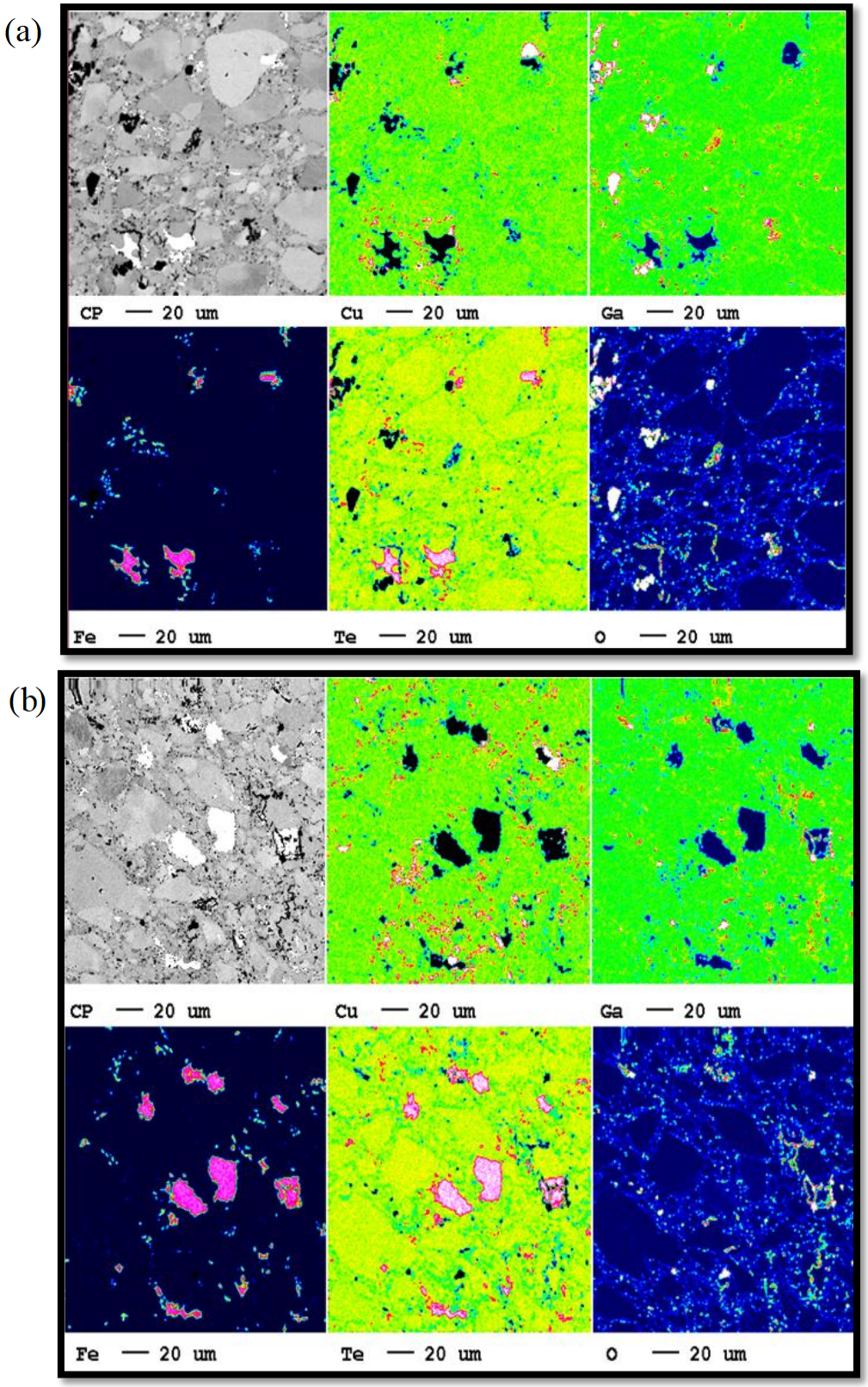

Figure 5. 6 displays mapping of the elements (Cu), (Ga) (Fe) (Te) and (O) for the sample (a) $CuGa_{0.96}Fe_{0.04}Te_2$. (b) $CuGa_{0.95}Fe_{0.05}Te_2$.

5. Thermoelectric Properties

Figure 5.7 shows plots of electrical resistivity as a function of temperature for $CuGa_{1-x}Fe_xTe_2$ where $x = 0.0$-0.05. As seen in Figure 5.7 (a) Resistivity values drops as temperature increases for all synthesized samples. This is usual behavior for a semiconductor. Below 600 K electrical resistivity values for Fe doped samples exhibit lower values as compared to pristine $CuGaTe_2$. However, Above 600 K first electrical values shows decrease with Fe concentration up to $x = 0.02$, and then slightly increased for $x \geq 0.03$. As discussed in previous section small amount of Fe was incorporated in the main phase of $CuGaTe_2$. This behavior of resistivity is might be due to the influence of minority phases. $FeTe_2$ is a narrow band gap semiconductor and exhibit much smaller values of electrical resistivity as compared to that of $CuGaTe_2$. [182], [183]. Therefore, the secondary phase might assist in the decrease of electrical resistivity up to 3% of Fe doping. However, for higher doping concentration ($x \geq 4\%$) as seen in elemental mapping secondary phase like CuTe starts to grow as seen in Figure 5.6. This may be one of the reason behind the resistivity increase with *Fe* concentration at high *T* range. However, small change in the chemical composition of the samples or the densities might influence the behavior of electrical resistivity as a function of Fe doping.

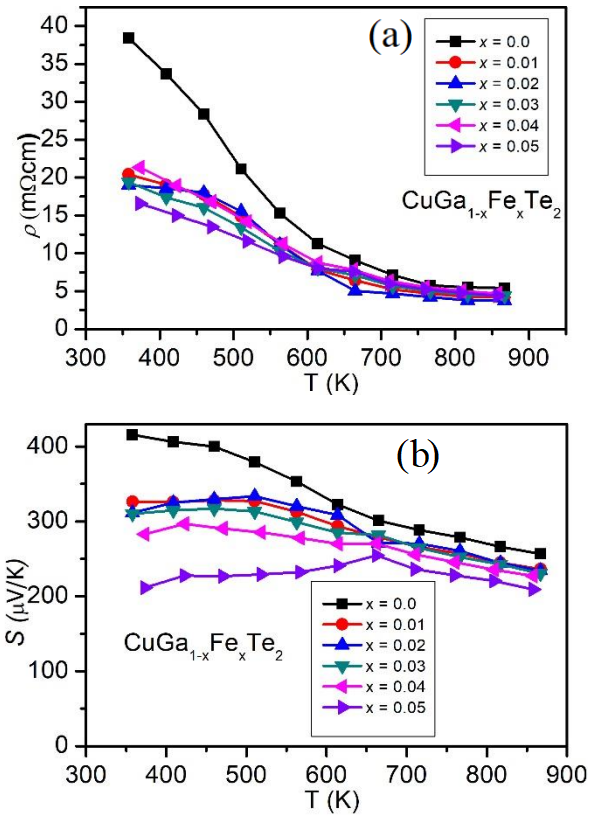

Figure 5. 7 (a) Plots of electrical resistivity (b) Seebeck Coefficient as a function of temperature for $CuGa_{1-x}Fe_xTe_2$ where x = 0.0-0.05.

Seebeck coefficient graphs as function of temperature are presented in Figure 5.7 (b). All samples exhibit positive values of Seebeck coefficient indicating *p*-type behavior. All samples show drop in the Seebeck coefficient values with increase in temperature. This trend was also observed in previous reports on $CuGaTe_2$ [10], [16] and attributed to thermally excitation of charge carriers at elevated temperature. Slight reduction in the values of Seebeck coefficient was observed after Fe doping thereby, power factor, S^2/ρ is improved as seen in Figure 5.8. Maximum value of power factor was 1.61 mW/K^2m for 2 % Fe doped sample at 770 K.

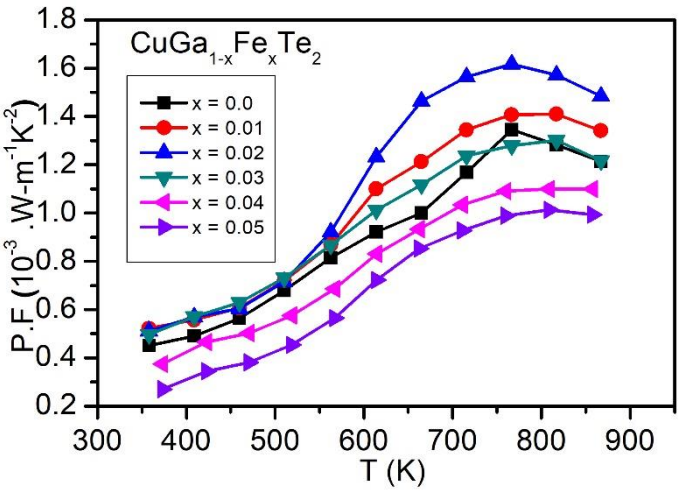

Figure 5. 8 Plots of Power factor as a function of temperature for $CuGa_{1-x}Fe_xTe_2$ where x = 0.0-0.05.

6. Thermal Transport Properties

Thermal conductivity measurements were carried out using Laser flash analysis. Results are plotted as a function of temperature in Figure 5.9. Thermal conductivity comprises of two main contributions can expressed as follow

$$\kappa_{tot} = \kappa_e + \kappa_{latt}$$

Here, κ_e represents electronic contribution towards total thermal conductivity and was evaluated using Wiedemann Franz Law, $\kappa_e = LT/\rho$ Here, L denotes Lorenz number, and its value for degenerate limit (2.44×10^{-8} $W\Omega K^{-2}$) was used in calculation. Subtracting electronic contribution we obtained lattice thermal conductivity. Figure 5.9 (b) shows plots of lattice thermal conductivity as a function of temperature. From Figure 5.9 (a) and Figure 5.9 (b) it is clear that electronic contribution has small contribution whereas main contribution is from that of lattice thermal conductivity. As temperature increases thermal conductivity values drops. This type of behavior is usually observed for a crystal and is attributed to Umklapp scattering at higher temperature [184]. Usually $\kappa_{latt} \propto T^{-1}$ trend is observed for Umklapp scattering. Figure 5.9 (c) shows graph between inverse of temperature and lattice thermal conductivity. A linear relationship was observed as expected.

Another interesting behavior is observed by looking at Fe doping dependence on thermal conductivity as shown in Figure 5.9 (d). Initially we observed 30-40 % decrease in thermal conductivity up to $x = 0.02$. For higher doping concentrations $x \geq 0.03$ an increase in thermal conductivity was observed. This trend is closely related to microstructural change as shown in Figure 5.4-5.6. Below 3% Fe doping secondary phases like $FeTe_2$ had small size and dispersed on grain boundaries as seen in elemental mapping graphs. This leads to enhanced phonon scattering and results in lower thermal conductivity. However, for higher Fe doping concentrations $x \geq 0.03$ thermal conductivity shows increase as secondary phase grows to the order of 10 µm and $CuGa_{1-x}Fe_xTe_2$ acts as composite material. Thermal conductivity value of $FeTe_2$ is higher as compared to $CuGaTe_2$. Hence, thermal conductivity is reduced by addition of secondary phase as long as doping concentration is restricted below where $FeTe_2$ particles scattered only at grain boundaries.

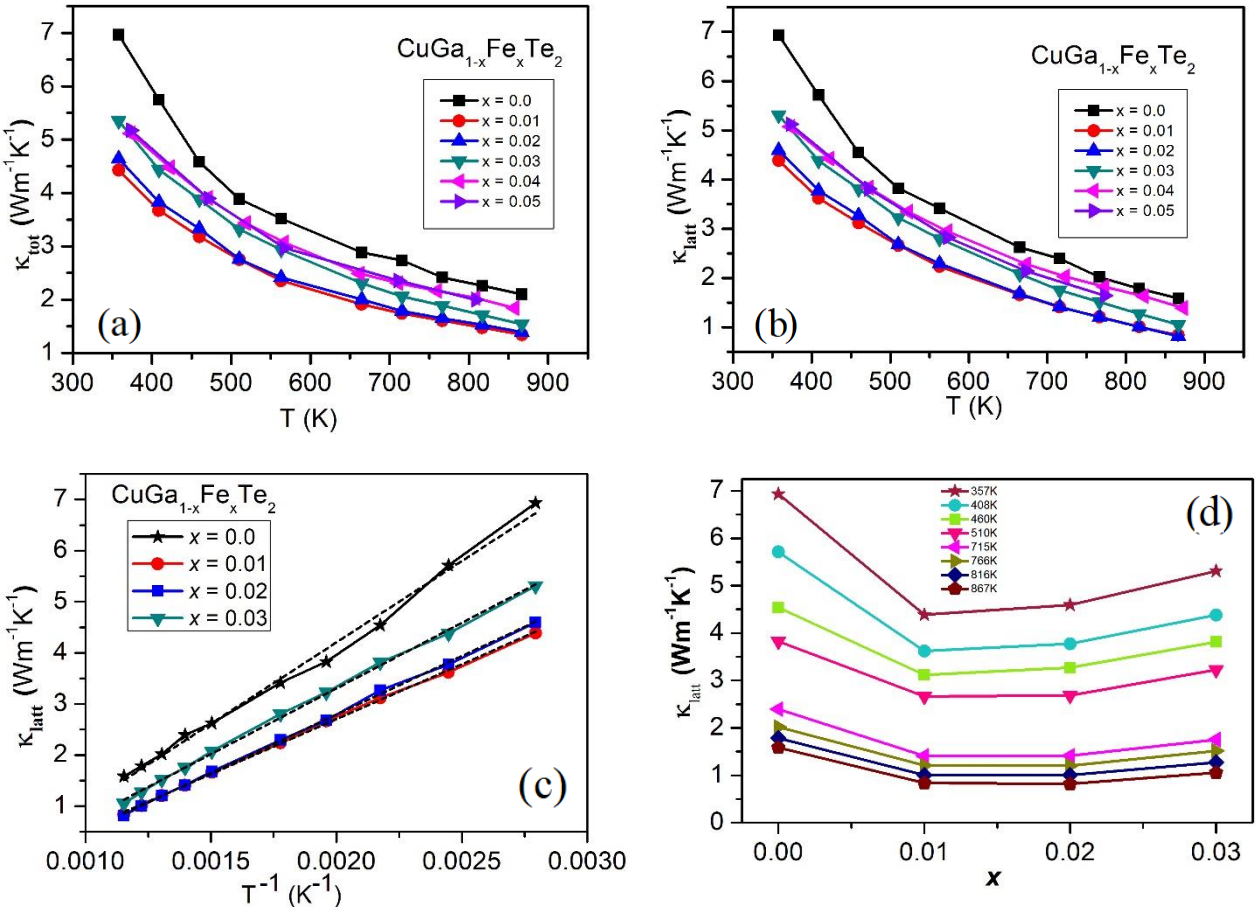

Figure 5. 9 Plots of (a) total thermal conductivity (b) lattice thermal conductivity as a function of temperature for $CuGa_{1-x}Fe_xTe_2$ where $x = 0.0$-0.05. (c) Lattice thermal conductivity plot with inverse of temperature. Black dotted lines shows linear fitting. (d) Lattice thermal conductivity values at different temperature as a function of Fe doping concentration

In the end we calculated Figure of merit (*ZT*) for all nominal samples. Results are plotted as a function of temperature in Figure 5.10. Significant increase in *ZT* value as observed as a result of Fe doping. Maximum *ZT* value of 0.92 calculated for $CuGa_{0.98}Fe_{0.02}Te_2$ at 870 K which is substantial enhancement as compared to pristine $CuGaTe_2$. Overall Fe incorporation was beneficial in improving thermoelectric properties. Secondary phases assisted in lowering thermal conductivity which contributed in improving *ZT* to the large extent. In a range of 1% to 2 %, Fe incorporation had useful effect on electrical properties as well which contributes towards improved power factor.

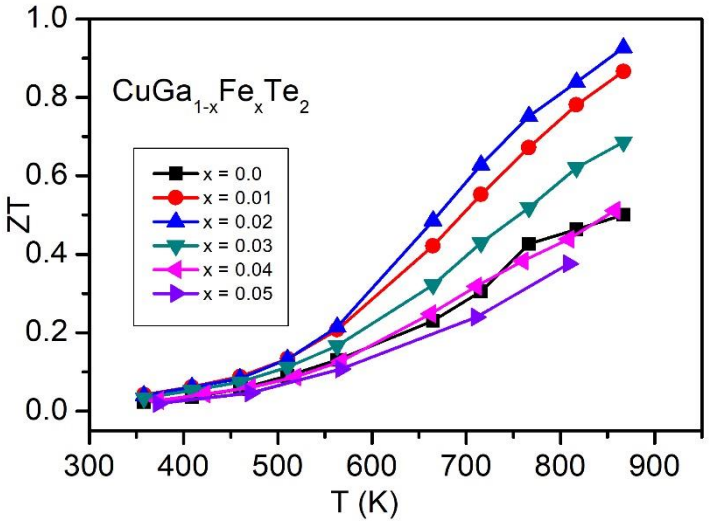

Figure 5. 10 Figure of merit (*ZT*) values as a function of temperature for $CuGa_{1-x}Fe_xTe_2$ where $x = 0.0$-0.05.

7. Summary points

1. Fe substitution and its effects on thermal transport and structural properties in chalcopyrite-type $CuGaTe_2$ were studied. In this work role of secondary phases and microstructural analysis towards improvement in thermoelectric properties of chalcopyrite $CuGaTe_2$ is demonstrated.
2. Fe has poor solubility inside $CuGaTe_2$ and as a result created secondary phases like $FeTe_2$.
3. Secondary phases helped in reduction of thermal conductivity up to certain limit of doping ($x \leq 3\%$).
4. Power factor has been improved with Fe addition as well. Thereby, Figure of merit (*ZT*) was enhanced and maximum value of 0.92 is obtained at 770 K for composition $CuGa_{0.98}Fe_{0.02}Te_2$. This is around 60 % improvement as compared to pristine $CuGaTe_2$
5. This work points to the significance of monitoring the microstructure of samples to improve thermoelectric properties

Conclusions and Outlook

A new idea of magnetic enhancement in power factor is presented. It has been demonstrated that by substituting a magnetic ion in $CuGaTe_2$, a significant enhancement in the power factor is observed. Using theoretical model interpretations and evaluating magnetic properties we showed power factor surpass normal carrier tuning effect. Owing to reduced thermal conductivity and carrier magnetic moments correlations we observed around 40 % enhancement in the power factor. Results demonstrate that magnetic ion doping is an effective technique to improve thermoelectric properties. In addition, open an opportunity for research on other thermoelectric families. We also presented thermoelectric and magnetic properties of $CuIn_{1-x}Mn_xTe_2$. Results showed that the Mn ions doped in $CuInTe_2$ are in the Mn^{3+} state. From the Curie-Weiss fitting, a strong antiferromagnetic interaction between Mn and carriers was inferred, which suggests the magnetic interaction is a probable origin for the enhanced power factor. Thermoelectric and magnetic properties of $CuIn_{1-x}Mn_xTe_2$ provides further evidence of carrier magnetic moments correlations presented in Chapter 3. Results reinforced the idea of magnetic enhancement in chalcopyrite type compounds and also revealed that magnetic moment and charge carrier interactions plays an essential role in enhancement of thermoelectric properties. In the last section of thesis we report results of Fe substitution and its effects on thermal transport and structural properties in chalcopyrite-type $CuGaTe_2$. In this work role of secondary phases and microstructural analysis towards improvement in thermoelectric properties of chalcopyrite $CuGaTe_2$ is demonstrated. Power factor has been improved with Fe addition as well. Thereby, Figure of merit (ZT) was enhanced and maximum value of 0.92 is obtained at 770 K for composition $CuGa_{0.98}Fe_{0.02}Te_2$. This is around 60 % improvement as compared to pristine $CuGaTe_2$.

Study in this thesis show that doping magnetic ion is feasible and bring extra contribution to improve the thermoelectric properties of chalcopyrite family. In future we aim to imply this mechanism of magnetic enhancement in other thermoelectric material families such as Silicides. We also believe that utilizing this technique in combination with other available mechanism i.e. Nano structuring will be an interesting research in future.

Appendix A

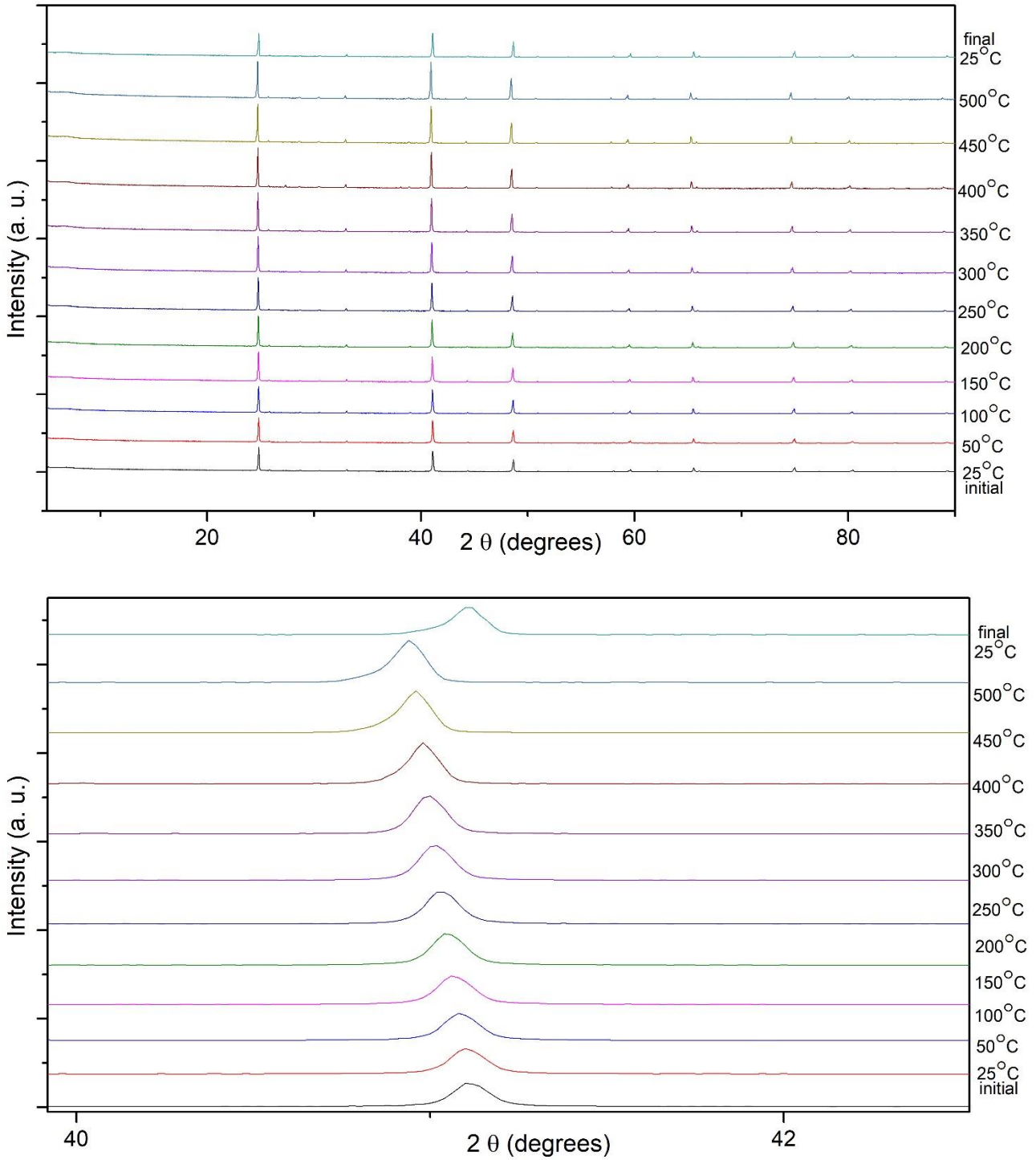

Figure A. Temperature dependent XRD- patterns for $CuInTe_2$. No phase transition observed up to 500 C.

References

[1] X. Shi, L. Chen, and C. Uher, "Recent advances in high-performance bulk thermoelectric materials," *Int. Mater. Rev.*, vol. 61, no. 6, pp. 379–415, 2016.

[2] T. Mori, "Novel Principles and Nanostructuring Methods for Enhanced Thermoelectrics," *Small*, vol. 13, no. 45, p. 1702013, 2017.

[3] D. M. Rowe, "Thermoelectrics, an environmentally-friendly source of electrical power," *Renew. Energy*, vol. 16, no. 1–4, pp. 1251–1256, 1999.

[4] H. J. Goldsmid, "Review of Thermoelectric Materials," in *Introduction to Thermoelectricity*, Berlin, Heidelberg: Springer Berlin Heidelberg, 2016, pp. 153–195.

[5] M. Hamid Elsheikh, D. A. Shnawah, M. F. M. Sabri, S. B. M. Said, M. Haji Hassan, M. B. Ali Bashir, and M. Mohamad, "A review on thermoelectric renewable energy: Principle parameters that affect their performance," *Renew. Sustain. Energy Rev.*, vol. 30, pp. 337–355, Feb. 2014.

[6] S. Chen and Z. Ren, "Recent progress of half-Heusler for moderate temperature thermoelectric applications," *Materials Today*. 2013.

[7] W. Xie, A. Weidenkaff, X. Tang, Q. Zhang, J. Poon, and T. Tritt, "Recent Advances in Nanostructured Thermoelectric Half-Heusler Compounds," *Nanomaterials*, 2012.

[8] K. Koumoto and T. Mori, Eds., *Thermoelectric Nanomaterials:Materials Design and Applications*. Heidelberg: Springer, 2013.

[9] G. D. Mahan, "Good Thermoelectrics," *Solid State Phys. - Adv. Res. Appl.*, vol. 51, no. C, pp. 81–157, 1997.

[10] T. Plirdpring, K. Kurosaki, A. Kosuga, T. Day, S. Firdosy, V. Ravi, G. J. Snyder, A. Harnwunggmoung, T. Sugahara, Y. Ohishi, H. Muta, and S. Yamanaka, "Chalcopyrite CuGaTe2: A high-efficiency bulk thermoelectric material," *Adv. Mater.*, vol. 24, no. 27, pp. 3622–3626, 2012.

[11] N. Tsujii and T. Mori, "High thermoelectric power factor in a carrier-doped magnetic semiconductor cufes2," *Appl. Phys. Express*, vol. 6, no. 4, p. 043001, 2013.

[12] N. Tsujii, T. Mori, and Y. Isoda, "Phase stability and thermoelectric properties of CuFeS2-based magnetic semiconductor," *J. Electron. Mater.*, vol. 43, no. 6, pp. 2371–2375, 2014.

[13] R. Ang, A. U. Khan, N. Tsujii, K. Takai, R. Nakamura, and T. Mori, "Thermoelectricity Generation and Electron-Magnon Scattering in a Natural Chalcopyrite Mineral from a Deep-Sea Hydrothermal Vent," *Angew. Chemie - Int. Ed.*, vol. 54, no. 44, pp. 12909–12913, 2015.

[14] J. Shen, X. Zhang, Z. Chen, S. Lin, J. Li, W. Li, S. Li, Y. Chen, and Y. Pei, "Substitutional defects enhancing thermoelectric CuGaTe2," *J. Mater. Chem. A*, vol. 5, no. 11, pp. 5314–5320, 2017.

[15] Y. Li, Q. Meng, Y. Deng, H. Zhou, Y. Gao, Y. Li, J. Yang, and J. Cui, "High thermoelectric performance of solid solutions CuGa 1-xIn xTe 2 (x = 0-1.0)," *Appl. Phys. Lett.*, vol. 100, no. 23, 2012.

[16] M. Kumagai, K. Kurosaki, Y. Ohishi, H. Muta, and S. Yamanaka, "Effect of Ball-Milling Conditions on Thermoelectric Properties of Polycrystalline $CuGaTe_2$," *Mater. Trans.*, vol. 55, no.

8, pp. 1215–1218, 2014.

[17] J. Shen, Z. Chen, S. Lin, L. Zheng, W. Li, and Y. Pei, "Single parabolic band behavior of thermoelectric p-type CuGaTe2," *J. Mater. Chem. C*, vol. 4, no. 1, pp. 209–214, 2015.

[18] J. Zhang, X. Qin, D. Li, H. Xin, C. Song, L. Li, Z. Wang, G. Guo, and L. Wang, "Enhanced thermoelectric properties of Ag-doped compounds CuAgxGa1-xTe2($0 \leq x \leq 0.05$)," *J. Alloys Compd.*, vol. 586, pp. 285–288, 2014.

[19] W. D. Carr and D. T. Morelli, "Influence of doping and solid solution formation on the thermoelectric properties of chalcopyrite semiconductors," *J. Alloys Compd.*, vol. 630, pp. 277–281, 2015.

[20] F. Ahmed, N. Tsujii, and T. Mori, "Thermoelectric properties of CuGa1−xMnxTe2: power factor enhancement by incorporation of magnetic ions," *J. Mater. Chem. A*, vol. 5, no. 16, pp. 7545–7554, 2017.

[21] F. Ahmed, N. Tsujii, and T. Mori, "Microstructure analysis and thermoelectric properties of iron doped CuGaTe2," *J. Mater.*, vol. 4, no. 3, pp. 221–227, Sep. 2018.

[22] D. M. Rowe, Ed., *Thermoelectrics and Its Energy Harvesting*. Boca Raton: CRC Press, 2012.

[23] M. Cutler, J. F. Leavy, and R. L. Fitzpatrick, "Electronic transport in semimetallic cerium sulfide," *Phys. Rev.*, vol. 133, no. 4A, p. A1143, 1964.

[24] G. J. Snyder and E. S. Toberer, "Complex thermoelectric materials," *Nat. Mater.*, vol. 7, no. 2, pp. 105–114, 2008.

[25] Y. Pei, H. Wang, and G. J. Snyder, "Band engineering of thermoelectric materials," *Advanced Materials*, vol. 24, no. 46. pp. 6125–6135, 2012.

[26] C. Gayner and K. K. Kar, "Recent advances in thermoelectric materials," *Prog. Mater. Sci.*, vol. 83, pp. 330–382, Oct. 2016.

[27] X. Zhang and L.-D. Zhao, "Thermoelectric materials: Energy conversion between heat and electricity," *J. Mater.*, vol. 1, no. 2, pp. 92–105, Jun. 2015.

[28] A. J. Minnich, M. S. Dresselhaus, Z. F. Ren, and G. Chen, "Bulk nanostructured thermoelectric materials: current research and future prospects," *Energy Environ. Sci.*, 2009.

[29] D. M. Rowe, *CRC Handbook of Thermoelectrics*. 1995.

[30] L. E. Bell, "Cooling, heating, generating power, and recovering waste heat with thermoelectric systems," *Science (80-.).*, vol. 321, no. 5895, pp. 1457–1461, 2008.

[31] F. J. Disalvo, "Thermoelectric cooling and power generation," *Science (80-.).*, vol. 285, no. 5428, pp. 703–706, 1999.

[32] R. Chein and G. Huang, "Thermoelectric cooler application in electronic cooling," *Appl. Therm. Eng.*, vol. 24, no. 14–15, pp. 2207–2217, 2004.

[33] D. Enescu and E. O. Virjoghe, "A review on thermoelectric cooling parameters and performance," *Renew. Sustain. Energy Rev.*, vol. 38, pp. 903–916, 2014.

[34] H. J. Goldsmid, *Introduction to thermoelectricity / H. Julian Goldsmid.* 2016.

[35] X. Zhang and L.-D. Zhao, "Thermoelectric materials: Energy conversion between heat and

electricity," *J. Mater.*, vol. 1, no. 2, pp. 92–105, Jun. 2015.

[36] M. Sajid, I. Hassan, and A. Rahman, "An overview of cooling of thermoelectric devices," *Renew. Sustain. Energy Rev.*, vol. 78, pp. 15–22, Oct. 2017.

[37] G. J. Snyder, E. S. Toberer, R. Khanna, and W. Seifert, "Improved thermoelectric cooling based on the Thomson effect," *Phys. Rev. B - Condens. Matter Mater. Phys.*, vol. 86, no. 4, 2012.

[38] X. F. Zheng, C. X. Liu, Y. Y. Yan, and Q. Wang, "A review of thermoelectrics research - Recent developments and potentials for sustainable and renewable energy applications," *Renew. Sustain. Energy Rev.*, vol. 32, pp. 486–503, 2014.

[39] Y. Pei, X. Shi, A. Lalonde, H. Wang, L. Chen, and G. J. Snyder, "Convergence of electronic bands for high performance bulk thermoelectrics," *Nature*, vol. 473, no. 7345, pp. 66–69, 2011.

[40] H. Wang, Z. M. Gibbs, Y. Takagiwa, and G. J. Snyder, "Tuning bands of PbSe for better thermoelectric efficiency," *Energy Environ. Sci.*, vol. 7, no. 2, pp. 804–811, 2014.

[41] M. Cutler and N. F. Mott, "Observation of anderson localization in an electron gas," *Phys. Rev.*, vol. 181, no. 3, pp. 1336–1340, 1969.

[42] W. Liu, X. Tan, K. Yin, H. Liu, X. Tang, J. Shi, Q. Zhang, and C. Uher, "Convergence of conduction bands as a means of enhancing thermoelectric performance of n-type Mg 2Si 1-xSn x solid solutions," *Phys. Rev. Lett.*, vol. 108, no. 16, pp. 166601-1–5, 2012.

[43] Y. Tang, Z. M. Gibbs, L. A. Agapito, G. Li, H.-S. Kim, M. B. Nardelli, S. Curtarolo, and G. J. Snyder, "Convergence of multi-valley bands as the electronic origin of high thermoelectric performance in CoSb3 skutterudites," *Nat. Mater.*, vol. 14, pp. 1223–1228, Oct. 2015.

[44] N. W. Ashcroft and N. D. Mermin, *Solid State Physics*. Brooks cole, 1976.

[45] W. v. Muench and H. Statz, "Solid-to-solid diffusion in the gallium arsenide device technology," *Solid State Electron.*, vol. 9, no. 10, pp. 939–942, 1966.

[46] B. Poudel, Q. Hao, Y. Ma, Y. Lan, A. Minnich, B. Yu, X. Yan, D. Wang, A. Muto, D. Vashaee, X. Chen, J. Liu, M. S. Dresselhaus, G. Chen, and Z. Ren, "High-thermoelectric performance of nanostructured bismuth antimony telluride bulk alloys," *Science (80-.).*, vol. 320, no. 5876, pp. 634–638, 2008.

[47] Z. G. Chen, G. Hana, L. Yanga, L. Cheng, and J. Zou, "Nanostructured thermoelectric materials: Current research and future challenge," *Prog. Nat. Sci. Mater. Int.*, vol. 22, no. 6, pp. 535–549, 2012.

[48] L. Yang, Z.-G. Chen, M. Hong, G. Han, and J. Zou, "Enhanced Thermoelectric Performance of Nanostructured Bi2Te3 through Significant Phonon Scattering," *ACS Appl. Mater. Interfaces*, vol. 7, no. 42, pp. 23694–23699, Oct. 2015.

[49] M. Hong, Z.-G. Chen, L. Yang, and J. Zou, "Enhancing thermoelectric performance of Bi2Te3-based nanostructures through rational structure design," *Nanoscale*, vol. 8, no. 16, pp. 8681–8686, 2016.

[50] Y. Ma, Q. Hao, B. Poudel, Y. Lan, B. Yu, D. Wang, G. Chen, and Z. Ren, "Enhanced thermoelectric figure-of-merit in p-type nanostructured bismuth antimony tellurium alloys made

from elemental chunks," *Nano Lett.*, vol. 8, no. 8, pp. 2580–2584, 2008.

[51] J. R. Szczech, J. M. Higgins, and S. Jin, "Enhancement of the thermoelectric properties in nanoscale and nanostructured materials," *J. Mater. Chem.*, vol. 21, no. 12, pp. 4037–4055, 2011.

[52] J. Androulakis, K. F. Hsu, R. Pcionek, H. Kong, C. Uher, J. J. D'Angelo, A. Downey, T. Hogan, and M. G. Kanatzidis, "Nanostructuring and high thermoelectric efficiency in p-type Ag(Pb 1-ySny)mSbTe2+m," *Adv. Mater.*, vol. 18, no. 9, pp. 1170–1173, 2006.

[53] B. A. Cook, M. J. Kramer, J. L. Harringa, M. K. Han, D. Y. Chung, and M. G. Kanatzidis, "Analysis of nanostructuring in high figure-of-merit Ag-1-x Pbm SbTe2+m thermoelectric materials," *Adv. Funct. Mater.*, vol. 19, no. 8, pp. 1254–1259, 2009.

[54] P. F. P. Poudeu, A. Guéguen, C. I. Wu, T. Hogan, and M. G. Kanatzidis, "High figure of merit in nanostructured n-type KPbmSbTe m+2 thermoelectric materials," *Chem. Mater.*, vol. 22, no. 3, pp. 1046–1053, 2010.

[55] P. F. P. Poudeu, J. D'Angelo, A. D. Downey, J. L. Short, T. P. Hogan, and M. G. Kanatzidis, "High thermoelectric figure of merit and nanostructuring in bulk p-type Na1-xPbmSbyTem+2," *Angew. Chemie - Int. Ed.*, vol. 45, no. 23, pp. 3835–3839, 2006.

[56] S. N. Girard, J. He, C. Li, S. Moses, G. Wang, C. Uher, V. P. Dravid, and M. G. Kanatzidis, "In situ nanostructure generation and evolution within a bulk thermoelectric material to reduce lattice thermal conductivity," *Nano Lett.*, vol. 10, no. 8, pp. 2825–2831, 2010.

[57] A. J. Minnich, M. S. Dresselhaus, Z. F. Ren, and G. Chen, "Bulk nanostructured thermoelectric materials: Current research and future prospects," *Energy Environ. Sci.*, vol. 2, no. 5, pp. 466–479, 2009.

[58] P. Pichanusakorn and P. Bandaru, "Nanostructured thermoelectrics," *Mater. Sci. Eng. R Reports*, vol. 67, no. 2–4, pp. 19–63, 2010.

[59] L. D. Hicks, T. C. Harman, and M. S. Dresselhaus, "Use of quantum-well from nonconventional to obtain a high figure of merit thermoelectric materials," *Appl. Phys. Lett.*, vol. 63, no. 7, pp. 3230–3232, 1993.

[60] L. D. Hicks, T. C. Harman, and M. S. Dresselhaus, "Use of quantum-well superlattices to obtain a high figure of merit from nonconventional thermoelectric materials," *Appl. Phys. Lett.*, vol. 63, no. 23, pp. 3230–3232, 1993.

[61] L. D. Hicks and M. S. Dresselhaus, "Thermoelectric figure of merit of a one-dimensional conductor," *Phys. Rev. B*, vol. 47, no. 24, pp. 16631–16634, 1993.

[62] M. G. Kanatzidis, "Nanostructured thermoelectrics: The new paradigm?," *Chem. Mater.*, vol. 22, no. 3, pp. 648–659, 2010.

[63] C. Kittel, *Introduction to Solid State Physics*. NewYork: John Wiley and Sons, 2004.

[64] W. Kim, "Strategies for engineering phonon transport in thermoelectrics," *J. Mater. Chem. C*, vol. 3, no. 40, pp. 10336–10348, 2015.

[65] C. L. Julian, "Theory of heat conduction in rare-gas crystals," *Phys. Rev.*, vol. 137, no. 1, pp. A128–A137, 1965.

[66] Z. Chen, X. Zhang, and Y. Pei, "Manipulation of Phonon Transport in Thermoelectrics," *Adv. Mater.*, vol. 30, no. 17, p. 1705617, 2018.

[67] R. P. CHASMAR and R. STRATTON, "The Thermoelectric Figure of Merit and its Relation to Thermoelectric Generators†," *J. Electron. Control*, vol. 7, no. 1, pp. 52–72, Jul. 1959.

[68] G. S. Nolas, J. Sharp, and H. J. Goldsmid, *Thermoelectrics: Basic Principles and New Materials Developments*, 1st ed. NewYork: Springer, 2001.

[69] J. Zhang, L. Song, S. H. Pedersen, H. Yin, L. T. Hung, and B. B. Iversen, "Discovery of high-performance low-cost n-type Mg3Sb2-based thermoelectric materials with multi-valley conduction bands," *Nat. Commun.*, 2017.

[70] J. P. Heremans, V. Jovovic, E. S. Toberer, A. Saramat, K. Kurosaki, A. Charoenphakdee, S. Yamanaka, and G. J. Snyder, "Enhancement of thermoelectric efficiency in PbTe by distortion of the electronic density of states," *Science (80-.).*, vol. 321, no. 5888, pp. 554–557, 2008.

[71] T. Koga, X. Sun, S. B. Cronin, and M. S. Dresselhaus, "Carrier pocket engineering to design superior thermoelectric materials using GaAs/AlAs superlattices," *Appl. Phys. Lett.*, vol. 73, no. 20, pp. 2950–2952, 1998.

[72] O. Rabina, Y.-M. Lin, and M. S. Dresselhaus, "Anomalously high thermoelectric figure of merit in Bi1−xSbx nanowires by carrier pocket alignment," *Appl. Phys. Lett.*, vol. 79, no. 1, pp. 81–83, 2001.

[73] H. J. Goldsmid and R. W. Douglas, "The use of semiconductors in thermoelectric refrigeration," *Br. J. Appl. Phys.*, vol. 5, no. 11, pp. 386–390, 1954.

[74] D. Li, R. R. Sun, and X. Y. Qin, "Improving thermoelectric properties of p-type Bi2Te3-based alloys by spark plasma sintering," *Prog. Nat. Sci. Mater. Int.*, vol. 21, no. 4, pp. 336–340, 2011.

[75] W. Xie, J. He, H. J. Kang, X. Tang, S. Zhu, M. Laver, S. Wang, J. R. D. Copley, C. M. Brown, Q. Zhang, and T. M. Tritt, "Identifying the specific nanostructures responsible for the high thermoelectric performance of (Bi,Sb)2Te3nanocomposites," *Nano Lett.*, vol. 10, no. 9, pp. 3283–3289, 2010.

[76] J. Li, Q. Tan, J. F. Li, D. W. Liu, F. Li, Z. Y. Li, M. Zou, and K. Wang, "BiSbTe-based nanocomposites with high ZT: The effect of SiC nanodispersion on thermoelectric properties," *Adv. Funct. Mater.*, vol. 23, no. 35, pp. 4317–4323, 2013.

[77] S. Il Kim, K. H. Lee, H. A. Mun, H. S. Kim, S. W. Hwang, J. W. Roh, D. J. Yang, W. H. Shin, X. S. Li, Y. H. Lee, G. J. Snyder, and S. W. Kim, "Dense dislocation arrays embedded in grain boundaries for high-performance bulk thermoelectrics," *Science (80-.).*, vol. 348, no. 6230, pp. 109–114, 2015.

[78] F. Wu, H. Song, J. Jia, and X. Hu, "Thermoelectric properties of rare earth-doped n-type Bi2Se0.3Te2.7 nanocomposites," *Bull. Mater. Sci.*, vol. 37, no. 5, pp. 1007–1012, 2014.

[79] Z. H. Dughaish, "Lead telluride as a thermoelectric material for thermoelectric power generation," *Phys. B Condens. Matter*, vol. 322, no. 1–2, pp. 205–223, 2002.

[80] A. D. LaLonde, Y. Pei, and G. J. Snyder, "Reevaluation of PbTe1−xIx as high performance n-type

thermoelectric material," *Energy Environ. Sci.*, vol. 4, no. 6, p. 2090, 2011.

[81] Y. Pei, A. D. LaLonde, N. A. Heinz, and G. J. Snyder, "High thermoelectric figure of merit in PbTe alloys demonstrated in PbTe-CdTe," *Adv. Energy Mater.*, vol. 2, no. 6, pp. 670–675, 2012.

[82] Y. Lan, A. J. Minnich, G. Chen, and Z. Ren, "Enhancement of thermoelectric figure-of-merit by a bulk nanostructuring approach," *Adv. Funct. Mater.*, 2010.

[83] O. Delaire, J. Ma, K. Marty, A. F. May, M. A. McGuire, M.-H. Du, D. J. Singh, A. Podlesnyak, G. Ehlers, M. D. Lumsden, and B. C. Sales, "Giant anharmonic phonon scattering in PbTe," *Nat. Mater.*, vol. 10, p. 614, Jun. 2011.

[84] K. F. Hsu, S. Loo, F. Guo, W. Chen, J. S. Dyck, C. Uher, T. Hogan, E. K. Polychroniadis, and M. G. Kanatzidis, "Cubic AgPbmSbTe2+m: Bulk Thermoelectric Materials with High Figure of Merit," *Science (80-.).*, vol. 303, no. 5659, pp. 818–821, 2004.

[85] B. Paul, P. K. Rawat, and P. Banerji, "Dramatic enhancement of thermoelectric power factor in PbTe:Cr co-doped with iodine," *Appl. Phys. Lett.*, vol. 98, no. 26, 2011.

[86] A. Nozariasbmarz, A. Agarwal, Z. A. Coutant, M. J. Hall, J. Liu, R. Liu, A. Malhotra, P. Norouzzadeh, M. C. Öztürk, V. P. Ramesh, Y. Sargolzaeiaval, F. Suarez, and D. Vashaee, "Thermoelectric silicides: A review," *Jpn. J. Appl. Phys.*, vol. 56, p. 05DA04-1-27, 2017.

[87] C. Gayner and K. K. Kar, "Recent advances in thermoelectric materials," *Prog. Mater. Sci.*, vol. 83, pp. 330–382, 2016.

[88] A. T. Burkov, "Silicide Thermoelectrics: Materials for Energy Harvesting," *Phys. Status Solidi A*, vol. 215, no. 17, p. 1800105, 2018.

[89] D. M. Rowe, V. S. Shukla, and N. Savvides, "Phonon scattering at grain boundaries in heavily doped fine-grained silicon-germanium alloys," *Nature*, vol. 290, no. 5809, pp. 765–766, 1981.

[90] C. B. Vining, W. Laskow, J. O. Hanson, R. R. Van Der Beck, and P. D. Gorsuch, "Thermoelectric properties of pressure-sintered Si0.8Ge0.2thermoelectric alloys," *J. Appl. Phys.*, vol. 69, no. 8, pp. 4333–4340, 1991.

[91] X. W. Wang, H. Lee, Y. C. Lan, G. H. Zhu, G. Joshi, D. Z. Wang, J. Yang, A. J. Muto, M. Y. Tang, J. Klatsky, S. Song, M. S. Dresselhaus, G. Chen, and Z. F. Ren, "Enhanced thermoelectric figure of merit in nanostructured n-type silicon germanium bulk alloy," *Appl. Phys. Lett.*, vol. 93, no. 19, p. 193121, Nov. 2008.

[92] S. Ahmad, R. Basu, P. Sarkar, A. Singh, A. Bohra, S. Bhattacharya, R. Bhatt, K. N. Meshram, S. Samanta, P. Bhatt, M. Navaneethan, Y. Hayakawa, A. K. Debnath, S. K. Gupta, D. K. Aswal, K. P. Muthe, and S. C. Gadkari, "Enhanced thermoelectric figure-of-merit of p-type SiGe through TiO2 nanoinclusions and modulation doping of boron," *Materialia*, Sep. 2018.

[93] J. Choi, K. Cho, and S. Kim, "Flexible Thermoelectric Generators Composed of n-and p-Type Silicon Nanowires Fabricated by Top-Down Method," *Adv. Energy Mater.*, 2017.

[94] D. Dávila, A. Tarancón, C. Calaza, M. Salleras, M. Fernández-Regúlez, A. San Paulo, and L. Fonseca, "Monolithically integrated thermoelectric energy harvester based on silicon nanowire arrays for powering micro/nanodevices," *Nano Energy*, vol. 1, no. 6, pp. 812–819, Nov. 2012.

[95] J. Lim, K. Hippalgaonkar, S. C. Andrews, A. Majumdar, and P. Yang, "Quantifying surface roughness effects on phonon transport in silicon nanowires," *Nano Lett.*, 2012.

[96] D. Beretta, N. Neophytou, J. M. Hodges, M. G. Kanatzidis, D. Narducci, M. Martin-Gonzalez, M. Beekman, B. Balke, G. Cerretti, W. Tremel, A. Zevalkink, A. I. Hofmann, C. Müller, B. Dörling, M. Campoy-Quiles, and M. Caironi, "Thermoelectrics: From history, a window to the future," *Materials Science and Engineering R: Reports*, Elsevier, 03-Nov-2018.

[97] L. D. Zhao, C. Chang, G. Tan, and M. G. Kanatzidis, "SnSe: A remarkable new thermoelectric material," *Energy Environ. Sci.*, vol. 9, no. 10, pp. 3044–3060, 2016.

[98] T.-R. Wei, C.-F. Wu, F. Li, and J.-F. Li, "Low-cost and environmentally benign selenides as promising thermoelectric materials," *J. Mater.*, vol. 4, no. 4, pp. 304–320, Dec. 2018.

[99] L.-D. Zhao, S.-H. Lo, Y. Zhang, H. Sun, G. Tan, C. Uher, C. Wolverton, V. P. Dravid, and M. G. Kanatzidis, "Ultralow thermal conductivity and high thermoelectric figure of merit in SnSe crystals," *Nature*, vol. 508, p. 373, Apr. 2014.

[100] Z. G. Chen, X. Shi, L. D. Zhao, and J. Zou, "High-performance SnSe thermoelectric materials: Progress and future challenge," *Progress in Materials Science*, vol. 97. pp. 283–346, 2018.

[101] L. D. Zhao, G. Tan, S. Hao, J. He, Y. Pei, H. Chi, H. Wang, S. Gong, H. Xu, V. P. Dravid, C. Uher, G. J. Snyder, C. Wolverton, and M. G. Kanatzidis, "Ultrahigh power factor and thermoelectric performance in hole-doped single-crystal SnSe," *Science (80-.).*, vol. 351, no. 6269, pp. 141–144, 2016.

[102] T. R. Wei, G. Tan, C. F. Wu, C. Chang, L. D. Zhao, J. F. Li, G. J. Snyder, and M. G. Kanatzidis, "Thermoelectric transport properties of polycrystalline SnSe alloyed with PbSe," *Appl. Phys. Lett.*, vol. 110, no. 5, 2017.

[103] M. Gharsallah, F. Serrano-Sánchez, N. M. Nemes, F. J. Mompeán, J. L. Martínez, M. T. Fernández-Díaz, F. Elhalouani, and J. A. Alonso, "Giant Seebeck effect in Ge-doped SnSe," *Sci. Rep.*, 2016.

[104] G. Tang, W. Wei, J. Zhang, Y. Li, X. Wang, G. Xu, C. Chang, Z. Wang, Y. Du, and L. D. Zhao, "Realizing High Figure of Merit in Phase-Separated Polycrystalline Sn1-xPbxSe," *J. Am. Chem. Soc.*, vol. 138, no. 41, pp. 13647–13654, 2016.

[105] Y. M. Han, J. Zhao, M. Zhou, X. X. Jiang, H. Q. Leng, and L. F. Li, "Thermoelectric performance of SnS and SnS-SnSe solid solution," *J. Mater. Chem. A*, vol. 3, no. 8, pp. 4555–4559, 2015.

[106] Asfandiyar, T. R. Wei, Z. Li, F. H. Sun, Y. Pan, C. F. Wu, M. U. Farooq, H. Tang, F. Li, B. Li, and J. F. Li, "Thermoelectric SnS and SnS-SnSe solid solutions prepared by mechanical alloying and spark plasma sintering: Anisotropic thermoelectric properties," *Sci. Rep.*, vol. 7, 2017.

[107] H. Guo, H. Xin, X. Qin, J. Zhang, D. Li, Y. Li, C. Song, and C. Li, "Enhanced thermoelectric performance of highly oriented polycrystalline SnSe based composites incorporated with SnTe nanoinclusions," *J. Alloys Compd.*, vol. 689, pp. 87–93, 2016.

[108] F. Chu, Q. Zhang, Z. Zhou, D. Hou, L. Wang, and W. Jiang, "Enhanced thermoelectric and mechanical properties of Na-doped polycrystalline SnSe thermoelectric materials via CNTs

dispersion," *J. Alloys Compd.*, vol. 741, pp. 756–764, 2018.

[109] Y. Zhang, X. Jia, H. Sun, B. Sun, B. Liu, H. Liu, L. Kong, and H. Ma, "Effect of high pressure on thermoelectric performance and electronic structure of SnSe via HPHT," *J. Alloys Compd.*, 2016.

[110] Y. Li, F. Li, J. Dong, Z. Ge, F. Kang, J. He, H. Du, B. Li, and J. F. Li, "Enhanced mid-temperature thermoelectric performance of textured SnSe polycrystals made of solvothermally synthesized powders," *J. Mater. Chem. C*, 2016.

[111] X. Zhou, Y. Yan, X. Lu, H. Zhu, X. Han, G. Chen, and Z. Ren, "Routes for high-performance thermoelectric materials," *Mater. Today*, Apr. 2018.

[112] X. Shi, J. Yang, J. R. Salvador, M. Chi, J. Y. Cho, H. Wang, S. Bai, J. Yang, W. Zhang, and L. Chen, "Multiple-filled skutterudites: High thermoelectric figure of merit through separately optimizing electrical and thermal transports," *J. Am. Chem. Soc.*, vol. 133, no. 20, pp. 7837–7846, 2011.

[113] J. He and T. M. Tritt, "Advances in thermoelectric materials research: Looking back and moving forward," *Science (80-.).*, vol. 357, no. 6358, 2017.

[114] X. Shi, H. Kong, C. P. Li, C. Uher, J. Yang, J. R. Salvador, H. Wang, L. Chen, and W. Zhang, "Low thermal conductivity and high thermoelectric figure of merit in n -type Bax Yby Co4 Sb12 double-filled skutterudites," *Appl. Phys. Lett.*, vol. 92, no. 18, 2008.

[115] G. D. Tang, Z. H. Wang, X. N. Xu, Y. He, L. Qiu, and Y. W. Du, "Low thermal conductivity and enhanced thermoelectric performance in In and Lu double-filled CoSb 3 skutterudites," *J. Electron. Mater.*, vol. 40, no. 5, pp. 611–614, 2011.

[116] T. He, J. Chen, H. D. Rosenfeld, and M. A. Subramanian, "Thermoelectric properties of indium-filled skutterudites," *Chem. Mater.*, vol. 18, no. 3, pp. 759–762, 2006.

[117] S. Choi, K. Kurosaki, A. Harnwunggmoung, Y. Miyazaki, Y. Ohishi, H. Muta, and S. Yamanaka, "Enhancement of thermoelectric properties of CoSb3skutterudite by addition of Ga and in," *Jpn. J. Appl. Phys.*, vol. 54, no. 11, 2015.

[118] B. B. Iversen, A. E. C. Palmqvist, D. E. Cox, G. S. Nolas, G. D. Stucky, N. P. Blake, and H. Metiu, "Why are clathrates good candidates for thermoelectric materials?," *J. Solid State Chem.*, vol. 149, no. 2, pp. 455–458, 2000.

[119] M. Christensen, S. Johnsen, and B. B. Iversen, "Thermoelectric clathrates of type i," *Dalt. Trans.*, vol. 39, no. 4, pp. 978–992, 2010.

[120] A. Bentien, M. Christensen, J. D. Bryan, A. Sanchez, S. Paschen, F. Steglich, G. D. Stucky, and B. B. Iversen, "Thermal conductivity of thermoelectric clathrates," *Phys. Rev. B - Condens. Matter Mater. Phys.*, vol. 69, no. 4, 2004.

[121] G. S. Nolas, G. A. Slack, and S. B. Schujman, "Chapter 6 Semiconductor clathrates: A phonon glass electron crystal material with potential for thermoelectric applications," *Semicond. Semimetals*, 2001.

[122] G. S. Nolas, J. L. Cohn, G. A. Slack, and S. B. Schujman, "Semiconducting Ge clathrates: Promising candidates for thermoelectric applications," *Appl. Phys. Lett.*, vol. 73, no. 2, pp. 178–

180, 1998.

[123] J. A. Dolyniuk, B. Owens-Baird, J. Wang, J. V. Zaikina, and K. Kovnir, "Clathrate thermoelectrics," *Materials Science and Engineering R: Reports*, vol. 108, pp. 1–46, 2016.

[124] A. Saramat, G. Svensson, A. E. C. Palmqvist, C. Stiewe, E. Mueller, D. Platzek, S. G. K. Williams, D. M. Rowe, J. D. Bryan, and G. D. Stucky, "Large thermoelectric figure of merit at high temperature in Czochralski-grown clathrate Ba 8Ga 16Ge 30," *J. Appl. Phys.*, vol. 99, no. 2, 2006.

[125] M. Falmbigl, A. Grytsiv, P. Rogl, P. Heinrich, E. Royanian, and E. Bauer, "Tuning of band gap and thermoelectric properties of type-I clathrate Ba8NixZnyGe46-x-y-zSnz," *J. Alloys Compd.*, vol. 567, pp. 65–72, 2013.

[126] X. Shi, L. Chen, and C. Uher, "Recent advances in high-performance bulk thermoelectric materials," *Int. Mater. Rev.*, vol. 61, no. 6, pp. 379–415, 2016.

[127] "Review of thermoelectric materials," in *Springer Series in Materials Science*, vol. 121, 2016, pp. 153–195.

[128] X. Yan, G. Joshi, W. Liu, Y. Lan, H. Wang, S. Lee, J. W. Simonson, S. J. Poon, T. M. Tritt, G. Chen, and Z. F. Ren, "Enhanced thermoelectric figure of merit of p-type half-heuslers," *Nano Lett.*, vol. 11, no. 2, pp. 556–560, 2011.

[129] G. J. Poon, "Chapter 2 Electronic and thermoelectric properties of Half-Heusler alloys," *Semicond. Semimetals*, vol. 70, no. C, pp. 37–75, 2001.

[130] J. W. G. Bos and R. A. Downie, "Half-Heusler thermoelectrics: A complex class of materials," *J. Phys. Condens. Matter*, vol. 26, no. 43, 2014.

[131] L. Huang, Q. Zhang, B. Yuan, X. Lai, X. Yan, and Z. Ren, "Recent progress in half-Heusler thermoelectric materials," *Materials Research Bulletin*. 2016.

[132] M. Nygren and Z. Shen, "On the preparation of bio-, nano- and structural ceramics and composites by spark plasma sintering," *Solid State Sci.*, vol. 5, no. 1, pp. 125–131, 2003.

[133] A. V. Sergueeva, D. M. Hulbert, N. A. Mara, and A. K. Mukherjee, "Mechanical properties of nanocomposite materials," *Front. Nanosci.*, vol. 1, no. 1 A, pp. 127–172, Jan. 2009.

[134] Z. A. Munir, U. Anselmi-Tamburini, and M. Ohyanagi, "The effect of electric field and pressure on the synthesis and consolidation of materials: A review of the spark plasma sintering method," *J. Mater. Sci.*, vol. 41, no. 3, pp. 763–777, 2006.

[135] "No Title." [Online]. Available: https://www.cameca.com/products/epma/technique. [Accessed: 04-Jan-2019].

[136] "WEBPAGE." [Online]. Available: http://squid.iitd.ernet.in/Basic_Literature.htm. [Accessed: 04-Jan-2019].

[137] "Webpage." [Online]. Available: https://www.qdusa.com/products/ppms.html. [Accessed: 04-Jan-2019].

[138] J. Zhang, X. Qin, D. Li, H. Xin, C. Song, L. Li, X. Zhu, Z. Wang, G. Guo, and L. Wang, "Enhanced thermoelectric performance of CuGaTe2based composites incorporated with nanophase Cu2Se,"

J. Mater. Chem. A, vol. 2, no. 9, pp. 2891–2895, 2014.

[139] A. Yusufu, K. Kurosaki, Y. Ohishi, H. Muta, and S. Yamanaka, "Thermoelectric properties of chalcopyrite-type CuGaTe2with ag substituted into the Cu sites," *Jpn. J. Appl. Phys.*, vol. 52, no. 8, 2013.

[140] J. Zhang, X. Qin, D. Li, C. Song, X. Zhu, Y. Liu, H. Xin, L. Chen, and T. Zou, "Enhanced thermoelectric performance of CuGaTe2by Gd-doping and Te incorporation," *Intermetallics*, vol. 60, pp. 45–49, 2015.

[141] J. Zhang, X. Qin, D. Li, Y. Liu, Y. Li, C. Song, H. Xin, and X. Zhu, "Enhanced thermoelectric performance of CuGaTe2based composites incorporated with graphite nanosheets," *Appl. Phys. Lett.*, vol. 108, no. 7, 2016.

[142] W. Wu, Y. Li, Z. Du, Q. Meng, Z. Sun, W. Ren, and J. Cui, "Manipulation of the crystal structure defects: An alternative route to the reduction in lattice thermal conductivity and improvement in thermoelectric performance of CuGaTe2," *Appl. Phys. Lett.*, vol. 103, no. 1, p. 011905, 2013.

[143] L. Xue, Y.-M. Ren, and Z.-L. Hu, "Physical properties of chalcopyrite-type Cu1−xAgxGaTe2 by first-principles study," *Mod. Phys. Lett. B*, vol. 30, no. 30, p. 1650373, 2016.

[144] S. Sharma, B. Singh, and P. Kumar, "Doping effect on the thermoelectric properties of chalcopyrite CuGaTe2," in *AIP Conference Proceedings*, 2018, vol. 1953.

[145] J. Yang, Y. Yan, Y. X. Wang, and G. Yang, "Improved thermoelectric performance of CuGaTe2 with convergence of band valleys: A first-principles study," *RSC Adv.*, vol. 4, no. 54, pp. 28714–28720, 2014.

[146] L. Xue, B. Xu, D. Zhao, and L. Yi, "First-principles prediction the effect of lattice deformation on thermoelectric properties of CuGaTe2," *Comput. Mater. Sci.*, vol. 90, pp. 143–147, 2014.

[147] Y. Qin, P. Qiu, R. Liu, Y. Li, F. Hao, T. Zhang, D. Ren, X. Shi, and L. Chen, "Optimized thermoelectric properties in pseudocubic diamond-like CuGaTe2 compounds," *J. Mater. Chem. A*, vol. 4, no. 4, pp. 1277–1289, 2016.

[148] J. Cui, Y. Li, Z. Du, Q. Meng, and H. Zhou, "Promising defect thermoelectric semiconductors Cu<inf>1-x</inf>GaSb <inf>x</inf>Te<inf>2</inf> (x = 0-0.1) with the chalcopyrite structure," *J. Mater. Chem. A*, vol. 1, no. 3, pp. 677–683, 2013.

[149] D. M. Rowe and G. Min, ??"-in ?? plot as a thermoelectric material performance indicator," *J. Mater. Sci. Lett.*, vol. 14, no. 9, pp. 617–619, 1995.

[150] B. Jalan and S. Stemmer, "Large Seebeck coefficients and thermoelectric power factor of La-doped SrTiO3 thin films," *Appl. Phys. Lett.*, vol. 97, no. 4, p. 42106, 2010.

[151] E. S. Toberer, M. Christensen, B. B. Iversen, and G. J. Snyder, "High temperature thermoelectric efficiency in Ba8Ga16Ge30," *Phys. Rev. B*, vol. 77, no. 7, p. 75203, 2008.

[152] E. S. Toberer, A. F. May, B. C. Melot, E. Flage-Larsen, and G. J. Snyder, "Electronic structure and transport in thermoelectric compounds AZn2Sb2(A = Sr, Ca, Yb, Eu)," *Dalt. Trans.*, vol. 39, no. 4, pp. 1046–1054, 2010.

[153] H. Takaki, K. Kobayashi, M. Shimono, N. Kobayashi, K. Hirose, N. Tsujii, and T. Mori, "First-

principles calculations of Seebeck coefficients in a magnetic semiconductor CuFeS2," *Appl. Phys. Lett.*, vol. 110, no. 7, p. 072107, 2017.

[154] J. K. Furdyna, "Diluted magnetic semiconductors," *J. Appl. Phys.*, vol. 64, no. 4, pp. R29–R64, 1988.

[155] T. M. Giebultowicz, J. J. Rhyne, and J. K. Furdyna, "Mn-Mn exchange constants in zinc-manganese chalcogenides," *J. Appl. Phys.*, vol. 61, no. 8, pp. 3537–3539, 1987.

[156] J. Kondo, "Theory of Dilute Magnetic Alloys," vol. 23, F. Seitz, D. Turnbull, and H. Ehrenreich, Eds. Academic Press, 1970, pp. 183–281.

[157] M. A. Mayer, P. R. Stone, N. Miller, H. M. Smith, O. D. Dubon, E. E. Haller, K. M. Yu, W. Walukiewicz, X. Liu, and J. K. Furdyna, "Electronic structure of Ga1-x Mnx As analyzed according to hole-concentration-dependent measurements," *Phys. Rev. B - Condens. Matter Mater. Phys.*, vol. 81, no. 4, p. 045205, 2010.

[158] B. C. Sales, R. Jin, D. Mandrus, and P. Khalifah, "Anomalous Hall effect in three ferromagnetic compounds: Eu Fe4 Sb12, Yb14 Mn Sb11, and Eu8 Ga16 Ge30," *Phys. Rev. B - Condens. Matter Mater. Phys.*, vol. 73, no. 22, p. 224435, 2006.

[159] F. Matsukura, H. Ohno, A. Shen, and Y. Sugawara, "Transport properties and origin of ferromagnetism in (Ga, Mn)As," *Phys. Rev. B - Condens. Matter Mater. Phys.*, vol. 57, no. 4, pp. R2037–R2040, 1998.

[160] N. Manyala, Y. Sidis, J. F. Ditusa, G. Aeppli, D. P. Young, and Z. Fisk, "Large anomalous Hall effect in a silicon-based magnetic semiconductor," *Nat. Mater.*, vol. 3, no. 4, pp. 255–262, 2004.

[161] Shimizu, M., "Itinerant electron metamagnetism," *J. Phys. Fr.*, vol. 43, no. 1, pp. 155–163, 1982.

[162] C. Hurd, *The Hall Effect in Metals and Alloys*. New York -London: Plenum Press.

[163] H. Takahashi, R. Okazaki, Y. Yasui, and I. Terasaki, "Low-temperature magnetotransport of the narrow-gap semiconductor FeSb2," *Phys. Rev. B - Condens. Matter Mater. Phys.*, vol. 84, no. 20, p. 205215, 2011.

[164] S. Ishiwata, Y. Shiomi, J. S. Lee, M. S. Bahramy, T. Suzuki, M. Uchida, R. Arita, Y. Taguchi, and Y. Tokura, "Extremely high electron mobility in a phonon-glass semimetal," *Nat. Mater.*, vol. 12, no. 6, pp. 512–517, 2013.

[165] H. Takaki, K. Kobayashi, M. Shimono, N. Kobayashi, K. Hirose, N. Tsujii, and T. Mori, "Thermoelectric properties of a magnetic semiconductor CuFeS 2," *Mater. Today Phys.*, vol. 3, pp. 85–92, Dec. 2017.

[166] C. Kim, S. Kim, Y.-K. Hong, M.-W. Oh, and M.-H. Jung, "Correlation between the magnetic and thermoelectric properties in Mg2−xMnxSi," *J. Alloys Compd.*, vol. 690, pp. 51–56, Jan. 2017.

[167] A. U. Khan, R. A. R. Al Orabi, A. Pakdel, J.-B. Vaney, B. Fontaine, R. Gautier, J.-F. Halet, S. Mitani, and T. Mori, "Sb Doping of Metallic CuCr2S4 as a Route to Highly Improved Thermoelectric Properties," *Chem. Mater.*, vol. 29, no. 7, pp. 2988–2996, Apr. 2017.

[168] A. M. and E. G. and F. G. and Y. B. and V. Hardy, "Revisiting some chalcogenides for thermoelectricity," *Sci. Technol. Adv. Mater.*, vol. 13, no. 5, p. 53003, 2012.

[169] P. Prabukanthan and R. Dhanasekaran, “Growth of CuInTe2single crystals by iodine transport and their characterization,” *Mater. Res. Bull.*, vol. 43, no. 8–9, pp. 1996–2004, 2008.

[170] V. Kucek, C. Drasar, J. Kasparova, T. Plechacek, J. Navratil, M. Vlcek, and L. Benes, “High-temperature thermoelectric properties of Hg-doped CuInTe<inf>2</inf>,” *J. Appl. Phys.*, vol. 118, no. 12, p. 125105, Sep. 2015.

[171] N. Cheng, R. Liu, S. Bai, X. Shi, and L. Chen, “Enhanced thermoelectric performance in Cd doped CuInTe2 compounds,” *J. Appl. Phys.*, vol. 115, no. 16, p. 163705, Apr. 2014.

[172] G. Zhou and D. Wang, “High thermoelectric performance from optimization of hole-doped CuInTe2,” *Phys. Chem. Chem. Phys.*, vol. 18, no. 8, pp. 5925–5931, 2016.

[173] V. Kucek, C. Drasar, J. Navratil, T. Plechacek, and L. Benes, “Thermoelectric properties of Ni-doped CuInTe2,” *J. Phys. Chem. Solids*, vol. 83, pp. 18–23, 2015.

[174] F. Ahmed, N. Tsujii, and T. Mori, “Influence of Slight Substitution (Mn/In) on Thermoelectric and Magnetic Properties in Chalcopyrite-type CuInTe2,” *J. Electron. Mater.*, vol. (under rev, 2019.

[175] R. Liu, Y. Qin, N. Cheng, J. Zhang, X. Shi, Y. Grin, and L. Chen, “Thermoelectric performance of Cu 1−x−δ Ag x InTe 2 diamond-like materials with a pseudocubic crystal structure,” *Inorg. Chem. Front.*, vol. 3, pp. 1167–1177, 2016.

[176] Z. Xia, G. Wang, X. Zhou, and W. Wen, “Effect of the Cu vacancy on the thermoelectric performance of p-type Cu1−xInTe2 compounds,” *Ceram. Int.*, vol. 43, no. 18, pp. 16276–16282, Dec. 2017.

[177] N. Tsujii, H. Kitazawa, and G. Kido, “Electric and magnetic properties of Mn- and Fe-doped CuInS2 compounds,” *Phys. Status Solidi Appl. Res.*, vol. 189, no. 3, pp. 951–954, 2002.

[178] J. Callaway and H. C. von Baeyer, “Effect of Point Imperfections on Lattice Thermal Conductivity,” *Phys. Rev.*, vol. 120, no. 4, pp. 1149–1154, 1960.

[179] P. G. Klemens, “Thermal resistance due to point defects at high temperatures,” *Phys. Rev.*, vol. 119, no. 2, pp. 507–509, 1960.

[180] T. Plirdpring, K. Kurosaki, A. Kosuga, M. Ishimaru, A. Harnwunggmoung, T. Sugahara, Y. Ohishi, H. Muta, and S. Yamanaka, “Effect of the Amount of Vacancies on the Thermoelectric Properties of Cu–Ga–Te Ternary Compounds,” *Mater. Trans.*, vol. 53, no. 7, pp. 1212–1215, 2012.

[181] I. V Bodnar and N. S. Orlova, “Lattice Thermal Expansion in CuGaT2 and CuInTe2 Compounds over the Temperature Range 80 to 650 K from X-ray Diffracion Data,” *Cryst. Res. Technol.*, vol. 21, no. 8, pp. 1091–1096, 1986.

[182] K. Kishimoto, K. Kondo, and T. Koyanagi, “Preparation and thermoelectric properties of sintered Fe1−xCoxTe2 (0≤x≤0.4),” *J. Appl. Phys.*, vol. 100, no. 9, p. 93710, 2006.

[183] T. Harada, “Transport Properties of Iron Dichalcogenides FeX2(X=S, Se and Te),” *J. Phys. Soc. Japan*, vol. 67, no. 4, pp. 1352–1358, 1998.

[184] S. Raghavan, H. Wang, R. B. Dinwiddie, W. D. Porter, and M. J. Mayo, “The effect of grain size,

porosity and yttria content on the thermal conductivity of nanocrystalline zirconia," *Scr. Mater.*, vol. 39, no. 8, pp. 1119–1125, 1998.

Achievements

List of Publications

1. **Fahim Ahmed**, Naohito Tsujii and Takao Mori. Thermoelectric properties of $CuGa_{1-x}Mn_xTe_2$: power factor enhancement by incorporation of magnetic ion. J. Mater. Chem. A, Vol 5, issue 16, pp 7545-7554 (2017)

2. **Fahim Ahmed**, Naohito Tsujii and Takao Mori. Microstructure Analysis and Thermoelectric Properties of Iron doped $CuGaTe_2$. J. Materiomics, Vol 4, issue 3, pp 221-227, (2018)

3. **Fahim Ahmed**, Naohito Tsujii and Takao Mori. Influence of Slight Substitution (Mn/In) on Thermoelectric and Magnetic Properties in Chalcopyrite-type $CuInTe_2$, J. Electron. Mater. Submitted (2018)

List of Presentations

1. **F. Ahmed**, N. Tsujii and T. Mori, Secondary phase assisted enhanced TE properties and controlled microstructure in chalcopyrite-type CuGaTe2, *ICT2018* July 1 – 5, 2018 Caen, France- **Poster**

2. **F. Ahmed**, N. Tsujii and T. Mori, Magnetic Enhancement in a Thermoelectric Chalcopyrite-type Compound CuGaTe2: *IUMRS-ICAM2017* Aug 27 – Sep 1, 2017, Kyoto, Japan-**Oral**

3. **F. Ahmed**, N. Tsujii and T. Mori, Synthesis and Thermoelectric Properties of Mn doped $CuGaTe_2$: Effect of magnetic moment and charge carriers interactions *ICE2017* May 28 – 31, 2017, Nagoya, Japan- **Oral**

4. **F. Ahmed**, N. Tsujii and T. Mori, Enhanced thermoelectric properties in the chalcopyrite-type magnetic semiconductor $CuIn_{1-x}Mn_xTe_2$, *TSJ2017* Sep 11 – 13, 2017 Osaka Japan-**Poster**

5. **F. Ahmed**, N. Tsujii and T. Mori, Microstructure Analysis and Thermoelectric Properties in Fe Doped Chalcopyrite-type $CuGaTe_2$, *Japanese Flux Growth Society Meeting,* DEC 7-8, 2017 Yokohama, Japan-**Poster**

6. **F. Ahmed**, N. Tsujii and T. Mori, Enhanced thermoelectric properties in Mn- and Fe-doped CuGaTe2: *RIKEN-NIMS 1st Materials Innovation Core Workshop* Jan 24, 2018, Tokyo Japan-**Poster**

Acknowledgements

I would like to take this opportunity to acknowledge all the help and support I got during my PhD. My sincere gratitude to my supervisor Prof. Takao Mori for his guidance. I thank him for always being available for discussion whenever needed. It would not have been possible without his constant support and encouragement throughout my research. I especially thank him for his suggestions and kind help in improving my writing and presentation skills.

I would like to express my deepest gratitude to Dr. Naohito Tsujii who plays a key role in my PhD research. I thank him for all his invaluable support and guidance. I have greatly benefited from his scientific knowledge and expertise. I especially thank him for being patient to all my imperfections.

Special thanks goes to my PhD Committee members Prof. Naoki Fukata, Prof. Seiji Mitani and Prof. Yoshikazu Suzuki for their insightful comments and suggestions.

I thank Dr. Yoshitaka Matsushita for high temperature XRD and analysis.

I also like to thank Mrs. Erika Arisumi, Mrs. Sayaka Latumeten and Mrs. Namiko Onodera for taking care of official work and documentation. I am extremely grateful to you all for always being there for kind help. Their assistance made my stay in Japan easier and enjoyable.

I want to thank all my group members for the discussion and valuable feedback especially GUO Quansheng and Jean Baptiste Vaney for teaching me various apparatuses.

I would like to acknowledge National Institute of Material Science (NIMS) and University of Tsukuba for providing me this wonderful opportunity and financial support during my stay in Japan.

Lastly, I want to thank all my family members and friends for their unconditional love and support throughout my life.